

Spin dynamics and transport in magnetic heterostructures

von der Fakultät für Naturwissenschaften der Technischen Universität Chemnitz
genehmigte Dissertation zur Erlangung des akademischen Grades

doctor rerum naturalium

(Dr. rer. nat.)

vorgelegt von M. Sc. Tobias Schneider

geboren am 16.02.1991 in Gera

eingereicht am 30.11.2018

Gutachter:

Prof. Dr. rer. nat. Sibylle Gemming

Prof. Dr. rer. nat. Jürgen Fassbender

Tag der Verteidigung: 15.03.2019

*Meinen Eltern &
Ulrike*

"One, remember to look up at the stars and not down at your feet. Two, never give up work. Work gives you meaning and purpose and life is empty without it. Three, if you are lucky enough to find love, remember it is there and don't throw it away."

— **Stephen Hawking**

Tobias Schneider

Spin dynamics and transport in magnetic heterostructures

Dissertation (in englischer Sprache), Technische Universität Chemnitz, Fakultät für Naturwissenschaften, Chemnitz (2018), 124 Seiten, 43 Abbildungen, 4 Tabellen

Stichworte: Spin Suprafluidität, Spintransport, Ferromagnetische Resonanz, Spinwellen, Nichtreziprozität

Kurzfassung

Die direkte Integration von magnon-spintronischen Bauteilen in moderne Technologien erfordert die Entwicklung von kurzwelligen Spinwellenquellen und verlustarmer Spinwellenleiter.

In dieser Arbeit werden mögliche Lösungen für diese beiden Herausforderungen vorgestellt. Der erste Teil dieser Arbeit beschäftigt sich mit der nichtreziproken Spinwellenemission in magnetischen Doppellagen. Zwei Prototypsysteme werden theoretisch untersucht und durch experimentelle Ergebnisse untermauert: (i) ausgedehnte magnetische Doppellagen und (ii) mikrometer-große elliptische Doppellagen. Durch die dynamischen Dipol-Dipol-Wechselwirkungen wird eine Nichtreziprozität der Dispersionsrelation induziert. Diese wird mittels mikromagnetischer Simulationen und einer analytischen Theorie untersucht. Die nichtreziproke Frequenzverschiebung nimmt hierbei bei kleinen Wellenzahlen linear mit der Filmdicke zu. Die topologische Emission von Spinwellen wird in den mikrometer-großen elliptischen Doppellagen unter Verwendung von Röntgentransmissionsmikroskopie beobachtet und theoretisch unter Verwendung mikromagnetischer Simulationen bestätigt.

Im zweiten Teil dieser Arbeit wird der spezielle Spintransport in ferromagnetischen dünnen Filmen untersucht, der als Spinsuprafluidität bekannt ist. Das Hauptmerkmal dieses makroskopischen Zustands ist die Abhängigkeit des dissipierten Spinstromes von der Propagationslänge als Potenzgesetz im Gegensatz zur exponentiellen Dämpfung von Spinwellen. Die Existenz und die Stabilität des suprafluiden Transportes in dünnen ferromagnetischen Filmen, angeregt durch einen spinpolarisierten Strom, in Gegenwart der intrinsischen Dipol-Dipol-Wechselwirkungen wird erstmals beschrieben. Um Hinweise für die experimentelle Realisierung der Spinsuprafluidität zu geben, wird die Abhängigkeit des Zustandes vom Anregungsstrom numerisch analysiert. Hierbei ergeben sich drei verschiedene Bereiche für den Fall vernachlässigter als auch aktivierter Dipol-Dipol-Wechselwirkung. Dies zeigt die Allgemeinheit des untersuchten Systems. Die beiden vorgestellten Effekte könnten in Zukunft neue Wege für die technologische Anwendung magnonischer Strukturen eröffnen.

Tobias Schneider

Spin dynamics and transport in magnetic heterostructures

Dissertation, Technische Universität Chemnitz, Fakultät für Naturwissenschaften, Chemnitz (2018), 124 pages, 43 figures, 4 tables

Keywords: spin superfluidity, spin transport, ferromagnetic resonance, spin waves, nonreciprocity

Abstract

The direct integration of magnon-spintronic devices in current technologies requires the development of spin-wave sources emitting ultra-short wavelengths and low-loss spin-wave guides. In this work, possible solutions for both of these challenges are provided.

The first part of this thesis is dedicated to the nonreciprocal spin-wave emission in magnetic bilayers. Two prototype systems are theoretically investigated and corroborated by experimental results: (i) extended magnetic bilayer films and (ii) micron-sized elliptical magnetic bilayers. The nonreciprocity of the dispersion relation induced by the dynamic dipole-dipole interactions is investigated by means of micromagnetic simulations and an analytic theory. The nonreciprocal frequency shift linearly increases with the film thickness for small wave numbers. The topological emission of short-wavelength spin waves is observed in the micron-sized elliptical magnetic bilayers using scanning transmission X-ray microscopy and theoretically corroborated utilizing micromagnetic simulations.

The second part of this thesis theoretically investigates a special spin transport mechanism in ferromagnetic thin films termed spin superfluidity. The main characteristic of this macroscopic state is the power-law dependence of the dissipated spin current in contrast to the exponential damping of spin waves, enabling low-loss long-range transport. The possible existence and the stability of the superfluidic transport in ferromagnetic thin films excited by spin-transfer torque in the presence of the intrinsic dipole-dipole interactions is reported for the first time. To provide indicators to prove the experimental realization of a spin superfluid the dependence on the excitation current is numerically analyzed. Three distinct regimes are obtained for both disabled and enabled dipole-dipole interactions, showing the generality of the investigated system.

Both presented effects might open new paths for the technological application of magnonic devices in the future.

Contents

Kurzfassung	vii
Abstract	ix
1. Introduction	1
2. Fundamentals	5
2.1. Contributions to the Total Energy	5
2.2. Magnetization Dynamics	13
2.2.1. Equation of Motion for Macro-Spins	13
2.2.2. Spin Waves	18
2.3. Hydrodynamic Formulation of Magnetization Dynamics	22
3. Experimental and Numerical Methods	27
3.1. Ferromagnetic Resonance	27
3.1.1. Broadband CPW-FMR	27
3.2. Numerical Micromagnetism - MuMax ³	28
3.2.1. Evaluation of Micromagnetic Simulations	30
4. Nonreciprocal Spin Wave Emission in Magnetic Bilayers	39
4.1. Theoretical Description	40
4.2. Nonreciprocity in Extended Thin Films	42
4.3. Nonreciprocal Spin-Wave Emission in Stacked Vortex Pairs	55
5. Numerical Investigation of Spin Superfluid Transport in Quasi-U(1) Systems	63
5.1. Thin Films with Dipole-Dipole Interaction	63
5.2. Nanowires with Out-of-Plane Anisotropy	78
6. Conclusion and Outlook	89
A. Appendix	92
A.1. Coefficient for FMR in Coupled Bilayers	92
A.2. Matrix Elements	93

Contents

A.3. The Effect of Windowing	95
Bibliography	96
List of Figures	109
List of Tables	112
Declaration of Authorship	114

1. Introduction

Research regarding magnetic materials and their applications has attracted enormous interest in the last decades [1]. This class of materials is already present in our everyday life, e. g. in electric motors, sensors or in information technology [2, 3]. Many of these applications are based on the combination of the electric charge transport and the electron spin, providing an additional degree of freedom [4, 5].

This new research field, termed spintronics was particularly stimulated by the discovery of the giant magnetoresistance (GMR) [6, 7], tunneling magnetoresistance (TMR) [8] and the spin transfer torque effects (STT) [9]. The mentioned examples show the direct interaction of a charge current with the magnetic moment. It is interesting to note that commercial products based on the GMR, TMR and STT already exist. The GMR effect was implemented as the new technology in hard disk drives to read out the information shortly after its discovery. Recently, the first commercial magnetic random access memory (MRAM) combining the TMR and the STT for reading and writing operation was launched. Utilizing magnetic material in such ways directly shows the advantages of spintronic systems. The information stored with magnetic material is non-volatile in comparison with conventional dynamic random access memory (DRAM). The operation speed of MRAM devices can reach GHz or even THz and therefore, can compete with the common DRAM. The operation speed of magnetic devices for example can be tuned by the size and geometry of the device, novel material and ion beams, providing the ability to optimize the device for the desired application [10, 11].

Besides the emerging field of spintronics, the direct application of spin waves or magnons—the elementary excitations in magnetic materials—is heavily investigated [12–14]. Since all spintronic applications still involve the electric charge transport, Joule heating will always be present, limiting the energy efficiency of spintronic devices. The field of magnon spintronic or magnonics tries to explore the direct integration of spin waves in logic circuits for information transport and processing. Such wave-based logic circuits could utilize not only the amplitude of the incoming signal, but also the phase or frequency, opening new possibilities for non-boolean architectures. To fabricate commercial devices, three important issues have to be solved: (i) The efficient excitation of spin waves with arbitrary wavelength and frequency, (ii) the fabrication of spin waveguides and (iii) the detection of the spin wave signal. Besides these three important parts, the general property of nonrecip-

rocal transport has to be fulfilled [13, 15]. So far, all issues have been partially addressed in the literature. The generation of spin waves with very short wavelength by using a vortex core as an emitter was shown by using STXM [16]. However, this scheme produces radial spin waves with very small propagation distances. More commonly lithographically prepared antennas are utilized to excite spin waves. However, to pattern structures well below 100 nm is challenging. A natural solution for this issue is the usage of magnetic textures as spin wave emitters [17, 18].

Many works focused on the investigation of magnonic waveguides. Besides the concept of the geometrical confined waveguides [19–22], flexible schemes based on effective field wells at the edge of the structure or generated by magnetic textures have been proposed [23–25].

Regarding the detection of the transmitted spin wave signal, the spin-pumping effect [26] and the inverse spin Hall effect [27] provide efficient processes. Moreover, the spin wave signal is converted in an electric signal [28], making it compatible with current technologies.

The general property of the nonreciprocal transport can be achieved in multiple ways. Every Damon-Eshbach spin wave shows a nonreciprocal transport regarding the spin-wave amplitude for a magnetic film thickness larger than the exchange length [29, 30]. To integrate magnonic devices into current information technology devices the film thickness is limited, and therefore, new approaches are needed. Recently many ways to manipulate the spin-wave dispersion relation have been proposed: Prominent examples are the modification of the material parameters at the surfaces of the magnetic film [31] or the usage of the Dzyaloshinskii-Moriya interaction (DMI) [32, 33]. Both schemes require elaborated techniques regarding the growth of the magnetic thin films, and therefore, provide many challenges.

As already discussed by Grünberg *et al.* in the 1980s [7, 34, 35], nonreciprocal properties can be introduced by the intrinsic dipolar interactions in magnetic materials. Recent reports point out that arrays of magnetic nanopillars, ferromagnetic nanotubes, and anti-ferromagnetic coupled bilayers exhibit nonreciprocal transport. Detailed theoretical and experimental studies regarding the magnon transport in magnetic bilayers are still missing.

The complete discussion of magnonic devices was so far focused only on spin waves. As shown by many authors, the propagation distance of spin waves can be rather limited depending on the material system. Studies for the spin-wave transport in magnetic insulators show the possibility of centimeter-long propagation distance in specific systems. However, commonly the propagation distance is limited to micrometers. However, already in the year 1969 a hydrodynamic formulation of spin waves was proposed [36]. This theoretical framework opened the discussion of similarities of the equations of motion in ferromagnetic system to the hydrodynamic equation for ideal fluids. Years later the field was rediscov-

ered [37] and was termed spin superfluidity, given by the similarities of the spin transport with superfluids. Several authors show the big advantage of the spin superfluidity compared to spin waves [37–42]. The superfluidic spin transport shows a power-law spatial decay in contrast to the exponential decay of spin waves, and thus enables long-range spin transport. So far mainly analytic studies omitting dipole-dipole interactions have been published. Only two micromagnetic studies of the spin superfluidity are available [43, 44]. However, both studies investigated micron-sized system with very strong magnetostatic fields. These strong magnetostatic fields lead to the suppression of the spin superfluid. This issues can be avoided considering extended thin films.

On this basis, the first part of this thesis deals with the nonreciprocal spin-wave transport in magnetic bilayers and the generation of planar spin waves with short wavelength in such systems. The dynamic dipole interactions inside the bilayer are carefully analyzed and a simple analytical formula to calculate the dispersion relation in antiferromagnetically aligned bilayers is provided. Both, experimental results obtained utilizing ferromagnetic resonance, magnetometry, transmission electron microscopy and Brillouin light scattering, as well as micromagnetic simulations support the analytic model.

The second part addresses the spin superfluidity and the impact of dipole-dipole interactions on this state. A combined analytical and numerical approach predicts the stability of the superfluid for (i) omitted dipole-dipole interactions and (ii) including dipole-dipole interactions. For both cases qualitatively the same behavior was obtained. In contrast to the published work so far, the superfluidic transport is not subject to a simple breakdown due to large excitation strength. The obtained numerical results indicate the existence of three different transport regimes. For small excitation bias the traditional superfluid is obtained. For larger bias a breakdown was expected. However, the superfluid is subject to a self-stabilization mechanism in this regime, allowing the emission of spin waves. Such a superposition shares many similarities with the well-known two-fluid model for superfluid He, indicating the generalities of superfluidic systems. This and also the third regime are strongly influenced by the interaction of the active region or the injector and the transport channel. For even larger excitations of the superfluid, the injector is polarized and the transmitted spin current, and therefore, the superfluid is screened. Besides the novel regimes, it is shown that the general behavior is not affect by additional anisotropies or dipole-dipole interactions, indicating possible paths for the experimental realization of such spin superfluids in ferromagnetic thin films.

This thesis is divided into six chapters: Chapter 2 covers the important theoretical background needed to understand the theoretical and experimental results. The contribution to the total energy in ferromagnets, the magnetization dynamics of single spins and spin waves, and theoretical details regarding the spin superfluidity are presented.

The next chapter, 3, summarizes the experimental and numerical methods used in this thesis. The basics regarding the ferromagnetic resonance and the vector network analyzer ferromagnetic resonance setup are shortly described. In order to understand the evaluation of the numerical results, micromagnetic simulations are briefly introduced. Both high-performance programs developed in the course of the present work, commonly utilized for the evaluation of micromagnetic simulations are described in detail and benchmarked.

The fourth chapter is devoted to the nonreciprocal spin-wave emission in magnetic bilayers. The theoretical framework deriving the dispersion relation in magnetic bilayers developed in close collaboration with the group of Prof. Landeros at the Universidad Técnica Federico Santa María in Valparaíso is briefly described and compared to micromagnetic simulations performed within the present thesis. To obtain experimental evidence ferromagnetic resonance spectroscopy performed by me as well as, magnetometry, and Brillouin light scattering were employed, showing a remarkable agreement with the theoretical description.

The fifth chapter summarizes the results regarding the spin superfluidity in ferromagnetic thin films. Two different systems exhibiting spin superfluidity are presented. For ferromagnetic thin films three regimes are obtained using micromagnetic simulations. The numerical results are compared with an analytic theory developed by D. Hill at the University of California, Los Angeles. Hypotheses are presented in order to understand the interaction of the injector with the transport channel, resulting in the emergence of the three distinct regimes. Moreover, similarities with the two-fluid model of superfluid He are discussed.

In the final chapter the main results obtained in this thesis are recapitulated and an outlook for further studies is provided.

2. Fundamentals

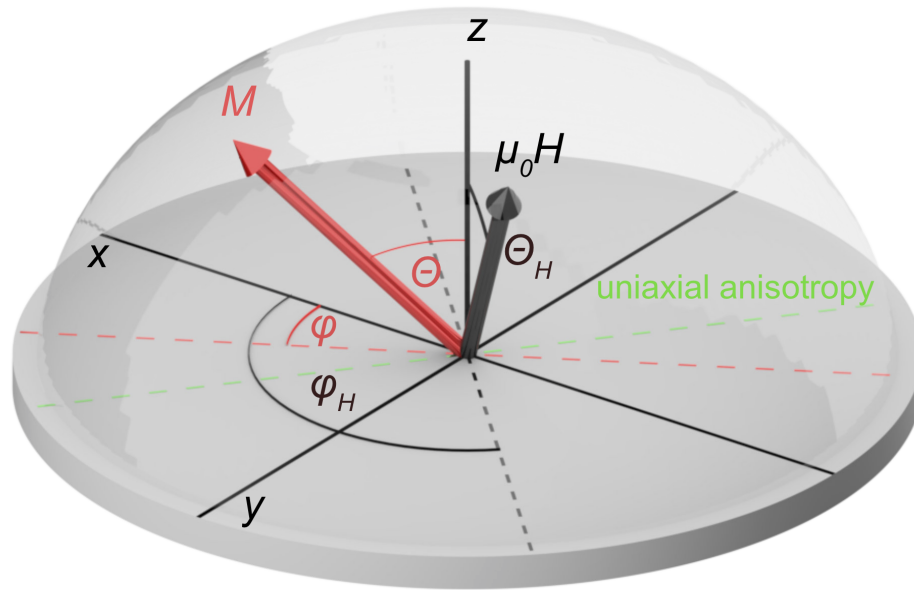


Figure 2.1.: Spherical coordinate system for the magnetization \vec{M} and the external field $\mu_0 \vec{H}$.

This chapter will cover specific fundamentals, which are important for understanding subsequent experimental and numerical results. The first section is devoted to the contribution of the free energy for a ferromagnetic body. Afterwards the dynamics for both a macro-spin and non-uniform excitations, spin waves, will be presented. In the final section, a unique transport phenomenon in thin ferromagnetic films will be introduced. If not otherwise indicated, the coordinate system used throughout this thesis is depicted in Fig. 2.1.

2.1. Contributions to the Total Energy

For the understanding of the magnetic configuration and excitations of magnetic bodies, it is important to find an expression for the total energy E_{tot} . This quantity contains all information necessary to derive all relevant physical quantities observed in experiments.

The five most important contributions are:

$$E_{\text{tot}} = E_{\text{exch}} + E_{\text{MCA}} + E_{\text{Zeeman}} + E_{\text{dipole}} + E_{\text{IEC}} + \dots \quad (2.1)$$

with E_{exch} , the exchange energy, E_{MCA} , the magnetocrystalline anisotropy energy, E_{Zeeman} , the Zeeman energy, E_{dipole} , the magnetostatic energy and E_{IEC} , the interlayer exchange energy. All these five contributions will be discussed in detail in the following section. To derive the contribution to the total energy, the magnetization is considered as a vector field $\vec{M}(\vec{r}, t)$, according to the interpretation of W. F. Brown [45]:

$$\vec{M}(\vec{r}, t) = M_s \cdot \vec{m}(\vec{r}, t). \quad (2.2)$$

To simplify calculations, the reduced magnetization $\vec{m}(\vec{r}, t)$ is introduced. Multiplying with the saturation magnetization M_s , the full magnetization can be recovered. The magnetization configuration is assumed to continuously vary in space and time within the magnetic body. In contrast to the domain theory developed by Landau and Lifshitz, no constraints keeping the magnetization uniform within a domain are included. Therefore, many localized phenomena can be described by micromagnetic approaches. For some experimental observations it is sufficient to consider a single macro-spin as

$$\vec{M} = \frac{1}{V} \int \vec{M}(\vec{r}, t) dV \quad (2.3)$$

with the volume of the magnetic body V . This macro-spin can be considered as the averaged response of all magnetic moments.

In the following, the important energy contribution will be briefly derived.

Exchange Energy

The exchange energy is a direct consequence of the Pauli exclusion principle [46]. In quantum-mechanical calculations of many particles the symmetrization or antisymmetrization of the wave function indirectly introduces new effective terms in the many-particle Hamiltonian. Therefore, the commonly used Heisenberg Hamiltonian to describe the exchange interaction in ferromagnets and antiferromagnets should be considered an effective Hamiltonian, which is given by

$$\hat{H} = -\frac{J}{2} \sum_{\langle i, j \rangle} \hat{S}_i \cdot \hat{S}_j \quad (2.4)$$

with the exchange integral J and the spin operators \hat{S} at the lattice sites i and j . The summation is executed for all lattice sites in the lattice. To prevent the double counting of

spins, the factor $1/2$ is included. The here presented operator is commonly used to solve the exchange energies on the atomistic scale. However, generally the observation length in experiments is much larger than the atomic distances and it is appropriate to consider an average within a continuum theory. Therefore, the angle $\phi_{i,j}$ between the spins at the lattice sites i and j is introduced. The newly obtained equation reads

$$\hat{H} = -\frac{J}{2} \sum_{\langle i,j \rangle} \hat{S}_i \hat{S}_j (1 - \phi_{i,j}^2). \quad (2.5)$$

By assuming only small angle variations between neighboring spins and rewriting this finite difference into a derivative, the exchange energy can be written as

$$E_{\text{exch}} = A \int [|\nabla m_x|^2 + |\nabla m_y|^2 + |\nabla m_z|^2] dV. \quad (2.6)$$

Here, A is the exchange constant, an important material parameter and m_i the component of the reduced magnetization $\vec{m}(\vec{r}, t)$. Since the exchange energy depends on the gradient of the individual magnetization components, it is intuitively clear that this contribution is zero in the macro-spin approach.

Dzyaloshinskii-Moriya interaction

For specific system without inversion symmetry, an additional contribution to the exchange has to be considered. The spin-orbit interaction leads to the introduction of the antisymmetric exchange interaction or Dzyaloshinskii-Moriya interaction (DMI) given by the Hamiltonian:

$$H_{\text{DMI}} = \sum_{\langle i,j \rangle} [\vec{S}_i \times \vec{S}_j] \cdot \vec{d}_{ij}. \quad (2.7)$$

Here, \vec{S}_i and \vec{S}_j are two neighbouring spins at the lattice sites i and j . \vec{d}_{ij} is the corresponding Dzyaloshinskii-Moriya vector. Depending on the symmetry class of the investigated system the Dzyaloshinskii-Moriya vector has to be chosen accordingly [47].

An easy example is given by the symmetry break provided by an interface of a ferromagnetic layer with a heavy metal. This effect is usually termed interfacial DMI [48]. For this case the Dzyaloshinskii-Moriya vector is given by [48]:

$$\vec{d}_{ij} = d_{ij} (\hat{z} \times \hat{u}_{ij}), \quad (2.8)$$

where \hat{z} and \hat{u}_{ij} are the unit vectors perpendicular to the surface and the connection of the lattice sites i and j , respectively. d_{ij} is reduced to a scalar constant.

2. Fundamentals

The interfacial DMI favors two different alignments depending on the sign of d_{ij} . If $d_{ij} > 0$ ($d_{ij} < 0$) the magnetization rotates anticlockwise (clockwise). Assuming that the normal exchange is nonzero leads to the formation of spin spirals in the presence of DMI.

The micromagnetic energy given by the interfacial DMI can be formulated as follows [48]:

$$E_{\text{DMI}} = D \cdot (m_z \partial_x m_x - m_x \partial_x m_z + m_z \partial_y m_y - m_y \partial_y m_z) \quad (2.9)$$

with the DMI constant D .

Zeeman Energy

Already within the classical electro-dynamic theory, the energy of a magnetic dipole in a magnetic field \vec{H} , termed Zeeman energy, is defined based on the torque exerted on the magnetic dipole. The Zeeman energy of a single magnetic dipole is given by

$$E_{\text{Zeeman}} = -\mu_0 \vec{\mu} \cdot \vec{H}. \quad (2.10)$$

Depending on the relative orientation of the magnetic dipole moment $\vec{\mu}$ and the magnetic field \vec{H} , the Zeeman energy can be positive for antiparallel alignment or negative for parallel alignment. However, without external perturbation both configurations can be considered stable.

Since the magnetic moment is mainly carried by the electronic spin in ferromagnets, the magnetic dipole moment can be replaced by $\mu_e = g \frac{\mu_B}{\hbar} \vec{S} = \gamma \vec{S}$, resulting in

$$E_{\text{Zeeman}} = -\mu_0 \gamma \vec{S} \cdot \vec{H}. \quad (2.11)$$

with the gyromagnetic ratio $\gamma = g \frac{\mu_B}{\hbar}$ and the g-factor g . Furthermore, this equation can be expressed in terms of the magnetization, instead of the spin operator

$$E_{\text{Zeeman}} = -\mu_0 M_s \int \vec{m}(\vec{r}) \cdot \vec{H}(\vec{r}) dV. \quad (2.12)$$

However, since the magnetization is a vector field, we have to integrate over the volume of the magnetic body.

Then, the relation for a macro-spin can easily be written as

$$E_{\text{Zeeman}} = -\mu_0 V M_s \vec{m} \cdot \vec{H} \quad (2.13)$$

Rewriting the vector product using the polar coordinates defined in Fig.2.1 and dividing by the volume V , gives the well-know expression for the

Zeeman energy density $\varepsilon_{\text{Zeeman}} = E_{\text{Zeeman}}/V$

$$\varepsilon_{\text{Zeeman}} = -\mu_0 M_s H [\sin \theta \sin \theta_H \cos(\varphi - \varphi_H) - \cos \theta \cos \theta_H]. \quad (2.14)$$

Magnetostatic Energy

The contribution of the dipole-dipole interactions between the magnetic dipole moments is of great importance for the magnetization dynamics, as well as the spatial magnetization configuration. As one will see in the Chapters 4 and 5, the dipole-dipole interactions can strongly influence many effects and therefore are a source of phenomena that have not been described before. In the simplest model, only the dipole-dipole interaction between two magnetic moments $\vec{\mu}_i$ and $\vec{\mu}_j$ separated by \vec{r}_{ij} is considered. To consider all magnetic moments, a summation over all lattice sites i and j has to be performed, leading to:

$$E_{\text{dipole}} = \frac{1}{2} \sum_{i,j} \frac{\mu_0}{4\pi} \left[\frac{\vec{\mu}_i \cdot \vec{\mu}_j}{r_{ij}^3} - \frac{3(\vec{r}_{ij} \cdot \vec{\mu}_i)(\vec{r}_{ij} \cdot \vec{\mu}_j)}{r_{ij}^5} \right]. \quad (2.15)$$

As for the exchange energy, the factor $\frac{1}{2}$ prevents the double counting of magnetic moments twice. For continuous magnetization distributions one may assume that the separation r_{ij} is small, the sum can be rewritten into an integral over the volume of the magnetic body. With this we finally find the magnetostatic energy for a magnetic body with arbitrary shape, E_{dipole} :

$$E_{\text{dipole}} = -\frac{\mu_0 M_s}{2V} \int \vec{m}(\vec{r}) \cdot \vec{H}_{\text{dip}}(\vec{r}) dV. \quad (2.16)$$

Therefore, the problem was simplified and condensed to the calculation of the magnetostatic field $\vec{H}_{\text{dip}}(\vec{r})$. To find a general expression for the magnetostatic field, Maxwell's equations [49] have to be considered. Within the classical electrodynamics the divergence of the magnetic field $\vec{B}(\vec{r})$ is zero and, therefore, the existence of magnetic monopoles is forbidden

$$\vec{\nabla} \cdot \vec{B}(\vec{r}) = 0. \quad (2.17)$$

However, this equation is not sufficient in the given context, since a magnetic body is considered. The magnetic field $\vec{B}(\vec{r})$ has to be replaced by the auxiliary field equation

$$\vec{B}(\vec{r}) = \mu_0 \left[\vec{H}_{\text{dip}}(\vec{r}) + M_s \vec{m}(\vec{r}) \right]. \quad (2.18)$$

Combining both equations leads to:

$$\vec{\nabla} \cdot \vec{H}_{\text{dip}}(\vec{r}) = -\frac{M_s}{\mu_0} \vec{\nabla} \cdot \vec{m}(\vec{r}). \quad (2.19)$$

As directly visible from Eq. (2.19), the magnetostatic field is directly related to the divergence of the magnetization. Therefore, the existence of magnetic (pseudo-) charges can be postulated, since the equation shows similarities with another Maxwell equation for the electrical field. However, magnetic pseudo-charges are only similar to classical electric charges. They also show attractive and repulsive forces, but cannot annihilate. For the understanding of the symmetry of the magnetostatic field and the relative orientation, it is sometimes useful to rely on the principle of magnetic charges. An example will be presented in Chapter 4.

To simplify the problem further, we also assume the electrostatic case. Since no current densities are present in the magnetic body, the second Maxwell equation states $\vec{\nabla} \times \vec{H}_{\text{dip}}(\vec{r})$. Such vector fields are termed irrotational vector fields. For this kind of vector fields an identity of vector calculus states $\vec{\nabla} \times (\nabla\Phi)$. Therefore, a scalar potential Φ can be found, satisfying the condition of zero curl. The magnetostatic field now can be written as:

$$\vec{H}_{\text{dip}} = -\nabla\Phi. \quad (2.20)$$

Combing Eqs. (2.19) and (2.20), results in the defining equation for the magnetostatic potential Φ

$$\Delta\Phi(\vec{r}) = M_s \vec{\nabla} \cdot \vec{m}(\vec{r}). \quad (2.21)$$

This resembles the well-known Poisson equation, for example found in the calculation of the electric potential. Since the solution for the Poisson equation was already calculated for the electric potential, the solution can be written as

$$\Phi = M_s \int G(\vec{r}, \vec{r}') \left(\vec{\nabla}_{\vec{r}'} \cdot \vec{m}(\vec{r}') \right) dV'. \quad (2.22)$$

The solution of this linear differential equation is given by Green's function $G(\vec{r}, \vec{r}') = -\frac{1}{4\pi} \frac{1}{|\vec{r} - \vec{r}'|}$ [50]. The area of integration is still not specified. If we assume a magnetic body with the volume V , the magnetostatic potential can be calculated by $\Delta\Phi_{\text{out}}(\vec{r}) = 0$, since the magnetization is zero outside of the magnetic body. This does not necessarily mean that the magnetostatic potential is zero outside the magnetic body. Since the starting point were Maxwell's equations, the potential has to fulfill the boundary conditions at the interface of the magnetic body. This leads to a continuous potential itself, but to a discontinuous derivative [51]. The boundary conditions can be formulated as:

$$\Phi_{\text{in}}(\vec{r}) = \Phi_{\text{out}}(\vec{r}), \quad (2.23)$$

$$\frac{\delta\Phi_{\text{in}}(\vec{r})}{\vec{n}} - \frac{\delta\Phi_{\text{out}}(\vec{r})}{\vec{n}} = \vec{M}(\vec{r}) \cdot \vec{n}. \quad (2.24)$$

with the normal vector \vec{n} given by the surface of the magnetic body. By constraining the integration volume in Eq. (2.22) and using Gauss's theorem, the integral can be split into two contributions. The resulting magnetostatic field is then given by [51, 52]

$$\vec{H}_{\text{dip}}(\vec{r}) = \nabla \left(\int_V dV' \frac{\vec{\nabla} \cdot \vec{M}(\vec{r}')}{|\vec{r} - \vec{r}'|} + \int_{\partial V} dA' \frac{\vec{n} \cdot \vec{M}(\vec{r}')}{|\vec{r} - \vec{r}'|} \right). \quad (2.25)$$

This representation has the great advantage that both contributions arising from the volume and surface can be calculated individually. We will come back to this in the presentation of the magnetostatic field in case of a magnetic bilayer in Chapter 4.

However, the exact analytical calculation of the magnetostatic potential or magnetostatic field is very challenging. Only for a few shapes of a magnetic body the Eq. (2.25) can be solved analytically. Depending on the case of application either the magnetostatic field can be calculated numerically or appropriate analytic approximations can be done [51, 53]. For the calculation of the dynamics of a single spin, the simplification using the demagnetization tensor N proved reliable:

$$\vec{H}_{\text{dip}}(\vec{r}) = -M_s \underline{N} \cdot \vec{m}(\vec{r}). \quad (2.26)$$

This tensor either can be calculated analytically for the case of a uniformly magnetized ellipsoid or again approximated numerically.

Magneto-crystalline Anisotropy

So far, no energy contribution was introduced to favor any alignment of the magnetization in an infinite magnetic body. However, many realistic systems show an energetically more complex landscape. This phenomenon is referred to as magneto-crystalline anisotropy (MCA). The origin of the difference in energy while rotating the magnetization with respect to the crystal lattice is given by the spin-orbit interaction and dipole-dipole interactions [54–56]. Thereby, the energy of the magneto-crystalline anisotropy can be expressed in terms of the crystal symmetry itself:

$$E_{\text{mca}} = \int g(\vec{m}(\vec{r})) dV. \quad (2.27)$$

Here, the function $g(\vec{m}(\vec{r}))$ contains all the information of the underlying symmetry.

The two important anisotropy contributions are the uniaxial anisotropy (90° symmetry) and the cubic anisotropy (45° symmetry). Since both contribution will be used throughout this thesis, the underlying equations will be discussed briefly within the macro-spin approximation.

In many systems the uniaxial anisotropy strongly differs between the direction within the film plane and perpendicular to the film plane. Therefore, two independent anisotropies are induced. The in-plane and out-of-plane cases are governed by the anisotropies arising from the anisotropy constants $K_{2,\parallel}$ and $K_{2,\perp}$, respectively. The uniaxial anisotropy energy density ε_u is given by

$$\varepsilon_u = -K_{2,\perp} \sin^2 \theta - K_{2,\parallel} \sin^2 \theta \cos^2 (\varphi - \varphi_u). \quad (2.28)$$

All angles θ , φ and φ_u are defined according to Fig. 2.1.

The energy density contribution arising from a cubic crystal lattice ε_c reads

$$\varepsilon_c = K_4 \sin^2 \theta - \frac{1}{8} K_4 (\cos(4\varphi) + 7) \sin^4 \theta \quad (2.29)$$

with the cubic anisotropy constant K_4 .

Interlayer exchange energy

This contribution to the total energy is similar to the exchange energy, but the coupling of neighboring spins is not within the films itself, but rather across an interface. In general, the interlayer exchange coupling can be considered as a special case of the so-called Ruderman-Kittel-Kasuya-Yoshida (RKKY) interaction [57]. The energy of the interlayer exchange for each two coupled magnetic layer can be written as

$$E_{\text{IEC}}^{(1)} = -\frac{J_1}{M_s^{(1)}d^{(1)}} \int \vec{m}^{(1)}(\vec{r}) \cdot \vec{m}^{(2)}(\vec{r}) dV_1 - \frac{J_2}{M_s^{(1)}d^{(1)}} \int [\vec{m}^{(1)}(\vec{r}) \cdot \vec{m}^{(2)}(\vec{r})]^2 dV_1, \quad (2.30)$$

$$E_{\text{IEC}}^{(2)} = -\frac{J_1}{M_s^{(2)}d^{(2)}} \int \vec{m}^{(1)}(\vec{r}) \cdot \vec{m}^{(2)}(\vec{r}) dV_2 - \frac{J_2}{M_s^{(1)}d^{(1)}} \int [\vec{m}^{(1)}(\vec{r}) \cdot \vec{m}^{(2)}(\vec{r})]^2 dV_2. \quad (2.31)$$

Here the saturation magnetization $M_s^{(i)}$, the layer thickness $d^{(i)}$ and the reduced magnetization $\vec{m}^{(i)}(\vec{r})$ corresponds to the magnetic layer i . Clearly, the similarities between the exchange energy and the interlayer exchange energy are visible.

Depending on the sign of the bilinear coupling constant J_1 the alignment of the two ferromagnetic layers can either be parallel for $J_1 > 0$ or antiparallel for $J_1 < 0$. Moreover, the coupling constant J_1 also strongly depends on the spacer material and the spacer thickness. If the bilinear coupling vanishes, the biquadratic coupling constant favors a 90° alignment of the magnetization for $J_2 < 0$. By tuning both material and thickness, the desired ground state configuration can be achieved. Extended reviews regarding the interlayer exchange coupling were published by Stiles [58] and Bruno [59,60].

Magnetic Ground State

All energy contributions derived above will affect the ground state of the investigated magnetic system. To obtain the magnetization configuration, which minimizes the total energy, the first variation of the latter has to be calculated. This results in Brown's equations [45]

$$\mu_0 M_s \vec{m} \times \vec{H}_{\text{eff}} = 0, \quad (2.32)$$

$$\left. \frac{\partial \vec{m}}{\partial \vec{n}} \right|_S = 0 \quad (2.33)$$

with the normal vector \vec{n} according to the surface S of the magnetic body. The effective field H_{eff} for a single magnetic body is defined by:

$$H_{\text{eff}} = \underbrace{\frac{A}{\mu_0 M_s} (\nabla^2 \vec{m})}_{\text{Exchange field}} - \underbrace{\frac{1}{\mu_0 M_s} \frac{\partial g_K}{\partial \vec{m}}}_{\text{Anisotropy field}} + \underbrace{\vec{H}_{\text{dip}}}_{\text{Magnetostatic field}} + \underbrace{\vec{H}_{\text{ext}}}_{\text{Zeeman field}}. \quad (2.34)$$

Replacing the effective field H_{eff} in Eq. (2.32) with the individual contributions introduced before, reveals that the equation is in fact an integro-differential equation. The calculation of the magnetostatic field requires solving an integral with the magnetization configuration \vec{m} itself as part of the integrand. Therefore, the ground state can only be calculated analytically for a few examples. Commonly, the magnetic ground state is obtained by numerical methods.

2.2. Magnetization Dynamics

This section is devoted to the dynamic excitations of the magnetization. At first, uniform excitations in a macro-spin model will be discussed. This will govern the basics of ferromagnetic resonance (FMR). Afterwards, spatially non-uniform excitation will be described, leading to the spin-wave theory.

2.2.1. Equation of Motion for Macro-Spins

At first glance, the problem to derive the equation of motion from macro-spins seems to involve quantum mechanics. However, as shown by various authors, only the basic equation has to be formulated within the framework of the quantum theory. Since a large number of spins has to be considered, the correspondence principle provides a semi-classical solution [61–63]. Therefore, classical mechanics are sufficient to calculate an appropriate equation of motion for macro spins.

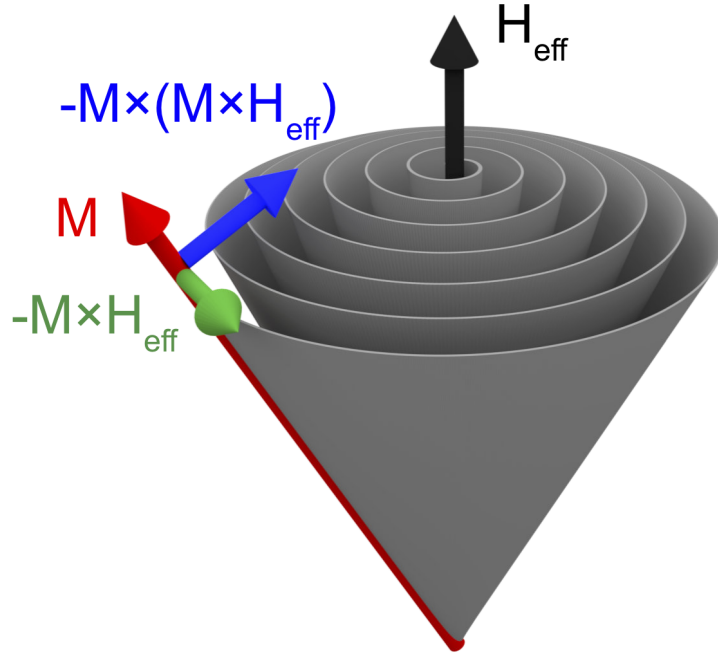


Figure 2.2.: Trajectory of the magnetization around the effective field direction.

The starting point is the well-known relation between the torque \vec{T} and the rate of change of the angular momentum \vec{L} , usually referred to as the rotational analog to Newton's 2nd law [64]:

$$\vec{T} = \frac{d\vec{L}}{dt}. \quad (2.35)$$

Almost the total angular momentum in a ferromagnetic material is carried by the spin \vec{S} . Therefore, we can replace the total angular momentum \vec{J} with the spin momentum \vec{S} and use the relation between the magnetization \vec{M} and the spin \vec{S}

$$\vec{M} = -\gamma\vec{S}. \quad (2.36)$$

Here, γ denotes the already introduced gyromagnetic ratio. Since the torque exerted on the magnetization \vec{M} is given by the effective magnetic field \vec{H}_{eff} we obtain

$$\frac{d\vec{M}}{dt} = -\mu_0\gamma [\vec{M} \times \vec{H}]. \quad (2.37)$$

With appropriate starting conditions this equation describes the persistent precession of the magnetization \vec{M} around the effective field \vec{H}_{eff} .

However, this result is not observed in realistic systems. On the microscopic scale, one could interpret the persistent precession as an infinite lifetime of a spin. To solve this issue,

dissipation of the spins or better of the magnetization has to be included. This damping term was phenomenologically included by Gilbert [65]. This results in the complete Landau-Lifshitz-Gilbert equation:

$$\frac{d\vec{M}}{dt} = -\gamma\mu_0 \left[\vec{M} \times \vec{H}_{\text{eff}} \right] - \frac{\alpha}{M_s} \left[\vec{M} \times \frac{d\vec{M}}{dt} \right]. \quad (2.38)$$

Here, α denotes the Gilbert damping constant. The resulting trajectory of the magnetization is depicted in Fig. 2.2. Important to note is that the length of the magnetization vector \vec{M} is conserved. The trajectory, therefore, is constrained to the surface of a sphere. To obtain the effective field, the first variation of the free energy F with respect to the magnetization has to be calculated [65]

$$H_{\text{eff}} = -\nabla_{\vec{M}} F. \quad (2.39)$$

Since only a single spin is considered, the free energy is equal to the total energy derived in Section 2.1.

To obtain the resonance equation needed to understand and evaluate FMR experiments, Eq. (2.37) can be expressed linearly in terms of the spherical coordinates. The obtained relations read [66]:

$$\frac{d\theta}{dt} = \gamma\mu_0 H_{\text{eff}}^{(\varphi)}, \quad (2.40)$$

$$\frac{d\varphi}{dt} \sin\theta = -\gamma\mu_0 H_{\text{eff}}^{(\theta)}. \quad (2.41)$$

Here, $H_{\text{eff}}^{(\varphi)}$ and $H_{\text{eff}}^{(\theta)}$ denote the azimuthal and polar components of the effective field, respectively. As already discussed above, the effective field is directly related to the free energy F , and therefore, the effective field components read

$$\mu_0 H_{\text{eff}}^{(\theta)} = -\frac{1}{M_s} F_{\theta}, \quad (2.42)$$

$$\mu_0 H_{\text{eff}}^{(\varphi)} = -\frac{1}{M_s \sin\theta} F_{\varphi}. \quad (2.43)$$

F_{θ} and F_{φ} denote the partial derivatives of the free energy F . Using these equations, the equilibrium angles θ_0 and φ_0 of the magnetization in the effective field can be obtained. To calculate the resonance equation, small deviations from equilibrium have to be assumed

$$\delta\theta(t) = \theta(t) - \theta_0, \quad (2.44)$$

$$\delta\varphi(t) = \varphi(t) - \varphi_0. \quad (2.45)$$

2. Fundamentals

To describe the excitations around the minimum of the free energy, given by the equilibrium angles, the free energy has to be expanded linearly around this minimum

$$F_\theta = F_{\theta\theta}\delta\theta + F_{\theta\varphi}\delta\varphi, \quad (2.46)$$

$$F_\varphi = F_{\varphi\theta}\delta\theta + F_{\varphi\varphi}\delta\varphi, \quad (2.47)$$

which includes the second derivatives of the free energy F_{ij} with respect to the equilibrium angles. By combining the presented equations, we obtain a coupled system of equations of motion

$$\frac{M_s}{\gamma} \sin\theta_0 \delta\dot{\theta} = F_{\varphi\theta}\delta\theta + F_{\varphi\varphi}\delta\varphi, \quad (2.48)$$

$$\frac{M_s}{\gamma} \sin\theta_0 \delta\dot{\varphi} = F_{\theta\theta}\delta\theta + F_{\theta\varphi}\delta\varphi. \quad (2.49)$$

By assuming a periodic solution in time for $\delta\theta$ and $\delta\varphi$, the system of equations can be solved for the resonance frequency ω_{res}

$$\omega_{\text{res}} = \gamma H_{\text{eff}} = \frac{\gamma}{M_s \sin\theta_0} [F_{\theta\theta}F_{\varphi\varphi} - F_{\theta\varphi}^2]. \quad (2.50)$$

The presented approach to obtain the resonance frequency $\omega = 2\pi f$ was developed by Smit and Beljers [67] and Suhl [68] simultaneously. However, Suhl provided a generalization of the method relying on the curvature tensor in arbitrary coordinates:

$$\omega = -\frac{\gamma}{M_s} (\det\Delta f)^{\frac{1}{2}}. \quad (2.51)$$

By using spherical coordinates the curvature tensor Δf can be written as

$$\det\Delta f = \frac{1}{\sin\theta_0} \begin{vmatrix} F_{\theta_0\theta_0} & F_{\theta_0\varphi_0} \\ F_{\varphi_0\theta_0} & F_{\varphi_0\varphi_0} \end{vmatrix}, \quad (2.52)$$

resembling the resonance equation derived above. The obtained equation has no solution for specific energy systems for $\theta_0 = 0^\circ$. Here the term energy system usually refers to the specific symmetry or interaction of the investigated system. This divergence was solved by Baselgia *et al.* [69], expanding the resonance equation using trigonometric identities. The resulting equation reads

$$\omega = \frac{\gamma}{M_s} \left[F_{\theta_0\theta_0} \left[\frac{F_{\varphi_0\varphi_0}}{\sin^2\theta_0} + \frac{\cos\theta_0}{\sin\theta_0} F_{\theta_0} \right] - \left[\frac{F_{\theta_0\varphi_0}}{\sin\theta_0} - \frac{\cos\theta_0}{\sin\theta_0} \frac{F_{\varphi_0}}{\sin\theta_0} \right]^2 \right]^{\frac{1}{2}}. \quad (2.53)$$

To evaluate experiments performed in this thesis, two different energy systems: (i) exchange biased ferromagnetic bilayer and (ii) interlayer exchange coupled ferromagnetic bilayer, are needed:

1. Exchange biased ferromagnetic bilayer without interlayer exchange coupling

Additionally to the energy contribution derived above, the influence of an antiferromagnetic layer, the so-called exchange bias, has to be considered. Such exchange-biased samples were investigated in this thesis. The exchange bias energy density is given by

$$\varepsilon_{\text{eb}} = K_{\text{eb}} \sin^2 \theta \cos \varphi, \quad (2.54)$$

where K_{eb} is the exchange bias constant. By applying the formalism given by Eq. (2.53) the resonance equation can be derived

$$\begin{aligned} \left(\frac{\omega}{\gamma}\right)^2 = & \left\{ \mu_0 H [\sin \theta_{\text{H}} \sin \theta \cos(\varphi - \varphi_{\text{H}}) + \cos \theta_{\text{H}} \cos \theta] \right. \\ & \left. - \cos 2\theta \left[\mu_0 M_{\text{eff}} + \frac{2K_{2\parallel}}{M_{\text{s}}} \cos^2(\varphi - \varphi_{\text{u}}) + \frac{2K_{\text{eb}}}{M_{\text{s}}} \cos \varphi \right] \right\} \times \\ & \left\{ \mu_0 H [\sin \theta_{\text{H}} \sin \theta \cos(\varphi - \varphi_{\text{H}}) + \cos \theta_{\text{H}} \cos \theta] \right. \\ & \left. - \cos^2 \theta \left[\mu_0 M_{\text{eff}} + \frac{2K_{2\parallel}}{M_{\text{s}}} \cos^2(\varphi - \varphi_{\text{u}}) + \frac{2K_{\text{eb}}}{M_{\text{s}}} \cos \varphi \right] \right. \\ & \left. + \frac{2K_{2\parallel}}{M_{\text{s}}} \cos(2(\varphi - \varphi_{\text{u}})) + \frac{K_{\text{eb}}}{M_{\text{s}}} \cos \varphi \right\} \\ & - \left[\frac{K_{2\parallel}}{M_{\text{s}}} \sin(2(\varphi - \varphi_{\text{u}})) + \frac{K_{\text{eb}}}{M_{\text{s}}} \sin \varphi \right]^2 \cos^2 \theta. \end{aligned} \quad (2.55)$$

Here, the angles θ_0 , φ_0 , θ_{H} and φ_{H} denote the magnetization and the magnetic field angles, respectively. To extract the material parameters, such as the effective magnetization M_{eff} , the in-plane uniaxial anisotropy $\frac{K_{2\parallel}}{M_{\text{s}}}$ and the exchange-bias field $\frac{K_{\text{eb}}}{M_{\text{s}}}$, the corresponding free energy density is numerically minimized to obtain the equilibrium magnetization angles θ_0 and φ_0 . Using this input, the resonance condition Eq. (2.55) is solved analytically to calculate the resonance field $\mu_0 H_{\text{res}}$.

2. Ferromagnetic bilayer with interlayer exchange coupling

The total energy density for a coupled bilayer is given by

$$\varepsilon = \varepsilon_{J_1} + \sum_{i=1}^2 d_i \left[-M_i \mu_0 H \eta_z^{(i)} + \varepsilon_{\text{Aniso},i} \right] \quad (2.56)$$

with

$$\eta_z^{(i)} = \sin \theta_H \sin \theta_i \cos(\varphi_i - \varphi_H) + \cos \theta_H \cos \theta_i,$$

$$\varepsilon_{\text{Aniso},i} = -(2\pi M_i^2 - K_{2\perp,i}) \sin^2 \theta_i - K_{2\parallel,i} \sin^2 \theta_i \cos^2(\varphi_i - \varphi_{u,i})$$

and

$$\begin{aligned} \varepsilon_{J_1} = & -J_1 [\sin \theta_1 \sin \theta_2 \cos(\varphi_1 - \varphi_2) + \cos \theta_1 \cos \theta_2] \\ & - J_2 [\sin \theta_1 \sin \theta_2 \cos(\varphi_1 - \varphi_2) + \cos \theta_1 \cos \theta_2]^2. \end{aligned}$$

Here, M_i corresponds to the saturation magnetization for layer i , $K_{2\perp,i}$ to the out-of-plane uniaxial anisotropy and $K_{2\parallel,i}$ to the in-plane uniaxial anisotropy. Furthermore, the coupling between the two layer is given by the interlayer exchange coupling constants J_1 (bilinear coupling) and J_2 (biquadratic coupling). Additionally, the thickness d_i of each ferromagnetic layer i influences the coupling. Again, the energy density is numerically minimized with respect to the magnetization angles θ_1 , θ_2 , φ_1 , and φ_2 . The resonance equation is obtained in the same framework as presented above. Since two ferromagnetic layers have to be considered the determinant has 16 entries for this case, resulting in a quartic equation for the resonance frequency [70]

$$\frac{\omega^4}{\gamma_1^2 \gamma_2^2} - b \frac{\omega^2}{\gamma_1 \gamma_2} + c = 0. \quad (2.57)$$

The corresponding resonance equation (2.57) is solved numerically and fitted to the experimental data sets. The coefficients b and c are listed in the appendix A.1.

2.2.2. Spin Waves

So far, only the dynamics of a single spin or an averaged macro-spin have been considered. Since a magnetic body contains many of individual spins or better magnetic moments, one can understand the macro-spin solution of Eq. (2.37) as a motion of all spins with the identical phase ϕ . It is clear that this equation can be solved by a harmonic time-dependent magnetization $\vec{M} = \vec{M}_0 + \vec{m}e^{i\omega t}$. However, solutions of the form $\vec{M} = \vec{M}_0 + \vec{m}e^{i(\omega t + \phi(\vec{r}))}$ are also allowed. Such solutions are called *spin waves*. Since the solution with identical phase for every spin has infinite wavelength, the wave number k corresponding to it is zero, ($k = 0$). All other cases can be classified by $k \neq 0$, defined by the wavelength λ .

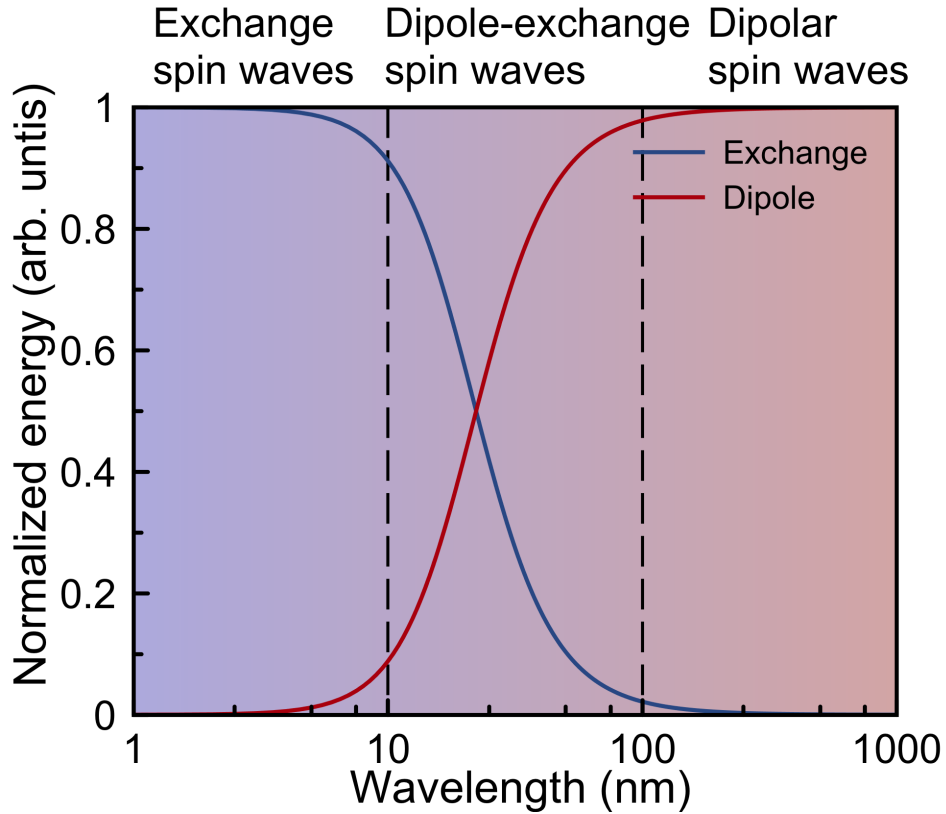


Figure 2.3.: Renormalized energy contribution for spin waves as a function of wave length.

Over the course of this section the classification of spin waves and their theoretical description in the form of the dispersion relation will be introduced and thereby focusing on magnetic thin films.

Spin waves can be classified according to different properties, such as wavelength λ or the orientation of the magnetization \vec{M} with respect to the propagation direction \vec{k} .

The exchange energy and the magnetostatic energy, introduced in Section 2.1, depend on the wavelength of the spin wave. Solving the exact Heisenberg Hamiltonian yields the eigen energies $\varepsilon(k) = 2JS[1 - \cos k]$, with the exchange integral J and the spin quantum number S [71]. In the limit of small wave numbers or long wavelengths, the dispersion relation can be approximated by $\omega \propto k^2$. The wave number dependence of the magnetostatic field is complex to solve. Both, the Landau-Lifshitz equation and the Maxwell equations have to be solved simultaneously within the linear regime. The resulting energy contribution reads [29]

$$E_{\text{dipole}} = \frac{1}{2} \mu_0 M_s^2 \left(\frac{1 - e^{-kd}}{kd} \right) \quad (2.58)$$

with $\mu_0 M_s^2$ saturation polarization, k the wave number and d the film thickness.

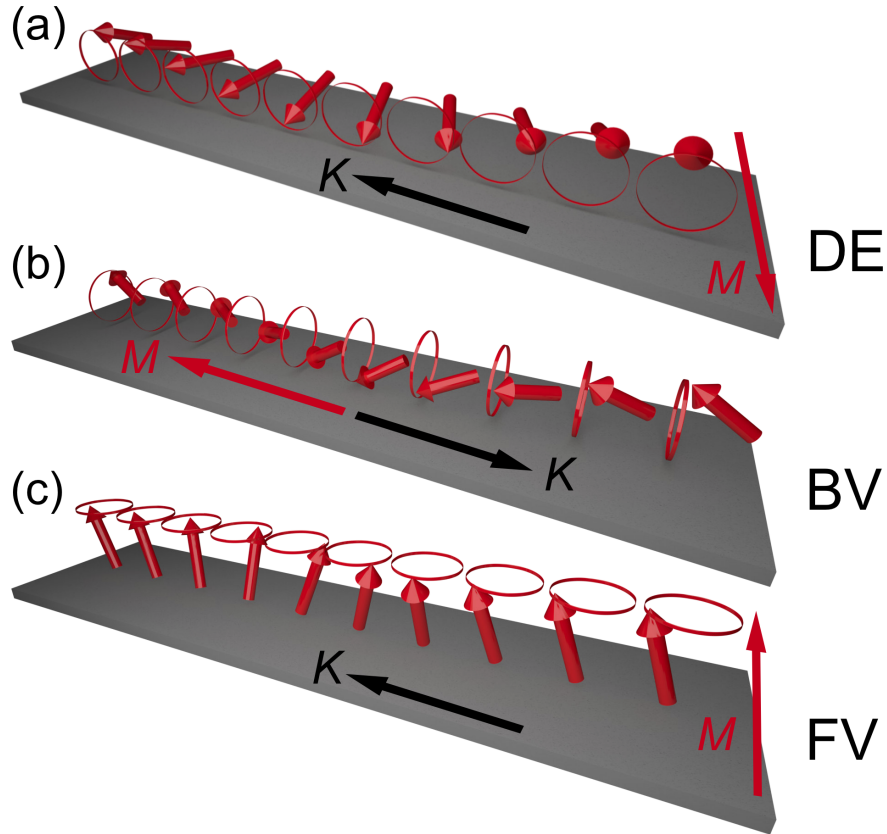


Figure 2.4.: Sketch of (a) Damon-Eshbach, (b) backward-volume and (c) forward-volume spin waves.

Both energies for a 10 nm thin $\text{Ni}_{80}\text{Fe}_{20}$ magnetic film, renormalized to the total energy, are shown in Fig. 2.3. As indicated in the figure, three regimes can be defined. For very small wavelengths the exchange energy dominates the total energy of the spin wave. In this limit, neighboring spins enclose a large angle with respect to each other, resulting in a strong increase in the exchange energy. For intermediate wavelengths in the range between $\lambda \approx 10$ nm and $\lambda \approx 100$ nm, both exchange and magnetostatic energy equally contribute. Therefore, these spin waves are termed dipole-exchange spin waves. For large wavelengths, the tilting angle of neighboring spins is very small, resulting in negligible exchange energy. However, the magnetostatic field, and therefore, the energy is a long-range interaction, dominating at such large wavelengths.

Additionally to the wavelength, spin waves can be classified depending on the relative orientation of the magnetization \vec{M} and the wave vector \vec{k} . The spin wave dispersion relation can be obtained for arbitrary orientation of \vec{M} with respect to \vec{k} and the resulting dispersion is known to be highly anisotropic [72]. However, three principle orientation provide interesting properties. Spin waves propagation parallel to the magnetization is referred

to as backward-volume (BV) modes ($\vec{k} \parallel \vec{M}$). Waves with the wave vector \vec{k} oriented perpendicular to the magnetization are termed Damon-Eshbach (DE) modes ($\vec{k} \perp \vec{M}$). For completeness it is to mention, that the third principle spin-wave mode with again a perpendicular orientation of \vec{k} and \vec{M} , but with the magnetization \vec{M} perpendicular to the film plane in this case, is named Forward-volume (FV) mode. All these three modes are sketched in Fig. 2.4.

In the following the dispersion relations of DE and BV modes will be discussed briefly.

Backward-Volume Modes

In the case of BV modes, the static magnetization is (anti)-parallel to the propagation direction. The spin-wave dispersion relation derived by Slavin and Kalinikos [72] reads:

$$\left(\frac{\omega}{\gamma}\right)^2 = [\mu_0 H_{\text{eff}} + Dk^2] \left[\mu_0 H_{\text{eff}} + Dk^2 + \mu_0 M_s \left(\frac{1 - e^{-kd}}{kd} \right) \right]. \quad (2.59)$$

Here, $\omega = 2\pi f$ is the spin-wave frequency and $D = 2A/M_s$ the exchange stiffness. The naming property of backward-volume modes is the group velocity $v_g = \frac{\partial \omega}{\partial k}$ for small wave numbers k , which reads

$$\lim_{k \rightarrow 0} v_g = -\mu_0 \gamma \frac{H_{\text{eff}} M_s}{4 \sqrt{H_{\text{eff}} (H_{\text{eff}} + M_s)}}. \quad (2.60)$$

The dipole-dipole interaction leads to a negative slope of the spin-wave dispersion and therefore to a negative group velocity. In contrast to this, the phase velocity $v_p = \frac{\omega}{k}$ is positive. However, the energy transport is directly related to the group velocity, which is *backwards* to the phase velocity v_p . Moreover, such spin-wave modes have similar amplitudes throughout the magnetic body, leading to the term *volume*.

Another interesting property of BV modes is the formation of a minimum in the spin-wave dispersion, due to the dipolar energy. This minimum in the dispersion is directly related to the formation of Bose-Einstein condensates in ferromagnetic films, underlining the bosonic nature of magnons [73].

Damon-Eshbach Modes

Damon-Eshbach modes are defined by the perpendicular alignment of the wave vector \vec{k} and the magnetization \vec{M} [29, 30]. Another commonly used term for such modes is magnetostatic surface modes, arising from the fact that the spin-wave amplitude is confined close to the surface of the magnetic film, if the thickness d is much larger than the exchange

length $\lambda = \sqrt{2A/\mu_0 M_s^2}$. The spin-wave dispersion for DE modes reads [72]

$$\left(\frac{\omega}{\gamma}\right)^2 = \left[\mu_0 H_{\text{eff}} + Dk^2 + \mu_0 M_s \left(1 - \frac{1-e^{-kd}}{kd}\right) \right] \times \left[\mu_0 H_{\text{eff}} + Dk^2 + \mu_0 M_s \left(\frac{1-e^{-kd}}{kd}\right) \right]. \quad (2.61)$$

Evaluating the group velocity for DE modes yields

$$\lim_{k \rightarrow 0} v_g = \mu_0 \gamma \frac{dM_s^2}{4\sqrt{H_{\text{eff}}(H_{\text{eff}} + M_s)}}. \quad (2.62)$$

Since the group velocity is positive, the spin-wave frequency is monotonically increasing. Therefore, no minimum is formed.

2.3. Hydrodynamic Formulation of Magnetization Dynamics

Transport phenomena without dissipation are known in many different fields of physics. This intriguing property occurs in different states of matter. However, one general characteristic all system have in common is: They consist of bosons. Due to the fundamental nature of this class of particles, the possibility of collective quantum states arises. The particles can be considered as a macroscopic wave function introducing one order parameter specific to the investigated system. Since magnons are bosons, many phenomena discovered in different fields of physics might also be observable in ferromagnets. Since several years the condensation of magnons as a Bose-Einstein condensate (BEC) in magnetic materials has been investigated [74–77]. Different methods to produce such condensates have been developed, such as thermal condensation [74] or parallel pumping [77]. Furthermore, recent studies suggest the possibility of dissipationless transport of this BEC in ferromagnetic materials [78]. Nevertheless, this new transport channel in ferromagnetic material is not fully understood.

Another new state of matter was discovered in supercooled liquid Helium [79]. The bosons present in the system formed another macroscopic state, providing the possibility of superfluidic transport. Both BEC and superfluidity are closely related. However, introducing the detailed entanglement of both effects would go beyond the scope of this thesis.

Both BEC, as already shown experimentally, and superfluidity, are theoretically possible in ferromagnets. Besides the well-known magnon transport via spin waves, the possible superfluid transport in magnetic thin films was proposed already by Halperin and Hohenberg [36]. The authors present the transformation of the underlying equations but did not fully consider the consequences of this for the transport. The theory later was refined by Sonin,

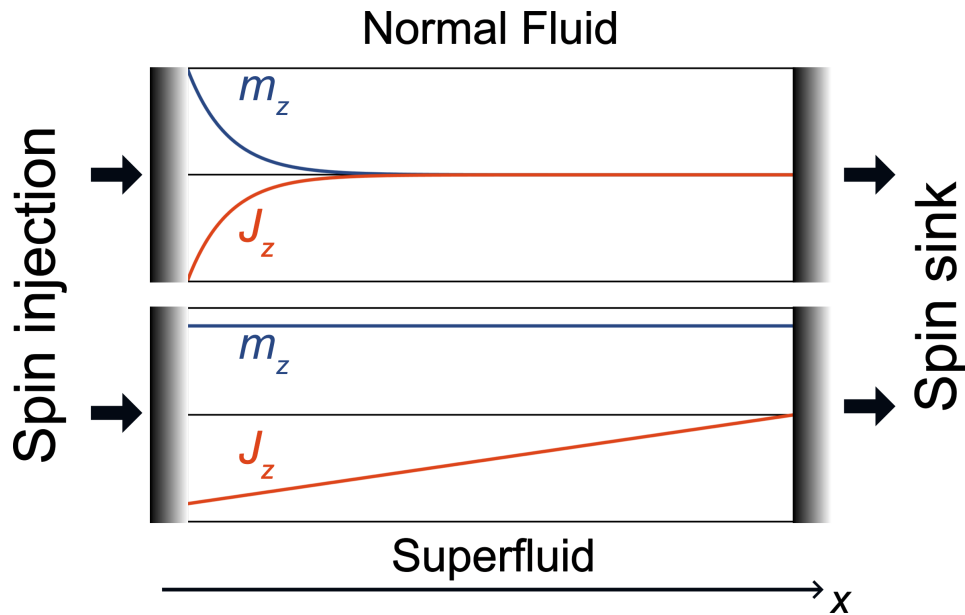


Figure 2.5.: Schematic representation of the transported spin current in non-superfluidic and superfluidic media. The upper panel shows the normal fluid, e.g. magnons. The damping of the m_z component is exponential, and therefore, also the spin current J_z is damped exponentially. In contrast to this superfluidic transport is presented in the lower panel. The spin current is only linearly damped along the transport channel.

where for the first time the term spin superfluid for ferromagnets was introduced [37]. Sonin defined this new state as 2π windings of the magnetization.

The term spin superfluid originates in the different damping behavior of the superfluidic state. The stability of the spin current is given by the topology of the system. For easy-plane ferromagnets the free energy does not depend on the magnetization angle φ defined by the 2π windings. It only depends on the gradient of the magnetization angle $\nabla\varphi$. If one now considers the Noether theorem [80] this should lead to the conservation of a conjugate variable, providing the supercurrent. Furthermore, this property of the free energy can be formulated within the framework of group theory. The symmetry of the energy corresponds to the unitary group $U(1)$. Therefore, the state is topologically protected and exhibits a different damping behavior.

However, one of the main disadvantages of the before-mentioned spin waves, especially for possible applications, is the limited propagation length. Many possible scattering mechanisms limit propagation length. Only for special materials like Yttrium iron garnet (YIG) very long spin wave propagation up centimeters was observed [12]. Nevertheless, the possibility of superfluid transport is intriguing from both fundamental and application points of view.

2. Fundamentals

Due to the advances of spin-torque oscillators and thereby, the deeper understanding of the underlying processes involved, the field of superfluidic transport was considered again in the last years. In the following chapter, a short summary of the analytic theory for the superfluidic transport in easy-plane ferromagnets will be presented.

Starting with the free energy F

$$F = \int dV \left[A (\nabla \vec{m}(\vec{x}))^2 - K_u m_z(\vec{x})^2 \right] \quad (2.63)$$

for an easy-plane ferromagnet will directly lead to coupled hydrodynamic equations [37]. Here, A is the exchange constant and K_u the easy-plane anisotropy constant. As already introduced above, an easy-plane ferromagnet can simply be defined by the ability of rotating the magnetization within one plane of the system, without changing the total energy of it. To gain insight in the dynamics of the ferromagnetic system, the underlying equation of motion [Eq. (2.37)] has to be solved for the here presented total free energy. To simplify the derivation of the hydrodynamic equations, no damping is assumed. For this the functional derivative of Eq. (2.63)

$$\frac{\delta F}{\delta \vec{m}} \equiv \vec{H}_{\text{eff}} = 2A \nabla^2 \vec{m} - 2K_u m_z \hat{z} \quad (2.64)$$

has to be calculated. Introducing the transformation

$$\vec{m} = \left(\sqrt{1 - m_z^2} \cos \varphi, \sqrt{1 - m_z^2} \sin \varphi, m_z \right) \quad (2.65)$$

yields two coupled equations [81, 82]. At first, the equation of motion for the z-component is computed. To simplify the discussion even further, a one-dimensional channel for the superfluid transport is assumed. Therefore, only the derivative along the x-direction contributes. Resulting in

$$\frac{1}{\gamma} \frac{dm_z}{dt} = 2A m_z \partial_x m_z \partial_x \varphi + A (m_z^2 - 1) \partial_{xx} \varphi. \quad (2.66)$$

By applying the reverse chain rule the equation can be shortened:

$$\frac{1}{\gamma} \frac{dm_z}{dt} = \partial_x [A (m_z^2 - 1) \partial_x \varphi]. \quad (2.67)$$

Both in-plane components require more steps to solve the equation. As a result of the transformation shown above, the in-plane components are coupled to the out-of-plane component. Therefore, Eq. (2.67) has to be substituted in the x- and y-component in Eq. (2.65), resulting in:

$$\frac{1}{\gamma} \frac{d\varphi}{dt} = \left(A (\partial_x \varphi)^2 - K_u \right) m_z + \frac{A m_z (\partial_x m_z)^2}{(m_z^2 - 1)^2} - \frac{A \partial_{xx} m_z}{m_z^2 - 1}. \quad (2.68)$$

Approximating this set of coupled equations, by only considering the first order of $\nabla\varphi$, m_z and assuming $m_z \ll 1$ results in

$$\dot{\varphi} = 2\gamma K_u m_z, \quad (2.69)$$

$$\dot{m}_z = 2\gamma A \nabla^2 \varphi. \quad (2.70)$$

These equations directly show the existence of the superfluid state in easy-plane ferromagnets. Interesting to note is that Eq. (2.70) has the form of a continuity equation for m_z [83]. The direct consequence is the conservation of the out-of-plane component in an ideal easy-plane ferromagnet. Furthermore, this property of such systems is directly linked to the conservation of the total energy under rotation within the easy plane. Following this interpretation leads directly to the conclusion, that \dot{m}_z corresponds to a collective spin current

$$\vec{j}_z = -2A \nabla \varphi. \quad (2.71)$$

In the limit of $\alpha = 0$, a dissipationless spin current can flow in the system, if the gradient of the easy-plane angle, $\nabla\varphi$, is non-zero.

One possible solution for Eqs. (2.69) and (2.70) is given by the ansatz

$$m_z(x, t) \equiv \text{const} = m_z, \quad (2.72)$$

$$\varphi(x, t) = \varphi(x) + \Omega t. \quad (2.73)$$

with the precession frequency $\Omega = \gamma K_u m_z$. Hence, Eq. (2.70) can be written as

$$0 = 2\gamma A \nabla^2 \varphi. \quad (2.74)$$

Thus, the solution for $\varphi(x)$ is given by

$$\varphi(x) = \frac{1}{2\gamma A} C_1 x + \frac{1}{2\gamma A} C_2, \quad (2.75)$$

with the integration constants C_1 and C_2 .

The here presented theory easily can be extended to the case of non-zero Gilbert damping. The modified equation reads

$$\dot{\varphi} = 2\gamma K_u m_z + \alpha \dot{m}_z, \quad (2.76)$$

$$\dot{m}_z = 2\gamma A \nabla^2 \varphi - \alpha \dot{\varphi}. \quad (2.77)$$

For the case of non-zero Gilbert damping the stationary solution is also modified by the condition $\partial_{xx}\varphi = \alpha/A\Omega$ [40, 44, 81]. With this is clearly visible, that the dissipation of the

spin current $J_z \propto -\nabla\varphi$ is proportional to the distance. The difference between a normal fluidic state, i. e. a spin wave, and a superfluidic state is depicted in Fig. 2.5. The m_z component of the normal fluid is damped exponentially, resulting in an exponential decay of the carried spin current J_z . In contrast to this, the solution of the superfluid contains a constant out-of-plane component of the magnetization. As discussed above, the solution of the easy-plane angle in case of non-zero damping will have the form $\varphi(x) = Ax^2 + Bx + C$. Therefore, the spin current $J_z \propto -\nabla\varphi(x)$ will depend linearly on x , as depicted in Fig. 2.5.

It is important to note, that the presented analytic approach neglects two important terms: At first, the developed equations lack the excitation term. It is not clear how an excitation region will behave in the presence of the superfluid. Secondly, no long range dipole-dipole interactions are included in the model. Since the superfluid is considered as composed of 2π rotations, the energy landscape is more complex in the presence of dipole-dipole interactions. A simplified picture using the terminology of spin waves can easily be introduced. The spin-wave dispersion is not isotropic due to the magnetostatic field [29, 30]. The two principal directions $\vec{k} \perp \vec{M}$ (Damon - Eshbach configuration) and $\vec{k} \parallel \vec{M}$ (Backward volume geometry) show different dispersion relations for spin waves due to the dipole-dipole interaction in ferromagnetic thin films [84]. Since the superfluid has a coherent transition from the Damon-Eshbach into the Backward-volume configuration, the energy of the system will be affected.

To investigate the two mentioned shortcomings of the analytic theory, extended micro-magnetic simulations have been performed. The results of this study are presented in Chapter 5.

3. Experimental and Numerical Methods

3.1. Ferromagnetic Resonance

The first reported measurement of the ferromagnetic resonance (FMR) was done by Arkadiew in 1919, probing the absorption of microwaves for two parallel wires [85]. Later on, this powerful experimental method was rediscovered in the 1940s, resulting in two independent reports by Zavoisky [86] and Griffiths [87].

Over the last decades, various techniques to measure the FMR have been developed. Each technique has its own advantages and disadvantages. However, classical FMR setups based on a microwave cavity are still present today, providing excellent signal-to-noise ratios, but are usually limited to a single frequency without changing the cavity. Other techniques based on a vector network analyzer (VNA) offer a broad range of frequencies but the signal-to-noise ratio is smaller compared to cavity setups [88].

Moreover, a variety of all-electrical detection methods have been developed, mainly based on the magneto-resistance [89–92].

However, the basic principle of the FMR phenomenon is always the same, and therefore is independent of the detection method.

3.1.1. Broadband CPW-FMR

All measurements presented in this thesis were done using a vector network analyzer (VNA) FMR setup. A detailed description of the setup, including the principle of the VNA can be found in Ref. [93]. The VNA acts as the microwave source and detector simultaneously. Such experimental setups support multiple operation modes to obtain the FMR data. Since the VNA is designed as a broadband source and detector, the excitation frequency can be swept while the sample is placed within a fixed external magnetic field. However, this operation mode requires a tedious calibration of all involved passive as well as active microwave components. Therefore, a second operation mode was utilized in this thesis. The frequency of the microwave source was kept constant and the external magnetic field was swept. This operation mode is identical to classical FMR measurements based on cavity setups.

If the resonance condition is fulfilled the sample will partially absorb the incoming microwave power. Therefore, the transmitted power in case of the resonant excitation will

differ compared to the internal reference of the VNA. This difference is proportional to the change in the high-frequency susceptibility, and can be theoretically described by one or several Lorentzians.

By fitting each recorded spectrum with a Lorentzian function, the resonance field $\mu_0 H_{\text{res}}$ and the linewidth $\mu_0 \Delta H_{\text{pp}}$ can be extracted. With the formulas presented above, the extracted resonance fields can be fitted according to the appropriate energy system, and therefore the material parameters are extracted.

3.2. Numerical Micromagnetism - MuMax³

To understand the often complex processes in ferromagnetic materials many different approaches to simulate this material class have been developed [94–97]. Especially micromagnetic simulations gained popularity during the last years, due to the experimental and technical progress in the fields of spintronics and magnonics. To facilitate the interpretation of experimental data of magnetic micro- or nano-devices, modeling within the framework of micromagnetism provides an easy and reliable tool. The main task of micromagnetic simulations is solving the Landau-Lifshitz-Gilbert equation [98], which is equivalent to

$$\frac{d\vec{M}}{dt} = -\gamma\mu_0 \left[\vec{M} \times \vec{H}_{\text{eff}} \right] - \mu_0 \frac{\gamma\alpha}{(1+\alpha^2)} M_s \left[\vec{M} \times \left(\vec{M} \times \vec{H}_{\text{eff}} \right) \right]. \quad (3.1)$$

Therefore, the effective magnetic field \vec{H}_{eff} has to be computed including all interactions introduced in Chapter 2.1. Moreover, the boundary conditions and requirements on the simulation grid have to be fulfilled.

The growth in the computing power and video memory enabled researchers to perform large-scale micromagnetic simulations on an everyday basis. The past generation of micromagnetic codes still relied on the central processing units (CPU) to compute the magnetization configuration considering all interactions between the magnetic moments. Usually one or more computing nodes, located at a high-performance computing (HPC) cluster, are needed to solve large-scale problems within a reasonable time frame. The costs of such systems easily range up into the tens of thousands of Euros. With the introduction of the *Compute Unified Device Architecture* (CUDA) by Nvidia in February 2007 it was possible to easily use the Graphic processing units (GPUs) for parallel computing.

Besides the intensive parallelism provided by GPUs, micromagnetic simulations based on the finite-difference approach are also accelerated by using fast-Fourier transformations. As visible in Eq. (2.25) the calculation of the magnetostatic field is a convolution of the Green function and the magnetization. The convolution theorem states that a Fourier transformation \mathcal{F} of a convolution is given by the product of the Fourier transformation of the

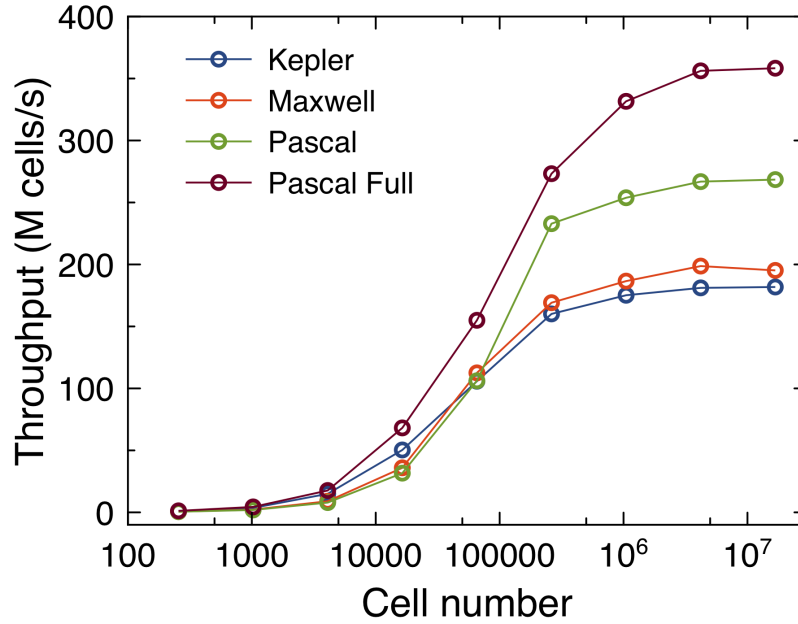


Figure 3.1.: Maximum throughput in millions of cells as a function of the total cell number in MuMax³. Four different GPU generations are compared. The performance regarding micromagnetic simulations was almost doubled between 2014 (Kepler launch) and 2017 (launch full Pascal GPU).

individual factors [99]:

$$\mathcal{F}\{f * g\} = \mathcal{F}\{f\} \cdot \mathcal{F}\{g\}. \quad (3.2)$$

By utilizing this theorem, the magnetostatic field is calculated as the product of the Fourier-transformed Green function and the Fourier-transformed magnetization. A naive implementation for the calculation of the magnetostatic field requires N^2 numerical operations for N cells. The fast-Fourier transformation (FFT) only requires $N \log N$ numerical operations.

The latest GPU generations provide the same performance as full CPU compute nodes with similar or even less cost per node. The performance of different generations for NVIDIA GPUs in MuMax³ is shown in Fig. 3.1. Typical system sizes in simulations are in the area of a few hundred thousands or million cells. Depending on the GPU generation the performance varies between 150 million cells per second (Kepler) and 350 million cells per second (Pascal Full). For 2D simulations the performance gain directly reduces the wall time by the same amount.

The increase of the performance depends on two important factors: (i) Every new GPU generation provides an increase in the number of compute cores and the overall efficiency of each compute core. (ii) The increase of the memory bandwidth highly enhanced the per-

formance of micromagnetic simulations, since the FFT is limited by the memory interface speed [100]. Therefore, it is very useful to upgrade at least every second GPU generation. In the next section the problem of the data evaluation is discussed.

3.2.1. Evaluation of Micromagnetic Simulations

Large-scale simulations need proper numerical tools to evaluate hundreds of gigabytes or even terabytes of data. Therefore, two tools commonly used to evaluate data produced by micromagnetic simulations have been developed during this thesis. Often the dynamic response of the system, usually termed power spectrum and the dispersion relation have to be computed. The developed program provide a time efficient way to calculate both quantities. Abstractly, both programs can be divided into three main routines. At first the data has to be loaded into the main memory. Afterwards, the main routine has to perform mathematical operations for the magnetization vector of each cell. Lastly, the computed spatially dependent quantities have to be written back to the storage system. The details for each step will be discussed for the two programs individually in the next sections.

Power spectrum calculation - MuMax³-pwsp

The calculation of the power spectrum is a common task when evaluating micromagnetic simulations. To obtain the dynamic response of a system, the time dependent magnetization $\vec{m}(\vec{r}, t)$ is recorded and afterwards transformed into the frequency space using an FFT approach. Transforming only the spatially averaged response $\mathcal{F} \langle \vec{m}(t) \rangle_N$, with the number of cells N , can substantially differ from the averaged transformed response $\langle \mathcal{F}(\vec{m}(t)) \rangle_N$. Considering the symmetry of the eigenmodes, the first approach will lead to zero or a small intensity for perfectly symmetric eigenmodes, since the average of the response before the FFT is close to zero. Applying the FFT first to all cells and averaging afterwards the dynamic response solves this issue. To perform an FFT in time for every cell is very challenging.

The presented program was directly implemented into the MuMax³ source code and therefore, shares many functions with the original release. The program was designed to evaluate extremely large data sets within a reasonable amount of time (maximal 8 h per data set with size of 1 TB) and additionally provides easy usability. The user only has to provide a minimal amount of input and the rest is done completely automatically.

The developed program has the following main functions as shown in Fig. 3.2. The magnetization data is loaded from the storage system into the main memory of the host system. Depending on the size of the simulated system, the whole amount can be stored but commonly the transformation has to be done inparts to fit the data into the host memory. Depending on the number of files provided for the transformation the program automatically

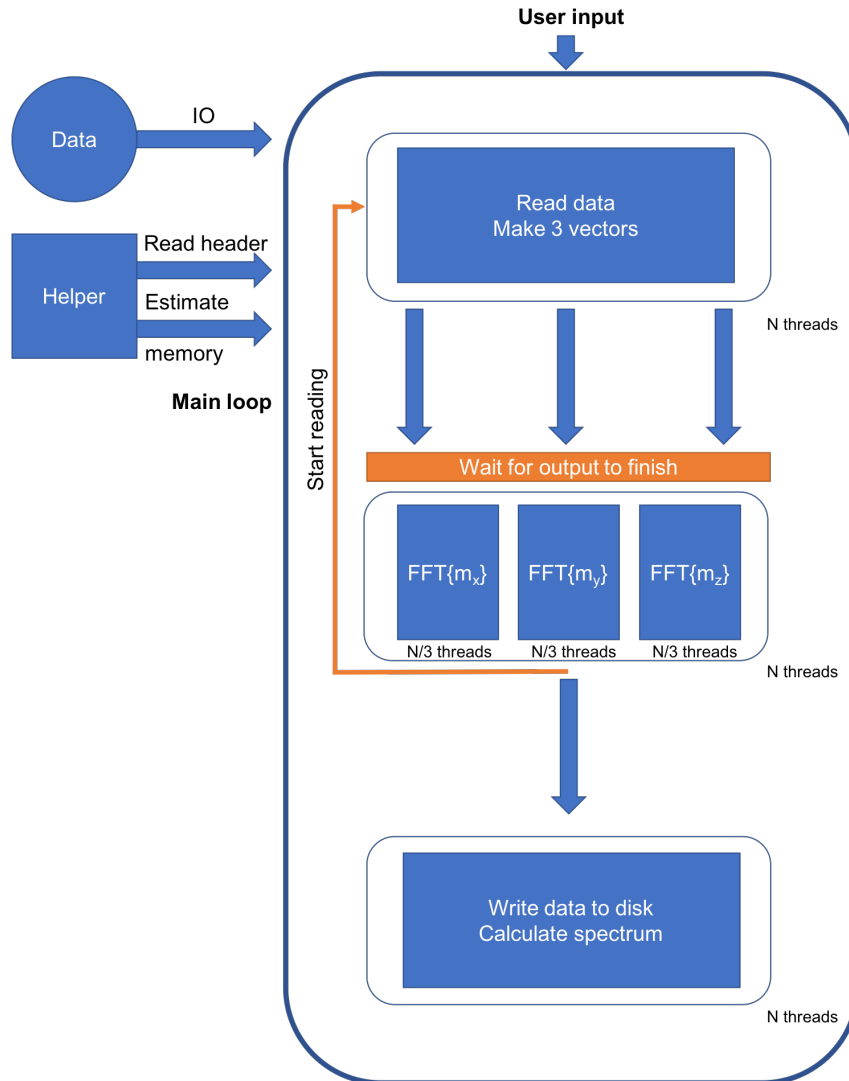


Figure 3.2.: Flow chart of MuMax³-pwsp.

estimates the maximal number of cells which can be loaded into the main memory. The amount of the main memory available is fixed in the source code at 4 GB for the normal release and 16 GB for the HPC release. However, some overhead of each routine will lead to an increase of the memory needed.

Due to the strong increase of the input-output (IO) performance, regarding the development of solid state drives (SSD) and highly parallel data systems, the maximal reading performance can be achieved, by parallelizing the reading operations [101, 102]. To maximize occupancy of each CPU core the reading routine and the separation of the magnetization vector $\vec{m}(\vec{r}, t)$ into the three components are combined into one thread.

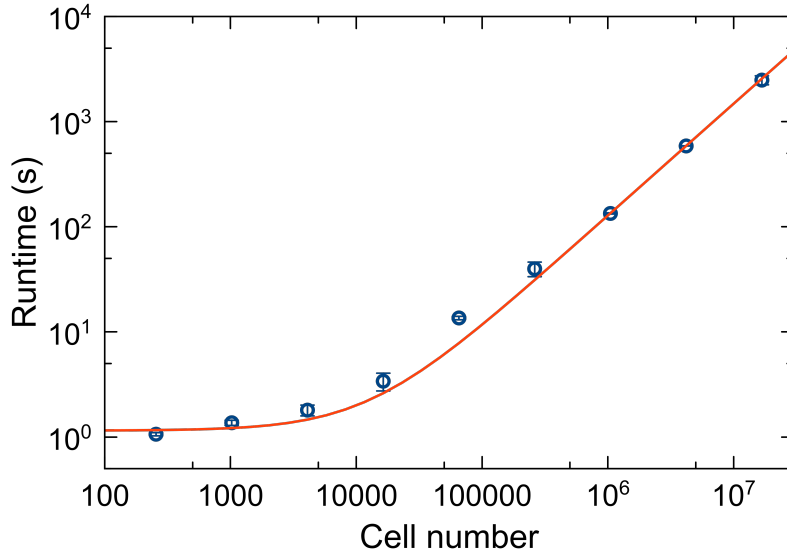


Figure 3.3.: Runtime of MuMax³-pwsp in the HPC release as a function of cells. Both axes are shown in logarithmic scale. The program was executed on the compute node mag007.

The FFT is calculated for each component of the magnetization vector m_i individually using $N/3$ threads. For this, the FFTW3 [103] wrapper originally shipped together with the MuMax³ source code was modified. This modification reduced the amount of host memory needed to perform the transformation, by using the *R2HC* flag of the FFTW3 package. This option in the FFTW3 package provides the ability to store the real and imaginary part in one vector as follows: The first $N/2 - 1$ entries in the vector are the real part of the FFT and the $N/2$ to $N - 1$ entries correspond to the imaginary part. The multi-core implementation of FFTW3 is directly used to calculate the FFT of each component. Therefore, the main functions are executed in the C back-end to provide maximum performance. Both reading and calculation functions are optimized to perform similarly for most common system sizes. The time spent in each function is approximately the same.

The performance critical part is the write-back of the transformed data to the storage system. The writing function can be split into two operations. At first the amplitude $A = \sqrt{\Re(\tilde{m}_i^j)^2 + \Im(\tilde{m}_i^j)^2}$ and the phase $\phi = \arctan(\Im(\tilde{m}_i^j)/\Re(\tilde{m}_i^j))$ are calculated for each transformed component i and every cell j . The calculation of the amplitude A is rather fast, but the phase calculation requires a significant amount of time. The correction of the phase ϕ to map it onto the full 2π range requires several *if-else* statements, strongly increasing the runtime. Therefore, the calculation of the amplitude A and the phase ϕ are parallelized. Depending on the number of CPU cores available, each core has to calculate a subset of the cells. This approach provides a significant increase of the performance of the program.

Nevertheless, storing the data is still open. The writing a single file with multiple threads is not safe¹. Therefore, both amplitude and phase are written using a single thread. Both files are again written within the framework of C.

To validate the newly developed tool, a standard FMR simulation was performed. The investigated system, a Ni₈₀Fe₂₀ square, was homogeneously excited with a sinc-Pulse in time. Standard literature material parameters were used. This pulse form in time provides a box window in the frequency space after the transformation. The cell size of the system was kept constant at $4 \times 4 \times 4 \text{ nm}^3$. Only the cell number N of the system was changed. The ring-down of the magnetization was recorded for 25 ns with a step size of 10 ps. This results in 2500 magnetization configurations taken into account for the evaluation. The integration time was chosen larger than the decay time of the excited magnetization dynamics. The maximal time step in the simulation was fixed to 1 ps to avoid numerical error. The runtime of the program executed on the mag007 compute node in the hypnos cluster of the HZDR was measured four times. The test data was stored on the GSSNAS system directly connected to the compute node by using InfiniBand [104]. The runtime for all four runs of MuMax³-pwsp were averaged.

The performance of Mumax³-pwsp is shown in Fig. 3.3. The error bars correspond to the standard deviation of all four runs. For a small number of cells the runtime is almost constant. This is a direct result of the overhead produced by the massive parallelism of the tool. The largest simulated case of approximately 16 Mio. cells corresponds to roughly 471 GB of data. The runtime for such mid-sized systems is only 42 min. The analysis of the runtime scaling with the number of cells gives an $N \log N$ dependence for large numbers of cells. This is the theoretical maximum for the FFT [103].

As already discussed above, the cell-dependent FFT provides advantages in calculating the power spectrum. To obtain all eigenmodes regardless of their symmetry, the cell-dependent FFT is inevitable. To illustrate this, a prototype system is considered. The dynamic response of a Ni₈₀Fe₂₀ disk with a diameter $d = 500 \text{ nm}$ and thickness $t = 20 \text{ nm}$ was computed. Again standard values of the material parameters were used. The magnetic configuration of the system is given by a magnetic vortex.

The power spectrum and eigenmodes of the magnetic vortex have been computed using at first the cell-dependent approach and, second, the averaged approach. The resulting power spectra are shown in Fig. 3.4. The first three eigenmodes of the system are visible for both approaches. However, with increasing mode number, only the cell-dependent FFT provides reliable results for the eigenmodes in the power spectrum. In the averaged approach almost no signal is present for some eigenmodes (encircled area in Fig. 3.4).

¹Each thread has to remember the position of the data per thread in the file. Therefore, extremely large integer numbers occur and sometime overflow the variable storage.

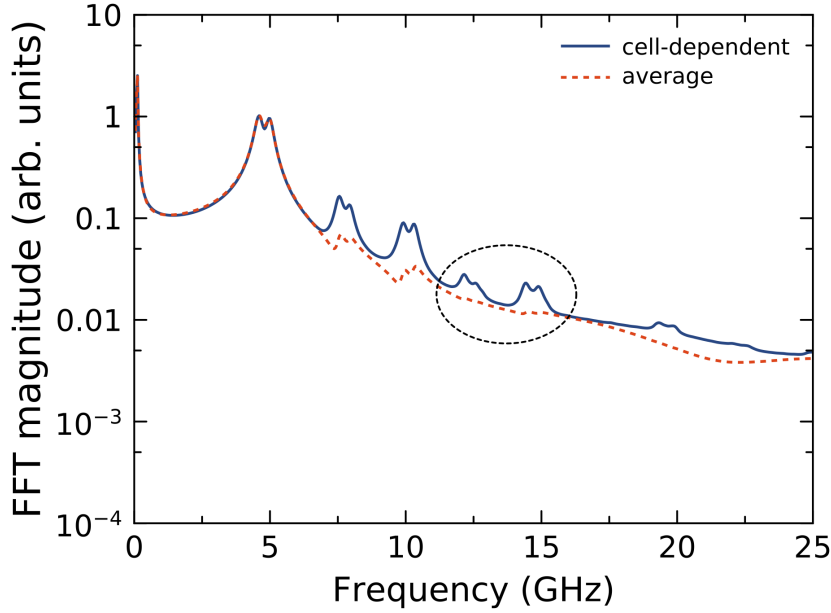


Figure 3.4.: Power spectrum of the magnetic vortex. The material parameters were chosen according to literature values for $\text{Ni}_{80}\text{Fe}_{20}$. The dashed red and solid blue lines show the averaged and cell-dependent approach, respectively. The encircled area shows the difference between both approaches. Some eigenmodes are suppressed in the averaged approach.

The massive parallelism of the tool provides an additional source for errors. For small a number of cells, the numerical noise in the calculated spectrum strongly increases. Since every CPU core utilized for the calculations has a slightly different round error, the total error accumulates. However, common systems have a larger number of cells, and therefore this is not an important issue. All other numerical errors of the tool can be ignored since all calculation are executed with double precession accuracy and the input data provide by MuMax³ is only single precession accuracy.

Dispersion relation calculation - MuMax³-dispersion

A second very important task is the calculation of the spin-wave dispersion relation. However, the conventional approach of local excitation with a CW frequency and extracting the corresponding wave number is tedious and time-consuming. A similar approach applied for the power spectrum using a sinc-pulse can also be utilized here. Therefore, a program is needed, which provides a two-dimensional FFT in space and time. During this thesis the program MuMax³-dispersion was developed for this purpose. A large part of the source code is based on MuMax³-pwsp. However, some fundamental changes were necessary. Es-

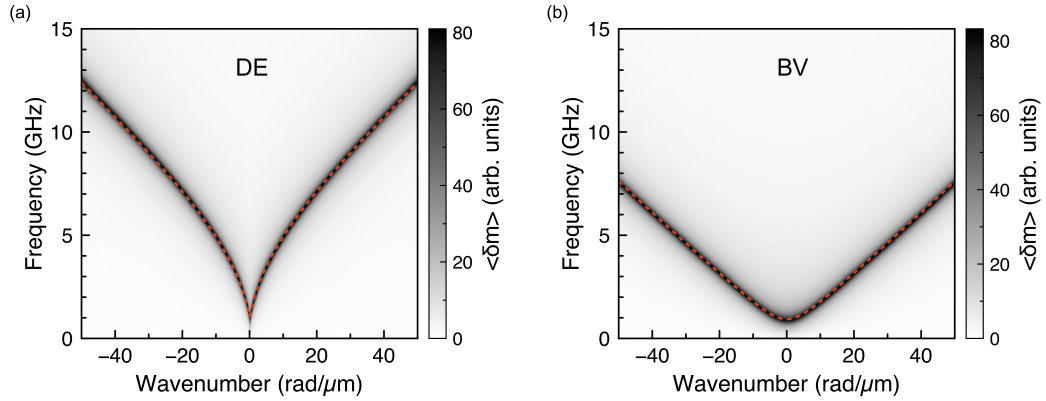


Figure 3.5.: Simulated dispersion relations of a 5 nm thick $\text{Ni}_{80}\text{Fe}_{20}$ film for (a) $\vec{k} \perp \vec{M}$ and (b) $\vec{k} \parallel \vec{M}$. The red solid lines show the analytic calculations of the dispersion relation based on the Eqs. (2.59) and (2.61)

pecially in the reading function several major changes have been implemented. Instead of an arbitrary number of cells of all time steps, a complete row of cells in the direction of the spin-wave propagation has to be loaded for all time steps to arrive at a 2D transformation. Two different versions for solving this issue have been developed.

The first version loads a single row of cells for all time steps. Since many read operations are needed the performance especially on the hypnos cluster was not sufficient. The second version, mainly developed for the hypnos cluster, loads multiple rows of cells. Since the FFT is performed on the two-dimensional structure of a single row in space and all time steps, additional treatment of the data structure is needed. The two-dimensional transformation is performed multiple times, where every time a part of the large data structure is stored in a buffer. After the transformation of the buffer data, the results are written back into the large data structure. However, since all three components can be treated individually both mentioned operations have been parallelized.

Another major difference is the application of a Hann window to the magnetization data in space and time. This window function is given by

$$w(n) = \frac{1}{2} \left[1 - \cos \left(\frac{2\pi n}{N-1} \right) \right]. \quad (3.3)$$

Here N is the number of samples and n the index of the corresponding frame. The number of samples is either provided by the discrete cell size in space or the discrete saving period in time. Each cell is multiple with the corresponding window function in time and space before the transformation. For this two one-dimensional Hann windows are multiplied with the original magnetization data while loading the data into the main memory. The application

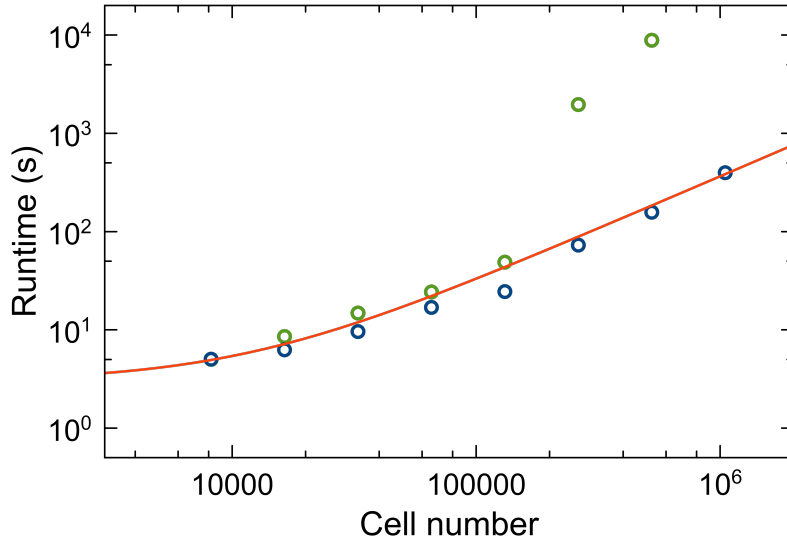


Figure 3.6.: Runtime of MuMax³-dispersion for both releases as a function of cells. Both axes are shown in logarithmic scale. The program was executed on the compute node mag006. The blue open symbols correspond to the HPC release of the program compiled for 64 GB of RAM. The green open symbols show to runtime for the standard release using 4 GB of RAM.

of this filter reduces the power loss with increasing frequency or wave number [105]. An example for the application of a window function is provided in the appendix A.3.

The transformation itself is very similar to the MuMax³-pwsp program mentioned before. Only the one-dimensional FFT in time is replaced with a two-dimensional FFT in space and time. Since the reconstruction of mode profiles is not needed for dispersion simulations, no space-dependent data is stored. However, the dispersion relation, as a sum over all cell rows of the Fourier amplitude, is stored as a matrix. An example for a simulation evaluated with the MuMax³-dispersion is shown in Fig. 3.5. Both Damon-Eshbach and backward-volume configurations have been computed for a 5 nm thick Ni₈₀Fe₂₀ film. The excitation was modeled as a sinc-pulse in space and time. In integration time was set to 25 ns. The magnetization configuration was stored every 10 ps. Both calculated dispersion relations perfectly resemble the theoretical predicted results (see Chapter 2.2.2).

To compare the performance of both versions the example mentioned above was computed and evaluated for different cell numbers. The cell number along the propagation direction of the spin wave (x -direction) was fixed to 2048. The second dimension N_y was changed from 4 to 512. The scaling for the HPC version again follows the theoretical maximum $N \log N$. However, the first simple version shows a very strong non-linear scaling for large cell numbers. For smaller cell numbers both version perform similarly. Loading the

data row by row produces a larger overhead while opening and closing all files multiple times and therefore, significantly slows down the program.

4. Nonreciprocal Spin Wave Emission in Magnetic Bilayers

As already briefly discussed in Chapter 2.2.2, SWs propagating in DE geometry exhibit a nonreciprocity regarding their amplitude distribution along the thickness of the magnetic film. For counter-propagating SWs, the largest amplitude is either located close to the top interface ($k > 0$) or the bottom interface ($k < 0$).

In recent years the general phenomenon of nonreciprocal transport became very popular [106–108]. In this case, one or several physical properties are different regarding the transport in opposite directions. Especially in the field of electronics and photonics this nonreciprocal transport is heavily investigated, leading to possible applications in electronic or photonic devices as isolators, circulators, and gyrators [109–111].

Moreover, ferromagnetic systems are also known to exhibit nonreciprocal propagation of SWs with respect to their wavelength. The already discussed case of DE SWs can also show nonreciprocity regarding the SW wavelength. Modifying the material parameters of both surfaces will inevitably lead to a different energy landscape and therefore, to different SW wavelengths [31, 112–116].

Recently, it was shown that dipolar interactions can lead to nonreciprocal properties in ferromagnetic nanostructures and ferromagnetic nanotubes [117, 118], underlining the important role of the dipole-dipole interactions in ferromagnetic bodies. The fabrication of the proposed nanostructures and the stabilization of the proper groundstate is rather challenging. So far, no experimental report is available, measuring the nonreciprocal SW dispersion in ferromagnetic nanotubes.

Therefore, many research groups focused their attention on the first theoretically predicted Dzyaloshinskii-Moriya interaction (DMI) arising from the symmetry break at interfaces or within the bulk [119, 120]. The influence of the DMI on the SW dispersion was heavily investigated in recent years [47, 121–126]. However, besides materials with a broken inversion-symmetry, mainly ultra-thin ferromagnetic films capped with a heavy-metal layer, providing a broken symmetry at the interface, were investigated. Since interfacial DMI is proportional to $1/t_{\text{FM}}$ [47], very small values of the layer thickness are required, making the experimental validation of large wavelength differences challenging.

In this thesis, a different way of inducing a nonreciprocal SW dispersion was investigated. Inspired by the work presented in Ref. [16], the effect of the dipole-dipole interaction in an antiferromagnetically aligned layers was investigated.

Regarding the nonreciprocal transport, three important questions can be formulated:

1. Is it possible to derive an analytic formula to describe the nonreciprocal SW dispersion relation including uniaxial anisotropy for antiferromagnetically aligned bilayer?
2. What are the limits of the analytic description in comparison to full-scale micromagnetic simulations?
3. Can samples be designed to validate the proposed theoretical framework?

Two different prototype systems were numerically investigated in this thesis and supported by experimental investigations. The systems are extended bilayers, where the antiparallel alignment is either achieved by the coupling of one layer to an antiferromagnet or using interlayer-exchange coupling. The spin-wave dispersion relation was investigated by means of BLS. The second system is a microstructured interlayer-exchange coupled magnetic bilayer. The microstructuring leads to the formation of a spin texture, giving rise to additional topological effects for the spin-wave emission.

4.1. Theoretical Description

The analytical description was mainly developed by R. A. Gallardo, A. Roldán-Molina and P. Landeros¹.

Fig. 4.1 depicts a schematic diagram of the bilayer structure, including the coordinate system used throughout the calculations. The investigated system is composed of two ferromagnetic layers with homogenous magnetization $\vec{M}^{(1)}$ and $\vec{M}^{(2)}$, respectively. Both layers might have different material and geometric parameters. To simplify the analytic calculations, a local coordinate system is introduced, where the local x-axis $\hat{X}^{(i)}$ always points along the local magnetization direction.

All interactions, such as dipole-dipole interactions, exchange interaction, interlayer exchange interaction and local anisotropies are considered in the model.

To obtain the dispersion relation, the Landau-Lifshitz equation (2.37) is linearized. Therefore, the magnetization \vec{M}^i and the corresponding effective field $\vec{H}_{\text{eff}}^{(i)}$ for each layer are written as

$$\vec{M}^{(i)}(\vec{r}, t) = M_s^{(i)} \hat{X}^{(i)} + \vec{m}^{(i)}(\vec{r}, t) \quad (4.1)$$

$$\vec{H}^{(i)}(\vec{r}, t) = H_{\text{eff}}^{(i)} \hat{X}^{(i)} + \vec{h}_{\text{eff}}^{(i)}(\vec{r}, t). \quad (4.2)$$

¹Departamento de Física, Universidad Técnica Federico Santa María, Avenida España 1680, Valparaíso, Chile

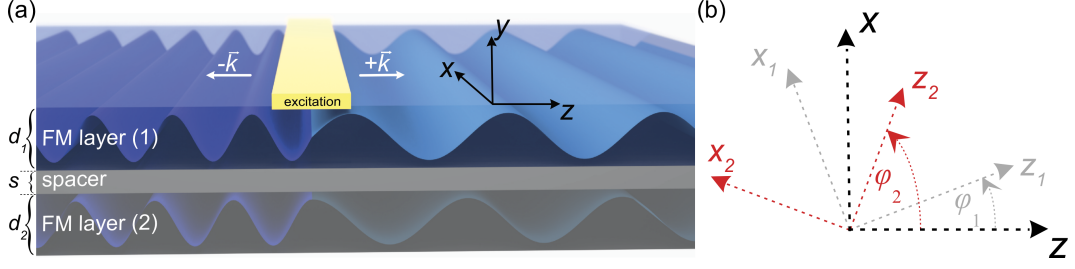


Figure 4.1.: (a) depicts a sketch of the bilayer system in the antiparallel state. The spin waves are excited below the antenna region (gold area) and travel in the direction of positive and negative wave numbers. The different color of the waves indicates the wavelength difference given by the nonreciprocity. (b) shows the in-plane components of the global coordinate system. The local coordinate system utilized for the calculation is shown in grey for layer 1 and red for layer 2, respectively.

Here, $\vec{m}^{(i)}(\vec{r}, t)$ and $\vec{h}_{\text{eff}}^{(i)}(\vec{r}, t)$ are the dynamic magnetization and the corresponding dynamic effective field for the layer i , respectively. The resulting linearized equations of motion are:

$$i\frac{\omega}{\gamma}m^{Y_i}(\vec{r}) = -m^{Z_i}(\vec{r})H_{\text{eff}}^{X_i} + M_s^{(i)}h_{\text{eff}}^{Z_i}(\vec{r}), \quad (4.3)$$

$$i\frac{\omega}{\gamma}m^{Z_i}(\vec{r}) = m^{Y_i}(\vec{r})H_{\text{eff}}^{X_i} - M_s^{(i)}h_{\text{eff}}^{Y_i}(\vec{r}), \quad (4.4)$$

where a harmonic time dependence of the dynamic magnetization was assumed $\vec{m}(\vec{r}, t) = \vec{m}(\vec{r})e^{i\omega t}$. Since one is interested in the dispersion relation $\omega(\vec{k})$, one can transform the dynamic magnetization $m(z) = \vec{m}(k)e^{ikz}$ and effective field $h_{\text{eff}}(z) = \vec{h}_{\text{eff}}(k)e^{ikz}$ into the reciprocal k -space. Additionally, the propagation direction was fixed to the z -direction with $k = \vec{k}\hat{z}$.

The resulting equation can be written in matrix form

$$i\frac{\omega}{\gamma}\vec{m}(k) = \tilde{A}\vec{m}(k), \quad (4.5)$$

reducing the calculation to an eigenvalue problem. The matrix elements are presented in the appendix A.2.

The eigenvalue problem can be solved fully analytically for identical layers with the thickness $d = d_1 = d_2$. The dispersion relation for two antiparallel aligned layers is given by the following expressions

$$f_{m_1}(k) = \frac{\gamma}{2\pi} \left\{ -G(k) + \sqrt{[G_1(k) - G(|k|)][G_2(k) - G(|k|) - 2C_J]} \right\}, \quad (4.6)$$

$$f_{m_2}(k) = \frac{\gamma}{2\pi} \left\{ G(k) + \sqrt{[G_2(k) + G(|k|)][G_1(k) + G(|k|) - 2C_J]} \right\}, \quad (4.7)$$

where $f_{m_1}(k)$ and $f_{m_2}(k)$ correspond to the acoustic and optical mode of the bilayer system. The individual terms are defined by:

$$\zeta(k) = \frac{\sinh(kd/2)}{kd/2} e^{-|k|\frac{d}{2}}, \quad (4.8)$$

$$G(k) = \frac{kd}{2} \mu_0 M_s \zeta(k)^2 e^{-|k|s}, \quad (4.9)$$

$$G_1(k) = \mu_0 H_u + \mu_0 M_s k^2 \lambda_{\text{ex}}^2 + \mu_0 M_s [1 - \zeta(k)], \quad (4.10)$$

$$G_2(k) = \mu_0 H_u - \mu_0 H_s + \mu_0 M_s k^2 \lambda_{\text{ex}}^2 + \mu_0 M_s \zeta(k). \quad (4.11)$$

Here, s is the spacer thickness, $C_J = \frac{J_1 - 2J_2}{dM_s}$ the bilinear (biquadratic) interlayer exchange field, $\mu_0 H_u$ the in-plane uniaxial anisotropy field and $\mu_0 H_s$ the out-of-plane uniaxial anisotropy field.

As clearly visible, $G(k)$ is introducing the nonreciprocity in the bilayer system. This is the only term changing sign as a function of wave number k . All other terms are positive for both wave-vector directions.

4.2. Nonreciprocity in Extended Thin Films

The derived dispersion relation was validated by micromagnetic simulations, using the GPU-accelerated code MuMax3 [127]. To calculate the spin-wave dispersion, a long magnetic bilayer stripe with the length $l = 20 \mu\text{m}$ and width $w = 80 \text{ nm}$ was considered. The system was discretized with $2048 \times 16 \times N_z$ cells. N_z was chosen according to the total thickness of the bilayer. The cell size c_z was kept constant with $c_z = 1 \text{ nm}$. To mimic the extended nature of a magnetic thin film, periodic boundary conditions were applied along the x - and z -directions, as depicted in Fig. 4.1. The magnetization dynamics were excited using the sinc-pulse form

$$\vec{h} = \tilde{h} \frac{\sin(k_0 z)}{k_0 z} \frac{\sin(2\pi f_0 t)}{2\pi f_0 t} \hat{y} \quad (4.12)$$

with the cut-off wavelength $\lambda_0 = 2\pi/k_0 = 9.77 \text{ nm}$, and a cut-off frequency of 50 GHz. To obtain the spin-wave dispersion relation, the magnetization configuration was stored every 10 ps for a total time of 12.5 ns and afterwards transformed using MuMax³-dispersion. The amplitude of the \tilde{h} was chosen to $\tilde{h} = 50 \text{ mT}$.

Two example systems were chosen to investigate the nonreciprocal spin-wave dispersion relation theoretically. The first system is composed of two identical NiFe layers with three different layer thicknesses $d = 2, 5$ and 20 nm . The spacer thickness was fixed to $s = 1 \text{ nm}$. The saturation magnetization M_s and the exchange stiffness $D = 2A/M_s$ were chosen to $M_s = 658 \text{ kA/m}$ and $D = 24.8 \text{ Tnm}^2$, respectively. The resulting spin-wave dispersion

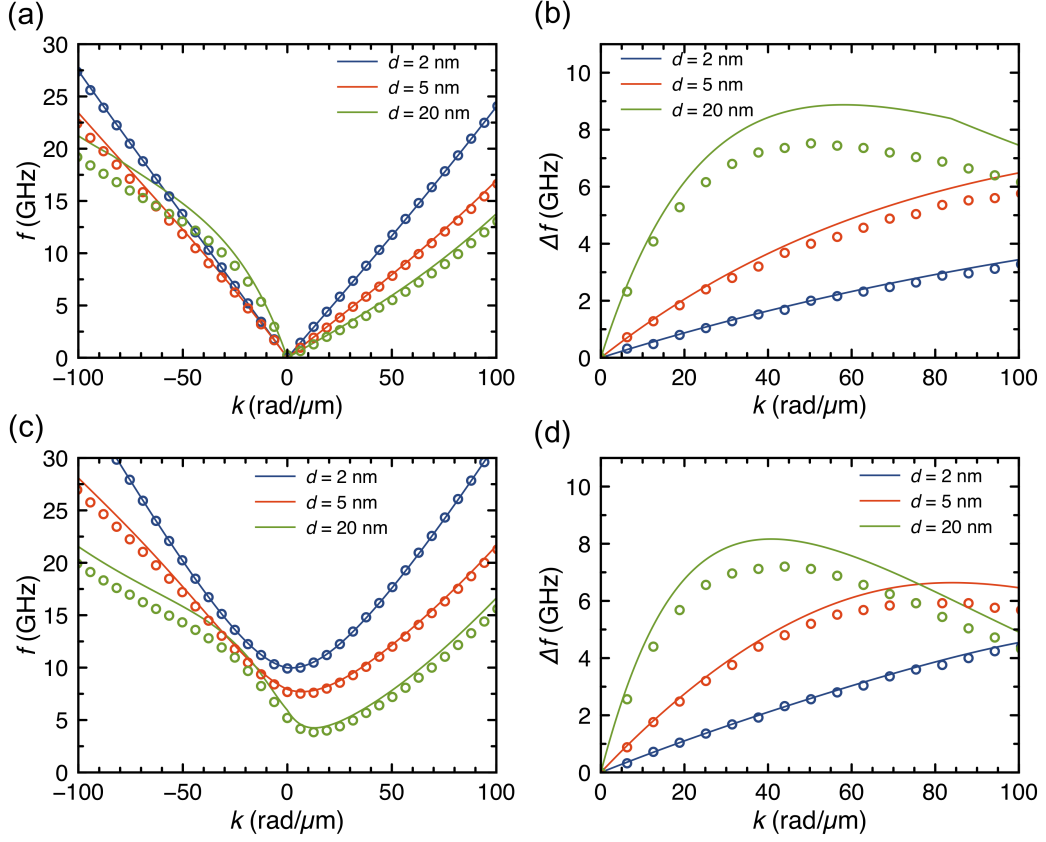


Figure 4.2.: (a,c) Nonreciprocal spin wave dispersion relation for the layer systems S_I and S_{II} , respectively. The open symbols represent the results of the micromagnetic simulations and the solid lines the analytic theory. (b,c) frequency shift Δf of two counter-propagating spin-waves as a function of the wave-vector k .

relations calculated with Eq. (4.7) in comparison to micromagnetic simulations are shown Fig. 4.2(a). In the limit of small thickness, the analytic theory and micromagnetic simulations agree perfectly. However, increasing the layer thickness results in slight deviations between both approaches.

Figure 4.2(b) depicts the frequency difference for two counter-propagating SWs. Already for 5 nm layer thickness, small deviations for large wave numbers are visible. These deviations increase with increasing layer thickness as visible for $d = 20$ nm. Since the analytic theory considers the amplitude of the dynamic magnetization to be constant along the thickness, this result is not surprising. For a very large layer thickness, the character of the magnetostatic surface modes has to be obtained, resulting in variations of the SW amplitude along the thickness. As one will see later in detail, the dipolar fields are responsible for the nonreciprocal spin-wave dispersion [16]. The thickness-dependent amplitude

of the dynamic magnetization will partially screen the magnetic charges in the volume and therefore, the nonreciprocity is reduced.

The second system considered was composed of one NiFe layer and one Co layer with the same thicknesses mentioned above. The material parameters of the NiFe layer were chosen identical to the material parameters of the first system. For the Co layer the saturation magnetization M_s and the exchange stiffness D were selected as $M_s = 1150$ kA/m and $D = 50.0$ Tnm², respectively. The eigenvalues of Eq. (4.5) for this case had to be calculated numerically. The resulting spin-wave dispersion is presented in Fig. 4.2(c). For this system, S_{II}, very small deviations are already observed for $k = 0$ for all investigated thicknesses. Since the effective field strongly differs in both layers, already the $k = 0$ modes show a profile of the dynamic magnetization along the film thickness. However, the deviation of the nonreciprocity in the case of system S_{II} is smaller [Fig. 4.2(d)]. Since the confinement of the SW modes to the surface depends on the wave number as well as the material parameters, this result is directly clear. The maximal nonreciprocity for $d = 20$ nm was calculated for $k \approx 35$ rad/ μ m instead of $k \approx 60$ rad/ μ m for system S_I.

The achieved magnitude of the nonreciprocity is almost a factor of five larger than the largest values reported for DMI systems [32, 33, 128] so far.

Moreover, the scaling of the dipolarly induced nonreciprocity is inverted compared to DMI. Approximating Eq. (4.7) for small wave numbers, and therefore considering the large wavelength limit yields

$$f(k \rightarrow 0) = f(0) - \frac{\gamma}{2\pi} d \mu_0 M_s \left(1 + \frac{\gamma}{2\pi} \frac{\mu_0 H_u}{f(0)} \right) k. \quad (4.13)$$

The similarity of the approximated spin-wave dispersion with the influence of DMI is remarkable [129]. In contrast to DMI, the frequency shift of two counter-propagating waves shows a different behavior. The frequency shift for the antiparallel state (AP) is given by

$$\Delta f_{\text{AP}} = \frac{\gamma}{2\pi} \mu_0 M_s k d \zeta(k)^2 e^{-|k|s}. \quad (4.14)$$

This expression can be approximated for small wave numbers, resulting in

$$\Delta f_{\text{AP}}(k \rightarrow 0) = \frac{\gamma}{\pi} \mu_0 M_s d k. \quad (4.15)$$

Therefore, the frequency shift will linearly increase with the film thickness d . This result is in strong contrast to the interfacial DMI induced nonreciprocity.

To understand the effect of the dipolar field qualitatively, the dynamic magnetization and the corresponding magnetic charges for antiparallel alignment are shown in Fig. 4.3. Both, volume and surface magnetic charges are considered. For SWs traveling along the positive

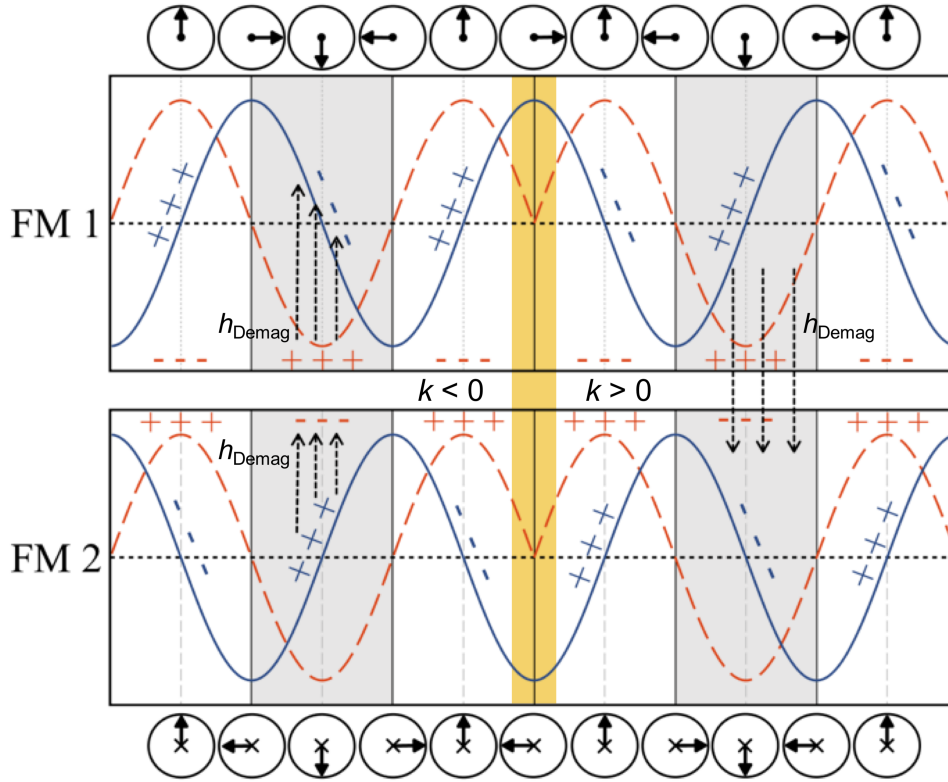


Figure 4.3.: Schematic representation of the magnetic volume and surface charges produced by the dynamic magnetization in a magnetic bilayer for the layer system S_1 . The dynamic magnetization of both FM layers is shown as indicated by the arrows. The blue curve represents the x -component and the red dashed curve the z -component of the dynamic magnetization projected onto the plane of the propagating SW. The magnetic charges produced by the dynamic magnetization in the volume proportional to $\nabla \cdot \vec{m}$ (blue) and the surface (red) are indicated with plus and minus signs. The resulting dynamic dipole field is indicated by the dashed arrows. Comparing both, positive k - and negative k -direction, a clear difference in the arrangement of the magnetic charges, and therefore the dynamic dipole field is visible.

z -direction, the volume charges start with positive values and oscillate, while moving along the z -direction. For the negative z -direction the signs of the volume charges are inverted, due to the fixed rotation sense of the dynamic magnetization. However, changing the alignment of the static magnetization from antiparallel to parallel, the rotation sense has to be inverted, resulting in a configuration of the volume charges as depicted in Fig. 4.3.

Additionally, the magnetic surface charges at the interface to the non-magnetic spacer have to be considered. Calculating $\vec{n} \cdot \vec{m}$, with the normal vector of the surface \vec{n} , for both layers, results in opposite charges at both interfaces to the ferromagnetic layers.

To now understand the different wavelengths for both counter-propagating waves, the dynamic dipole energy has to be analyzed. Evaluating the magnetic charges for a fixed

position in z for both $+z$ and $-z$ (grey shaded area), clearly shows a strong difference for both directions. For negative wave numbers the dynamic dipole field is antiparallel to the dynamic magnetization. Regarding positive wave numbers, the magnetic charge distribution is changed and therefore, a parallel configuration of the dynamic magnetization and the dipole field is achieved. Since the dipole energy is given by $\epsilon_{\text{Demag}} = -(1/2)(\vec{m} \cdot \vec{h}_{\text{Demag}})$, the counter-propagating waves have different energies. However, the frequency f is fixed, the spin wave therefore will adapt the wavelength for both directions to match the energy landscape.

So far the analytical calculations are only supported by micromagnetic simulations. However, supporting the theoretical framework with experimental results is beneficial. Therefore, two samples series were designed in collaboration with the group of Prof. Hellwig at the TU Chemnitz. All material and geometric parameters of the sample were carefully determined using multiple methods, like transmission electron microscopy (TEM), magnetometry and FMR. An overview of the samples is presented in Tab. 4.1. The first samples series consists of two synthetic antiferromagnets, containing $\text{Co}_{40}\text{Fe}_{40}\text{B}_{20}$ and $\text{Ni}_{81}\text{Fe}_{19}$. A thin Ir layer mediates the interlayer exchange coupling between both layers, to achieve an antiparallel alignment at remanence. Such systems were and still are strongly investigated regarding their static and dynamic properties [35, 130–132].

In the second sample series the antiparallel alignment of both layers is produced by the direct interface of the antiferromagnet IrMn with one of the $\text{Ni}_{81}\text{Fe}_{19}$ layers.

Magnetometry

The sample magnetization for the first samples series, $M(H)$, was determined using SQUID-VSM magnetometry, with a QuantumDesign Magnetic Properties Measurement System (MPMS)². The effective anisotropy constant (K_{eff}) was determined by acquiring in-plane

²The measurement was done by S. S. P. K. Arekapudi at the TU Chemnitz.

Table 4.1.: Overview of the thickness of the individual layers of all samples. For the sample Ch2724 the thicknesses were determined by TEM. The nominal thickness for the sample Ch2724 are provided in the squared brackets. For all other samples the nominal thicknesses are given.

Sample	Stack	d_{FM_1} [nm]	d_{FM_2} [nm]	s [nm]
Ch2724	$\text{Co}_{40}\text{Fe}_{40}\text{B}_{20} / \text{Ir} / \text{Ni}_{81}\text{Fe}_{19}$	5.7(2) [6]	6.7(3) [6]	0.6(3) [0.45]
Ch2717	$\text{Co}_{40}\text{Fe}_{40}\text{B}_{20} / \text{Ir} / \text{Ni}_{81}\text{Fe}_{19}$	10	10	0.45
Ch2745	$\text{IrMn} / \text{Ni}_{81}\text{Fe}_{19} / \text{Cu} / \text{Ni}_{81}\text{Fe}_{19}$	8	8	5
Ch2746	$\text{IrMn} / \text{Ni}_{81}\text{Fe}_{19} / \text{Cu} / \text{Ni}_{81}\text{Fe}_{19}$	10	10	5

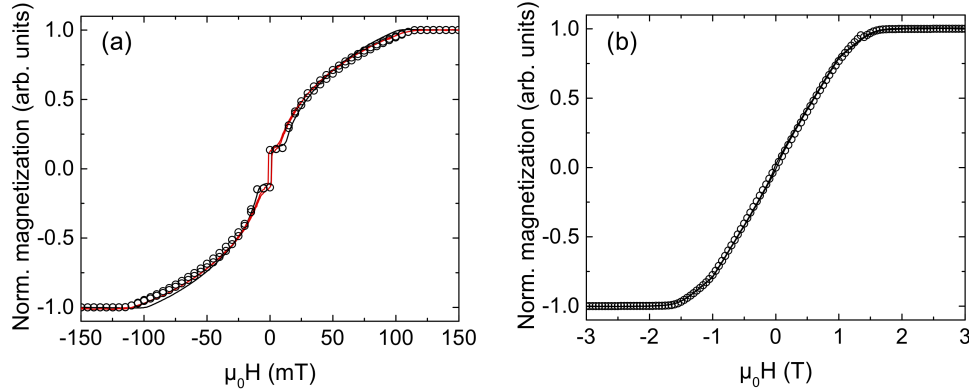


Figure 4.4.: Magnetometry measurements for the sample Ch2724 for (a) in-plane orientation and (b) out-of-plane orientation of the magnetic field. The black and red solid lines represent the experimental data for the SQUID-VSM and conventional VSM, respectively. The black open symbols represent micromagnetic simulations of the hysteresis loop.

($\theta_H = 90^\circ$) and out-of-plane ($\theta_H = 0^\circ$) hysteresis loops. The bilinear and biquadratic interlayer exchange coupling constants of the AF-coupled layers were obtained from the in-plane hysteresis loops. Additionally, conventional VSM measurements have been performed with a MicroSense VSM EZ7³. The results of the magnetometry measurements are presented in Fig. 4.4. Both field orientation $\theta_H = 90^\circ$ [Fig. 4.4(a)] and $\theta_H = 0^\circ$ [Fig. 4.4(b)] are shown. The black and red solid lines show the experimental results. To extract the material parameters, micromagnetic simulation have been performed, to reproduce the hysteresis loops. Since no domain formation is expected, only a small lateral system (16 x 16 cells) has to be considered. The individual thicknesses of each layer were modeled according to the realistic sample. To mimic the nature of an extended film, periodic boundary conditions (PBC) were applied within the film plane. At every field step the total energy and the torque were minimized using a steepest-descent solver.

The open black symbols show the results of the micromagnetic simulations. The curvature of the hysteresis loop for $\theta_H = 90^\circ$ suggests a rather strong contribution of the biquadratic coupling [133, 134]. Both magnetometry measurements provide different results, especially for the saturation field $\mu_0 H_s$ for the sample. It is important to note, that the saturation fields measured with both techniques differ by almost 10%. At first, this small difference seems to be negligible, but in coupled systems the saturation field is mainly given by the strength of the interlayer exchange coupling [135]. Therefore, this rather small difference leads to a wrong assumptions regarding the coupling strength, which subsequently will affect the evaluation of the dynamic magnetic properties. The saturation field $\mu_0 H_s$ in

³The measurement was done by A. Oelschlägel at the HZDR.

coupled identical magnetic bilayer is given by [135]:

$$\mu_0 H_s = -\frac{2}{M_s d} (2J_2 + J_1). \quad (4.16)$$

The saturation field determined by the SQUID-VSM is smaller than the field determined by the conventional VSM, leading to smaller bilinear (biquadratic) interlayer exchange coupling constants J_1 (J_2). The reason of the difference of the saturation field is still unknown.

Moreover, the VSM measurements do not show a perfect antiparallel alignment of both layers at small external magnetic fields. In contrast to this, the SQUID measurement does. However, also the in-plane SQUID loop has a small slope in the low field regime. This observed static behavior of the bilayer sample might indicate a non-perfect antiparallel alignment of both layers. This would consequently affect the spin-wave dispersion measurement presented later.

FMR Experiments

To extract the contribution of the exchange bias for the second series, FMR measurements have been performed. The in-plane angular dependence will provide valuable information about the direction of the exchange bias with respect to the easy-axis in the unbiased layer and the strength of the exchange bias field. As an example the in-plane angular dependence for the sample Ch2745 is shown in Fig. 4.5. Two modes can be detected over the full circle of in-plane angles. The clear crossing of these two modes at 90° and 275° indicates that both magnetic layers are uncoupled. The minimal resonance field (easy axis) at 180° denotes the exchange bias direction. To increase the visibility of the exchange bias in the experimental data, the measurement was performed at a frequency $f = 5$ GHz instead of the more commonly used values $f = 10$ GHz or $f = 15$ GHz. At the lower frequency the influence of the exchange bias on the resonance position is larger since the resonance fields are rather small compare to the exchange bias field. Therefore, the exchange bias field dominates the measured resonance field, leading to a clearer splitting of the two modes. Further reduction of the excitation frequency is not possible, since the resonance fields tend towards zero field.

The extracted material parameters using the resonance equation (2.55) for both exchange biased samples are listed in Tab. 4.2.

A detailed analysis of the interlayer exchange-coupled sample regarding the structural and magnetic parameters was performed. The magnetic parameters were extracted as the best fit of all performed measurement techniques, each with its own advantages and disadvantages.

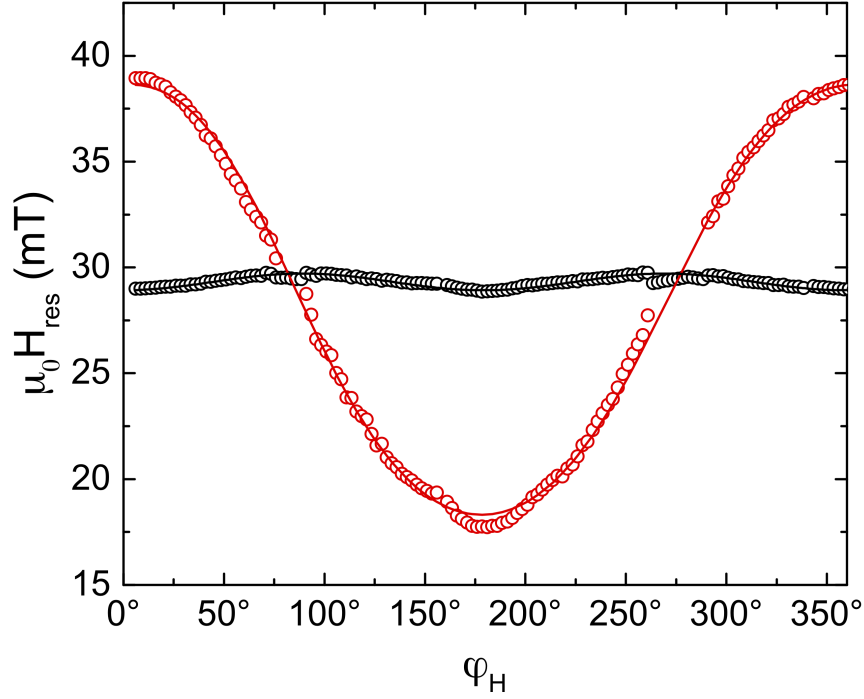


Figure 4.5.: In-plane angular dependence of the sample Ch2754. The excitation frequency was fixed to $f = 5$ GHz. The red and black open symbols represent the extracted resonance fields for both layers. The angular dependence of the red symbols is attributed to the exchange bias. The red and black solid lines are fits using Eq. (2.55) for the exchange bias energy system.

The coupling of the two magnetic layers leads to the presence of two eigenmodes of the system. Therefore, two FMR modes, the acoustic and the optical mode, can be detected.

Both modes strongly differ in intensity. The acoustic mode, consisting of the parallel alignment of the dynamic magnetizations, shows larger intensities in the aligned regime. In contrast to this, for the optical mode, defined by the antiparallel alignment of both dynamic magnetizations, only the difference signal will be detected using the VNA-FMR [136, 137].

Table 4.2.: Overview of magnetic parameters for selected samples.

Sample	$\mu_0 M_{\text{eff}_1}$ [mT]	$\mu_0 M_{\text{eff}_2}$ [mT]	$2K_{u_1}/M_s$ [mT]	$2K_{u_2}/M_s$ [mT]	K_{eb}/M_s [mT]
Ch2745	948	948	0.40	0.84	-9.9
Ch2746	993	970	0.20	0.30	10.3

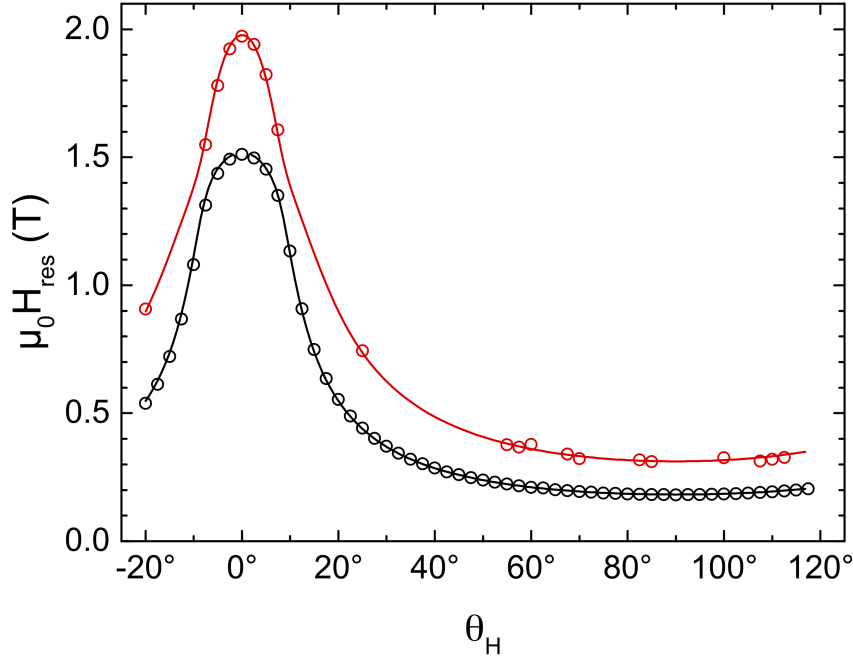


Figure 4.6.: Polar angular dependence of sample Ch2724. The red and black symbols correspond to the optical and acoustic mode, respectively. The solid lines show the fit based on the parameters presented in Tab. 4.3. The excitation frequency was fixed to $f = 10$ GHz.

The results of the FMR measurements are summarized in Figs. 4.6 and 4.7. Figure 4.6 depicts the polar angular dependence. Since the interlayer exchange coupling was optimized to favor antiparallel alignment, the optical mode is detected at higher resonance fields, and therefore lower energy. The red and black open symbols in Fig. 4.6 correspond to the optical mode and acoustic mode, respectively. However, as visible in both Figs. 4.6 and 4.7, the optical mode is difficult to measure, resulting in missing data points or additional scattering of the data. Nevertheless, already the polar angular dependence strongly indicates a coupling due to the avoided crossing of both modes around $\theta_H = 10^\circ$ and the large difference in the intensities of both modes.

For the frequency-field dependence (Fig. 4.7) two critical magnetic fields are visible. At those external field values the character of the FMR modes changes. The first transition around 15 mT is related to the spin-flop transition from the perfect antiparallel state to a canted state [131], as indicated in the magnetometry data. Interesting to note is the transition from an aligned mode back to a not-aligned mode present for the optical mode after the first critical field. At first the frequency as a function of the external of the optical starts increasing, reaching a maximal frequency around 75 mT. At this field values the frequency

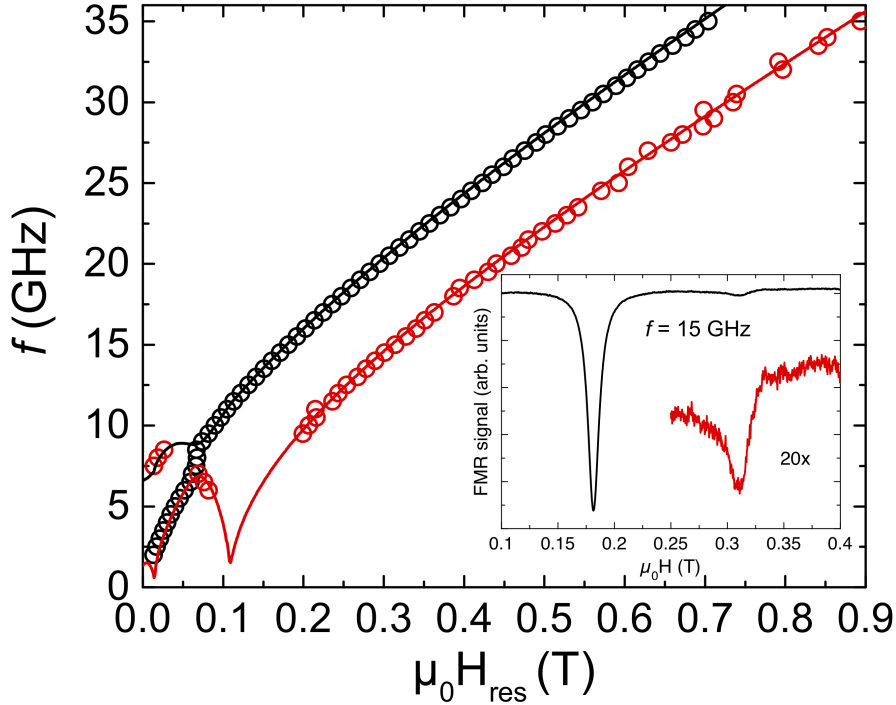


Figure 4.7.: Frequency-field dependence $f(H)$ of sample Ch2724. The red and black symbols correspond to the optical and acoustic mode, respectively. The solid lines show the fit based on the parameters presented in Tab. 4.3. Two critical fields are visible, where the FMR modes change their character. The inset shows an exemplary spectrum recorded at $f = 15$ GHz. The black solid line shows the complete spectrum with both, acoustic and optical mode. The red solid lines depicted the optical mode enlarged by a factor of 20.

starts decreasing again until reaching the saturation field. The sample is saturated around 100 mT, defining the second critical field or saturation field [131].

Without the not-aligned field range it is impossible to determine the ratio of the bilinear and biquadratic coupling using FMR. In the aligned field range, both coupling constants can be treated as an effective coupling of both layers [131]. The fitting of the not-aligned branches is challenging due to the larger linewidth and overlapping resonance peaks. In combination with the magnetometry measurements all material parameters were extracted, fitting the experimental data to the model using Eq. (2.57).

Now all magnetic and geometric parameters of the sample Ch2724 are determined. Only the exchange constant A_{ex} has to be fitted using the BLS results presented in the next section.

Brillouin Light Scattering Experiments

To investigate the spin-wave nonreciprocity, Brillouin light scattering (BLS) measurements were performed by the group of Prof. Anjan Barman⁴ in the Damon-Eshbach (DE) geometry [138,139]. A bias magnetic field was applied in the sample plane. The plane of incidence of the laser beam was set perpendicular to the applied field, probing SWs in the DE configuration. To investigate the spin-wave dispersion, a back-scattering geometry was used. The wave number was selected by changing the incidence angle θ of the monochromatic laser light (wavelength $\lambda = 532$ nm and power $P = 250$ mW) from a solid-state laser. To eliminate any phonon contributions to the measurement signal, the polarization of the incident laser beam and the scattered light were crossed. Subsequently, the frequencies of the scattered light are analyzed using a Sandercock-type six-pass tandem Fabry-Pérot interferometer from JRS scientific instruments [140]. Since the SW frequencies in the AFM region are very small, a free spectral range (FSR) of 30 GHz for higher wave numbers and 20 GHz for lower wave numbers was used, respectively. Additionally, a 2^{10} multi-channel analyzer was used during the BLS measurements, resulting in a frequency resolution of 0.05 GHz (0.02) for higher (lower) wave numbers.

The sample magnetization was first saturated by applying a high enough magnetic field of -140 mT (P state) followed by reducing the field slowly to the bias magnetic field $\mu_0 H = -5$ mT (AP state) and the BLS spectra were measured at both field values for multiple wave numbers. The SW dispersion was measured with a wave-number resolution of 2.06 rad/ μm up to a maximal wave number of $k = 20.4$ rad/ μm .

For the first few wave vectors, the Stokes and anti-Stokes peaks merge with the tail of the elastic peaks and could not be resolved and hence, only BLS spectra from $k = 8.1$ rad/ μm and higher are presented. The nonreciprocity in spin-wave frequency (Δf) was calculated by taking the difference between anti-Stokes and Stokes peak observed in the BLS spectra. All samples listed in Tab. 4.1 were investigated using BLS. However, only the sample Ch2724 provides reliable and useful results.

⁴Department of Condensed Matter Physics and Material Sciences, S. N. Bose National Centre for Basic Sciences, Block JD, Sec. III, Salt lake, Kolkata 700106 India

Table 4.3.: Experimentally determined material parameters for sample Ch2724. The magnetic properties were determined by FMR, SQUID and VSM. The layer thicknesses and the spacer thickness were determined by cross-section TEM.

	d (nm)	$\mu_0 M_{\text{eff}}$ (mT)	$\mu_0 H_u$ (mT)	J_{bl} (mJm ⁻²)	J_{bq} (mJm ⁻²)	s (nm)
Ni ₈₁ Fe ₁₉	6.7(3)	942.5	4.0	-0.195	-0.044	0.6
Co ₄₀ Fe ₄₀ B ₂₀	5.7(2)	1442.9	0.0			

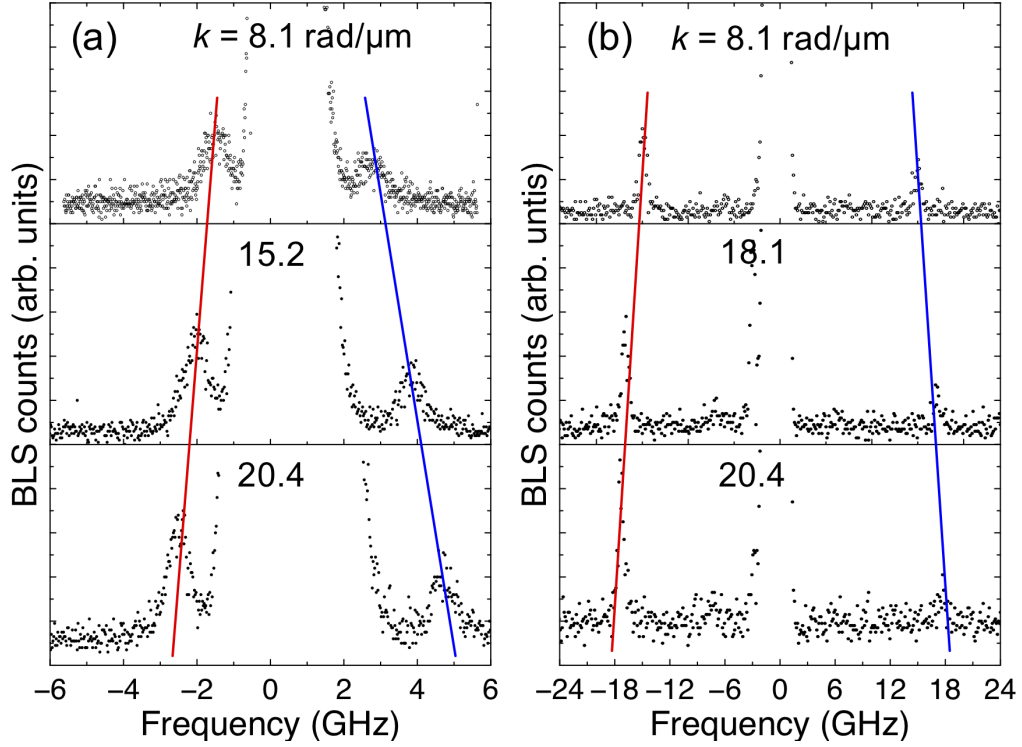


Figure 4.8.: BLS spectra for selected wave numbers for (a) the antiparallel and (b) the parallel state of sample Ch2724. The red and blue solid lines mark the trend of the peak. Already without detailed evaluation the nonreciprocity is clearly visible.

Exemplary BLS spectra for sample Ch2724 are shown in Fig. 4.8. The red and blue solid lines indicate the trend of the peak as a function of the wave number. For the SW frequencies observed in the AP state [Fig. 4.8(a)] the red and blue lines already indicate the nonreciprocity present in this system, as a different slope. Such a difference can be observed for the P state as well [Fig. 4.8(b)], but the frequency shift is significantly smaller. Nevertheless, the observed SW intensity is rather small, leading to a larger uncertainty in the SW frequencies.

The SW dispersion and the frequency shift are presented in Fig. 4.9. The open symbols in all panels represent the experimentally obtained SW frequencies and the resulting frequency shift. The solid lines are the theoretical calculation based on the approach shown above. Since almost all geometric and magnetic parameters were already determined by other measurement techniques, only the exchange constant A_{ex} had to be fitted for both measurements in the P and the AP state. The calculated SW dispersion for the P state [Fig. 4.9(b)] fits the experimental data set almost perfectly. Only small deviations are visible, especially in the frequency shift [Fig. 4.9(d)].

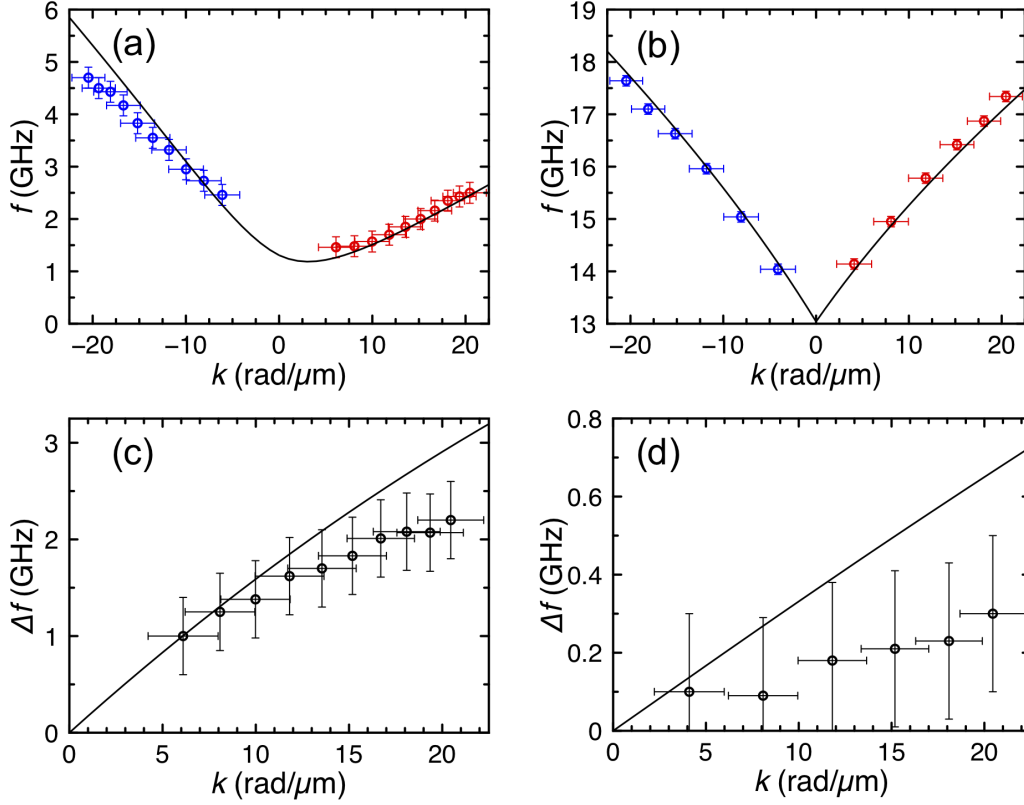


Figure 4.9.: Spin-wave dispersion and frequency shift for Stokes and Antistokes for the antiparallel (left panel) and the parallel state (right) panel. The blue and red open symbols represent the fitted BLS spectra as indicated in Fig. 4.8 by the red and blue solid lines. The black open symbols in (c) and (d) show the frequency shift for the AFM and FM state, respectively. All solid lines show the theoretical prediction.

Since the theoretical approach has 15 independent parameters, the uncertainties of all these parameter affect the resulting SW dispersion. The agreement in the AP state [Fig. 4.9(a)] is not as perfect as for the FM state, but still good. However, to obtain this almost perfect match, each layer had to be tilted 25° with respect to the y -axis. This leads to a reduction of the intermediate angle of both layers and is directly followed by a reduction of the nonreciprocity. However, already the VSM hysteresis loops indicated such a possible tilting. The biquadratic coupling can stabilize such a canted state. Nevertheless, the theoretically predicted frequency shift was almost confirmed. Our prototype system already reaches frequency shifts similar to the largest values reported in the presence of DMI [32]. However, the big advantage of the here proposed system is the scaling with the film thickness. With increasing film thickness, the nonreciprocity could easily be increased.

To investigate this increase of the nonreciprocity a second prototype system with very thick magnetic layers was investigated.

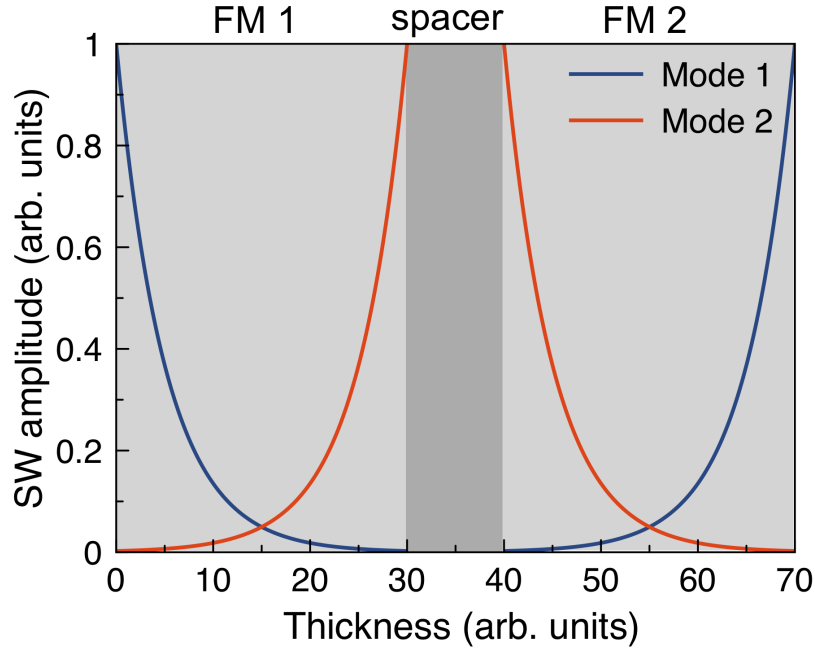


Figure 4.10.: Sketch of the dynamic magnetization profile along the thickness of a thick magnetic bilayer. Mode 1 shows a strong decay of the SW amplitude towards to spacer for the first layer (FM 1). The SW amplitude for mode 1 grows towards the second interface in the second layer (FM 2). Mode 2 shows the exactly opposite behavior.

4.3. Nonreciprocal Spin-Wave Emission in Stacked Vortex Pairs

As presented in the previous section, BLS can provide direct evidence for the spin-wave nonreciprocity in magnetic bilayers. However, this technique is not suitable for investigating thick magnetic layers. The penetration depth of the laser light is limited to several nanometers [141]. However, normally this depth is enough to collect all necessary information regarding the spin waves. For the here investigated system, the distribution of the dynamic magnetization has to be considered. Both spin-wave branches have the character of magnetostatic surface spin waves, which results in a confinement of the amplitude close to the surface if the specimen is thick enough. However, in the case of a magnetic bilayer, four interfaces have to be considered. Fig. 4.10 shows the profile of the dynamic magnetization for the prototype system. Therefore, time-resolved scanning transmission x-ray microscopy (TR-STXM) was used to investigate the spin-wave dispersion in thick magnetic bilayers [143]. Details regarding the experimental realization and sample preparation can be found in Refs. [16, 142]. Since the application of an external magnetic field in such a setup is technically challenging, the antiferromagnetic groundstate should be stable at zero field. To achieve this groundstate, the magnetic film was patterned into elliptical microstructures as described in Ref. [142]. Moreover, an external antenna was lithographically prepared

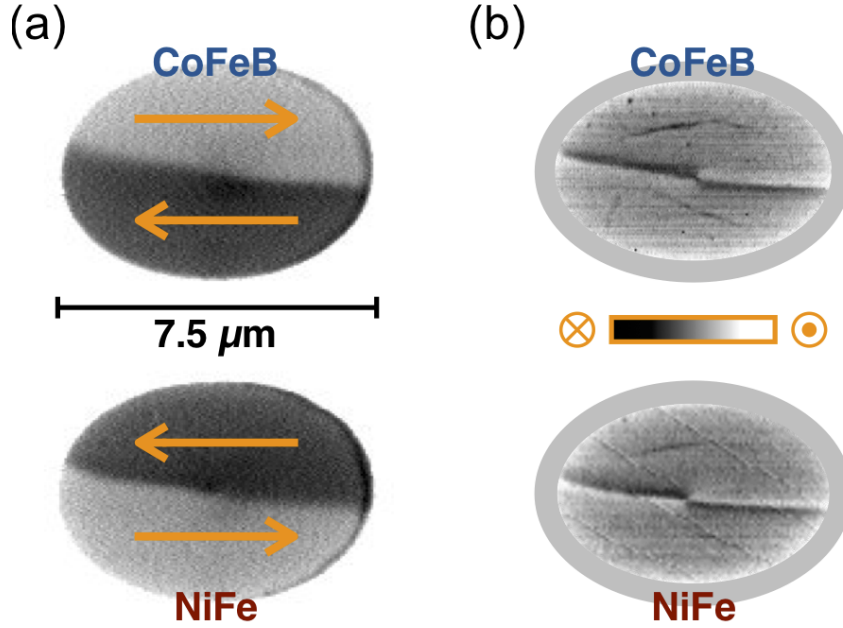


Figure 4.11.: STXM images of the magnetic configuration of the coupled bilayer. (a) shows the in-plane component of the magnetization and (b) the out-of-plane component clearly highlighting the 180° domain wall in the center [142]. The top row shows the CoFeB layer image obtained at the Co edge and the lower row for the NiFe layer recorded at the Ni edge.

on top of the microstructure, resulting in a homogeneous Oersted field in the area of the sample.

Due to the competition of the magnetostatic and the exchange field, a special magnetic texture is formed, referred to as magnetic vortex. The magnetic moments located at the rim of the microstructure are aligned parallel to it, resulting in a circulating magnetization and magnetic singularity in the center, termed vortex core. However, the here investigated system poses a peculiarity. Due to presence of a uniaxial anisotropy in both magnetic layers and the elliptical shape, a 180° domain wall is formed in the center of the structure, separating the magnetic texture in two parts. The resulting domain wall is present in both magnetic layers. However, since an antiferromagnetic alignment is favored, the vorticity, i. e. the rotation sense of the magnetization, is opposite. The domain wall itself can be considered as a mixture of a Bloch- and a Néel-like wall [144], showing partial perpendicular alignment. The STXM images of this complex ground state are depicted in Fig. 4.11. The black or white color indicates the local orientation of the magnetization of either the in-plane component [Fig. 4.11(a)] or the out-of-plane component [Fig. 4.11(b)]. The partial perpendicular alignment of the domain wall is not favored by the interlayer exchange interaction but the flux-closure state minimizes the magnetostatic energy.

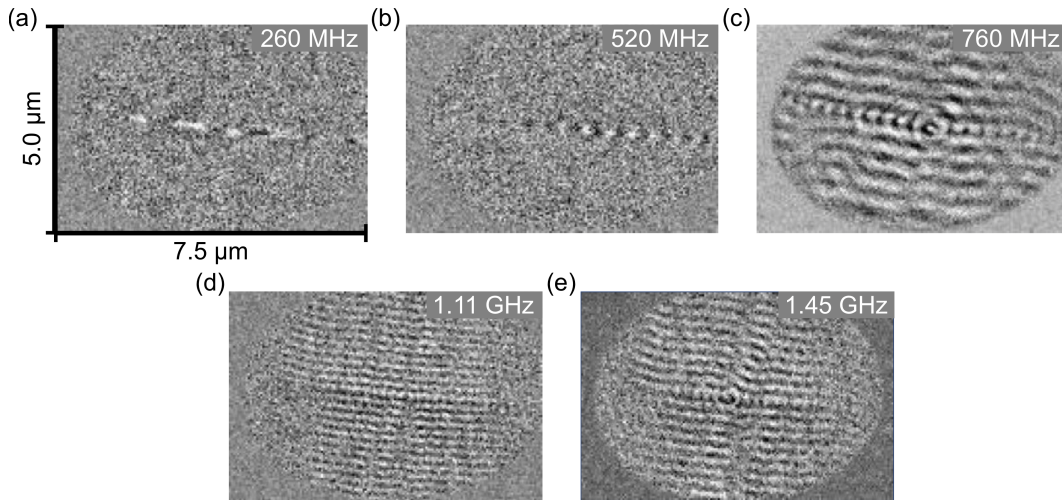


Figure 4.12.: TR-STXM image of the magnetic configuration of the coupled bilayer.

Spin waves can be excited in such magnetic textures by applying an alternating Oersted field [16, 145]. The antenna geometry utilized in this experiment results in strong in-plane Oersted field within the area of the sample. The antenna is oriented along the long edge of the ellipse, resulting in Oersted field components parallel to the short axis of the ellipse. Therefore, the Oersted field is oriented perpendicular to the domain wall. Since the Oersted field is homogenous within the sample area, only the domain wall and the vortex core can be excited by the rf-field. The concept of domain-wall mediated spin-wave emission was theoretically proposed in Ref. [146]. Moreover, first signatures were found in experiments [18]. The magnetization dynamics of the micro-structured bilayer was imaged stroboscopically by means of TR-STXM. This technique uses the time structure of the X-ray pulses produced in the synchrotron to image the excited dynamics. Details regarding this method can be found in Refs. [16, 142]. The resulting images for selected excitation frequencies are shown in Fig. 4.12. The black or white color represents the out-of-plane component of the magnetization.

For the smallest investigated frequency, $f = 260$ MHz, no spin waves can be detected within the domains themselves. Only confined excitations along a one-dimensional channel are visible. The static STXM images (Fig. 4.11) indicated the presence of the domain wall exactly at the position of the detected spin wave. Such a spin transport within a domain wall was already investigated theoretically [23] and later on confirmed by means of BLS [24]. Increasing the frequency ($f = 520$ MHz) clearly shows the expected reduction of the wavelength. However, the spin wave is still confined to the domain wall. At the excitation frequency $f = 760$ MHz, the first spin waves within the domain are detected. For this frequency three different types of spin waves are visible. At first, the spin wave within the domain wall is still present, as visible as an additional modulation along the domain wall.

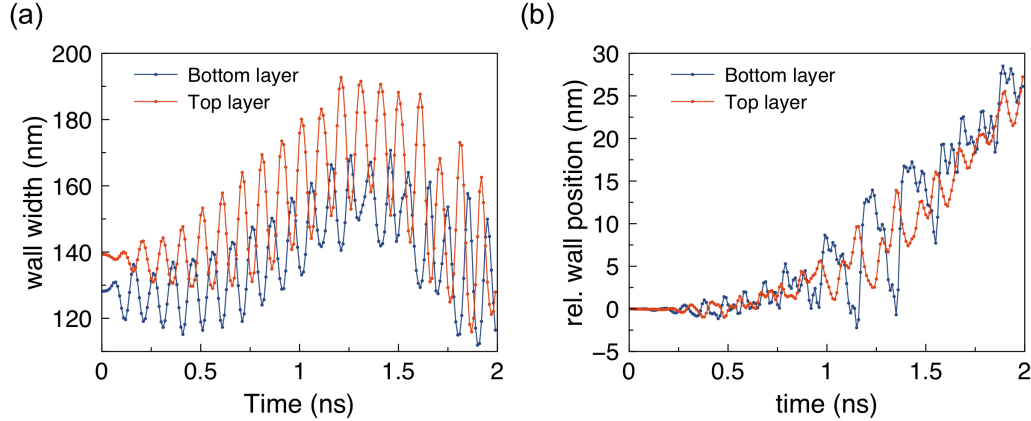


Figure 4.13.: Micromagnetic simulations of the excitation mode in coupled domain walls. (a) Domain wall width and (b) the relative wall position as a function of time excited with $f = 10$ GHz. The red and blue solid lines show the response in the NiFe and the CoFeB layers, respectively.

Moreover, radial spin wave modes were detected. Such an emission of radial spin waves within such magnetic textures had already been observed [16]. Due to the in-plane Oersted field, both vortex cores are excited, resulting in a small gyrotropic motion of these cores around their equilibrium positions. This gyrotropic motion leads to the formation of small magnetization "dips" of opposite sign [147]. This combined perturbation of the spin texture is followed by the emission of spin waves. An analogon can be easily found in a fluidic system. If a fluidic system is stirred orbitally, the resulting spiraling wave pattern is very similar.

Additionally, planar spin waves are excited in the investigated system. This type of spin waves are detected for all frequencies above $f = 760$ MHz. However, for all shown frequencies ($f \geq 760$ MHz) also radial spin waves are measured. For both $f = 1.11$ GHz and $f = 1.45$ GHz, the planar spin waves propagated further than the radial ones, since the damping in radial modes is inversely proportional to the traveling distance [16]. Therefore, the excitation of planar spin waves is superior with regard to the possible propagation distance.

To understand the process of the planar spin wave excitation in detail, micromagnetic simulations of this presented bilayer microstructure have been performed. Given the fact that both magnetic layers are rather thick (≈ 50 nm) and the spacer thickness is very small ($s = 0.8$ nm), the simulation of such a system is rather challenging. Already the discretization along the thickness requires 115 cells. Assuming a cell size within the plane of 5×5 nm², limits the system size to 3.24×2.16 μm^2 due to the maximal available memory on modern GPUs. The material parameters were chosen according to experimental and litera-

ture values. For the NiFe layer the saturation magnetization $M_s = 800$ kA/m, the exchange constant $A_{\text{ex}} = 10.5$ pJ/m and a small uniaxial in-plane anisotropy $\mu_0 H_k = 0.5$ mT were assumed. Regarding the CoFeB layer, the saturation magnetization $M_s = 1250$ kA/m, the exchange constant $A_{\text{ex}} = 13$ pJ/m [148] and a uniaxial in-plane anisotropy $\mu_0 H_k = 8$ mT were chosen. The anisotropy value in the CoFeB layer is significantly larger than values reported for individual layers [149]. This increase can be attributed to the strain present in the microstructured bilayer due to the antenna patterned on top of the system [150]. To stabilize the antiferromagnetic alignment, the interlayer-exchange coupling was chosen to be $J = -0.3$ mJ/m².

An in-plane sinusoidal excitation field along the short edge of the ellipse with a fixed frequency f was applied to excite the magnetization dynamics. In order to obtain a dynamic equilibrium the integration time was set to 20 periods. For each period the magnetization configuration was stored 10 times.

To study the excitation mechanism of the planar wave, the magnetization configuration for each layer was averaged along the thickness for all points in time. The contribution of the domain wall to the planar excitation was analyzed by extracting the domain wall profile across the short edge of the ellipse. The position and the width of the domain wall were extracted for both magnetic layers and are shown in Fig. 4.13. Within the first 0.25 ns only the wall width is periodically changing, indicating the excitation of spin waves due to the breathing of the domain walls [Fig. 4.13(a)] [151]. Important to note is that the breathing of both domain walls is phase-shifted by 180°. Since the interlayer exchange coupling favors antiparallel alignment, this optical mode is the energetically lower mode. Such breathing modes were reported as fundamental domain wall excitations [152]. With increasing time both domain walls start to move [Fig. 4.13(b)]. Only small periodic oscillations of the domain wall position are visible. For larger times a continuous shift of both domain walls is strongly pronounced. Since the simulated structure is rather small, the excited spin wave might be reflected at the border of the system and could interact with the domain wall, leading to a continuous shift of the latter. Additionally, also the width of the domain walls seems to be affected by the reflected spin waves.

To further deepen the understanding of the spin wave types present in this system, the spin-wave dispersion relation was experimentally determined and theoretically verified.

At first the planar waves within the domains are analyzed. By extracting the STXM signal along the propagation direction, the wave number $k = 2\pi/\lambda$ was extracted for all investigated frequencies. The result is represented by the open purple symbols in Fig. 4.14. The blue solid line shows the theoretical results, obtained by an extended framework discussed in Sec. 4.1. As mentioned before in this section, the theoretical description assumes a constant amplitude of the dynamic magnetization along the thickness. However, the framework

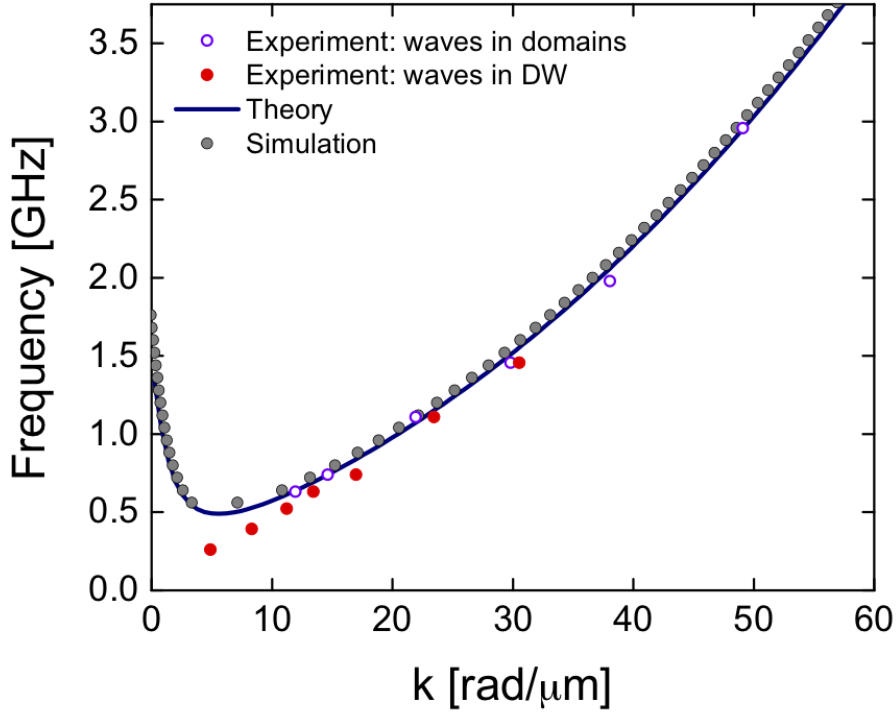


Figure 4.14.: Dispersion relation for the coupled Vortex pair [142].

was extended to include the splitting of each ferromagnetic layer into N equally thick thin films. These N slabs are coupled to each other by an effective ferromagnetic intralayer exchange coupling J_{intra} . This effective intralayer exchange coupling J_{intra} is determined by the continuum limit of the splitting, given by

$$J_{\text{intra}} = \frac{2A_{\text{ex}}}{a} \quad (4.17)$$

with the exchange constant A_{ex} and the slab thickness a . This theoretical description enables quick computing of the spin-wave dispersion relation in thick coupled ferromagnetic layers. Therefore, the eigenvalue problem [Eq. (4.5)] has to be solved. The size of the matrix \tilde{A} increases to $2N$. However, the solution of the eigenvalue problem is still considerably faster than full-scale micromagnetic simulations.

The calculated dispersion relation is sensitive on the CoFeB in-plane uniaxial anisotropy and the interlayer exchange coupling. For $J = -0.1 \text{ mJ/m}^2$ and $\mu_0 H_k(\text{CoFeB}) = 4.8 \text{ mT}$, a very good agreement of the theoretical calculation with the experimental data was found. Moreover, the exchange constant $A_{\text{ex}} = 7.5 \text{ pJ/m}$ [153] was slightly reduced compared to

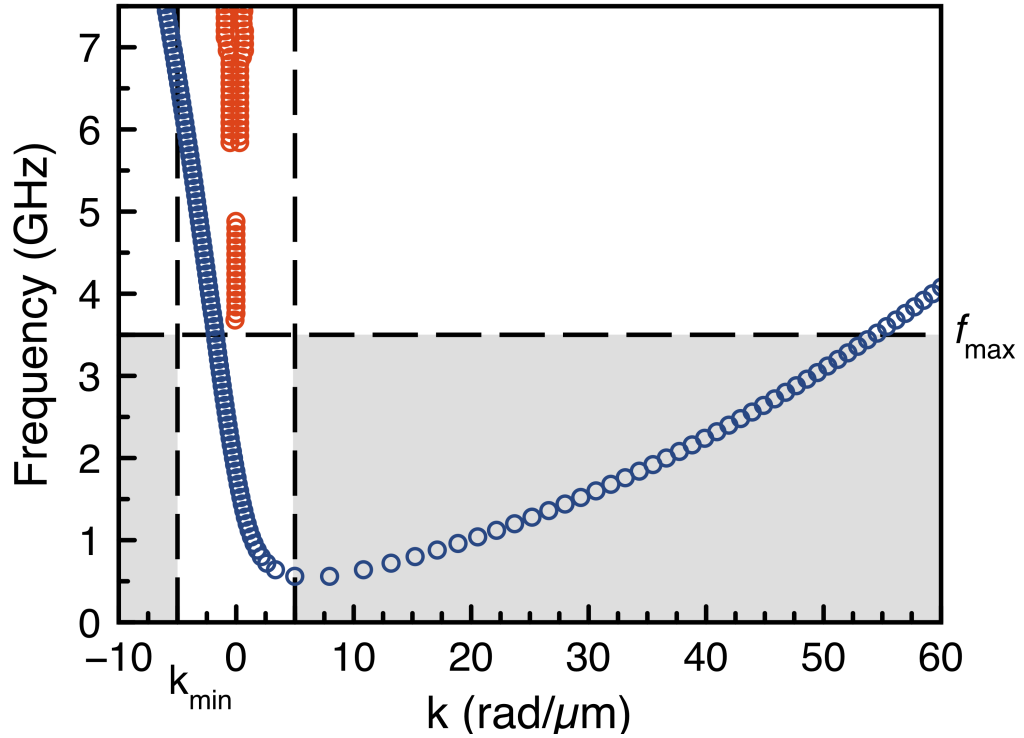


Figure 4.15.: Calculated dispersion relation of the coupled vortex pair. The open blue and red symbols correspond to the optical and acoustic mode of the magnetic bilayer, respectively. The grey shaded areas were experimentally accessible utilizing TR-STXM. The small wave number is given by the sample size. The highest frequency is determined by the time structure of the synchrotron.

the simulation of the excitation mechanism. All other material parameters were chosen as mentioned above. To validate the splitting approach micromagnetic simulations were performed. The results are shown as the solid grey symbols in Fig. 4.14. Both, micromagnetic simulations and theory agree very well, showing the suitability of the splitting approach.

As already observed in Fig. 4.2, the spin-wave dispersion shows a frequency gap in the presence of uniaxial anisotropy, leading to the formation of a local minimum in the dispersion. This intriguing feature is introduced by the combination of the dipole-induced nonreciprocity in antiferromagnetically coupled bilayers [16] with the uniaxial anisotropy. Again, similarities with the frequency shift induced by DMI can be found [129]. The experimental observation of the selective spin-wave propagation can be explained by the presence of the frequency gap. When selecting a frequency inside this gap no magnon propagation is allowed. Important to note is that only spin waves with positive wave numbers could be detected. Both, the very large group velocity of the fast branch and the system size limits the direct investigation of the nonreciprocity. Since the short axis of the ellipse is $2.5 \mu\text{m}$, the

small wave number is limited to $k_{\min} \approx 5 \text{ rad}/\mu\text{m}$. The high excitation frequency $f_{\max} = 3.5 \text{ GHz}$ is given by the time structure of the X-ray pulse produced at the synchrotron. As visible in Fig. 4.15, no spin wave with negative wave number can be excited.

In contrast to the planar wave, the measured dispersion relation in the domain walls linearly tends towards zero frequency. Therefore, no frequency gap is observed for this type of excitation. The existence or absence of gap-less excitation modes is usually explained by the Goldstone theorem [154]. This theorem postulates the existence of a gap-less mode, if the continuous symmetry of the system is spontaneously broken in the ground state. Specifically in the system under investigation, the continuous symmetry within the domains is broken by the uniaxial anisotropy, and therefore the frequency gap for this excitations is observed. For the spin wave confined to the domain wall, the continuous translational symmetry along the domain wall is preserved, leading to the presence of the gap-less mode. However, in realistic samples defects and the finite length will always introduce a small frequency gap, which seems to be too small to be observed within the scope of this study.

Conclusion

In conclusion, the theoretically predicted nonreciprocity in antiferromagnetically aligned bilayers could be directly and indirectly confirmed by means of BLS and TR-STXM. Since the frequency shift will increase with increasing film thickness, BLS measurements are limited in observing a very large nonreciprocity. For very thick magnetic layers, TR-STXM provides a suitable alternative. However, by using this technique only one branch of the spin-wave dispersion can be observed, providing only indirect evidence for the nonreciprocity in such systems. Nevertheless, using TR-STXM the striking feature of frequency-selective spin wave propagation in either ferromagnetic domains or the domain walls was experimentally observed for the first time. Both features, the nonreciprocity and the selective propagation provide new possibilities for magnon-based computing and magnonic circuits.

5. Numerical Investigation of Spin Superfluid Transport in Quasi-U(1) Systems

Many studies investigating superfluidic transport only rely on analytic theory. To the knowledge of the author only two single micromagnetic simulations including all important interactions have been reported [43, 44]. However, especially the excitation and therefore, the feedback of the injector on the magnetic state and vice versa, is of big interest regarding the experimental investigation of this long-distant spin transport. Moreover, multiple publications already explored an application of the spin superfluidity, e. g. , domain walls acting as hosts of these states or the transportation of domain walls using spin superfluids [155, 156]. Moreover, first experimental signatures of spin superfluidic transport were found in YIG [78], Chromia [157] and Graphene [158]. In this thesis, the spin superfluid transport is numerically investigated, exciting the dynamics using spatially localized spin-transfer torque. This injection region plays a crucial role defining the transport properties of the system. Both, an easy-plane ferromagnetic without non-local dipole-dipole interactions and a thin film including dipole-dipole interaction between the spins, are subject of the study. The latter shows not a perfect U(1) symmetry as discussed in Chapter 2.3, since, as one will see later, dipole-dipole interactions introduced a quasi anisotropy in the system. In the light of the currently available theoretical description of the spin superfluidic transport, two main questions can be formulated:

1. Is the superfluidic transport subject to a self-stabilizing mechanism at high bias current?
2. Does the superfluidic transport exist on large length-scales in the presence of non-local dipole-dipole interactions?

5.1. Thin Films with Dipole-Dipole Interaction

To understand the non-local dipole-dipole interactions and its impact on the superfluidic transport, a model system was studied. The material parameters were chosen to correspond

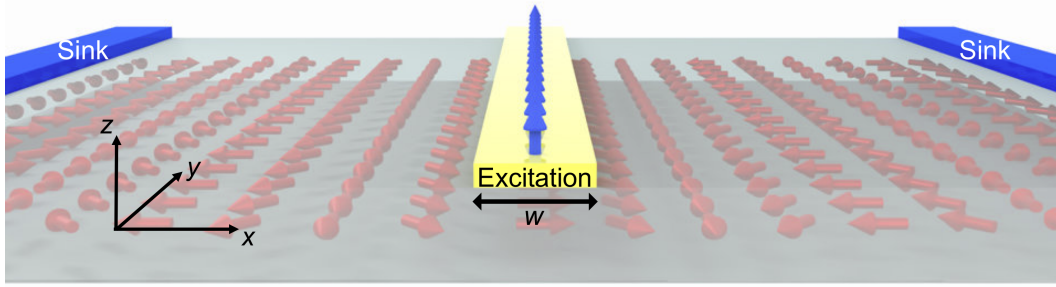


Figure 5.1.: Sketch of the theoretically investigated system. The yellow line indicates the DC injection channel with out-of-plane spin polarization (blue arrows). The blue areas correspond to the spin sinks to absorb the angular momentum. The red arrows indicate the 2π rotations of the magnetization [162].

to thin $\text{Y}_3\text{Fe}_5\text{O}_{12}$ (YIG) films. The saturation magnetization $M_s = 130 \text{ kAm}^{-1}$ and the exchange constant $A_{\text{ex}} = 3.5 \text{ pJm}^{-1}$ were chosen according to Refs. [159–161]. The lateral size of the system was chosen with a length $l = 50 \text{ }\mu\text{m}$ and a width $w = 5 \text{ }\mu\text{m}$. Since the dipole-dipole interactions should scale with the thickness of the system, a thickness from $d = 2 \text{ nm}$ up to $d = 30 \text{ nm}$ with a step size of 1 nm were simulated. To mimic the extended nature of the thin film, PBC were applied along the in-plane directions. Since the system is not a square, additional tests using a square-sized system ($50 \text{ }\mu\text{m} \times 50 \text{ }\mu\text{m}$) were conducted to test and verify the magnetostatic field. In contrast to the analytic model, the micromagnetic simulation have to assume a non-zero Gilbert damping parameter with $\alpha = 0.002$ to obtain a stable numerical solution. A sketch of the system showing the spin spiral is depicted in Fig. 5.1. It is important to note that in contrast to the previous chapter the x direction is now the propagation direction.

As already discussed in Chapter 2.3, the presented analytic approach does not cover the excitation. However, in the micromagnetic simulations the superfluid transport was excited by means of spin-transfer torque (STT). The SST with a spin polarization $\vec{p} = (0, 0, 1)$, was applied locally in the center of the system. Additionally, a spin sink, like an interface to a heavy metal, was introduced in the simulation to extract the spin current. This sink was modeled as an exponentially increasing Gilbert damping constant α at the short edges of the system. To investigate the zero-thickness limit, the dipole-dipole interactions were disabled. Instead an easy-plane anisotropy was introduced by using a negative uniaxial out-of-plane anisotropy $K_u = -10000 \text{ Jm}^{-3}$. This value roughly provides the same anisotropy field $H_K = \frac{2K_u}{M_s}$ as the magnetostatic field $\mu_0 M_s$. It was shown, that this replacement resembles the zero-thickness limit perfectly [163]. As discussed in Chapter 2.3, the gradient of the in-plane angle φ is directly proportional to the spin current. To extract this quantity, the

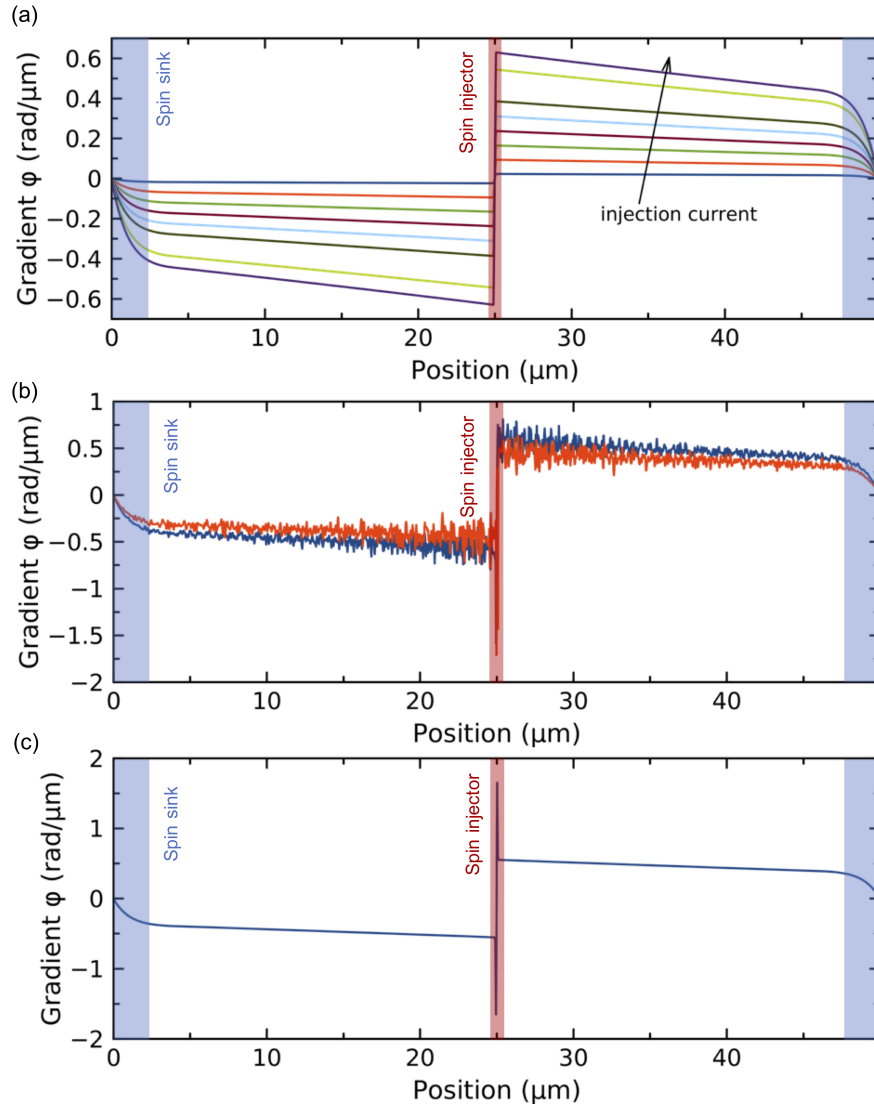


Figure 5.2.: Gradient of the in-plane angle φ as a function of the distance from the injector for selected current densities in the area of $1.0 \times 10^{10} \text{ A/m}^3$ to $4.6 \times 10^{11} \text{ A/m}^3$. The three panels are representative for the three observed regimes of the superfluidic transport. In (a) $\nabla\varphi$ shows a linear dependence with the distance for all current density values. Within the oscillatory regime, shown in (b) the linear dependence is superimposed with non-coherent oscillations along the channel. (c) with further increase of the injector current density, the linear dependence is recovered with an additional spin texture in the injector region. $\varphi = 0^\circ$ is defined by the equilibrium configuration $\vec{M} = M_s \hat{x}$.

magnetization dynamics is excited and the equation of motion is integrated over 500 ns to reach the dynamic equilibrium for each current density.

In Fig. 5.2 the gradient of the in-plane angle $\nabla\varphi$ as a function of the distance is shown for various injection currents. The Fig. 5.2(a) shows $\nabla\varphi$ as a function of the distance for the

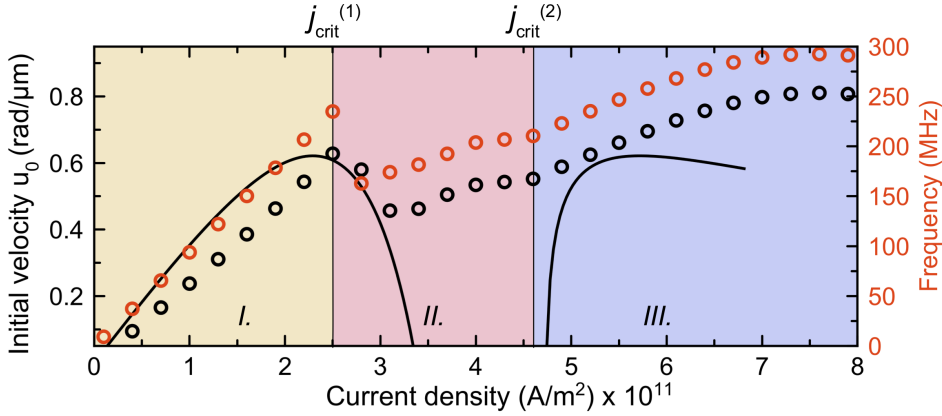


Figure 5.3.: Initial fluid velocity u_0 (black open symbols) and frequency Ω (red open symbols) of the superfluid state as a function of the injector current density omitting dipole-dipole interactions. The black solid line represent the analytically calculated transmitted spin current $u \sin^2 \theta$ for the spin superfluid. The three different regimes are marked with different color (yellow, red and blue).

linear regime ($1 \times 10^{10} - 2.5 \times 10^{11}$ A/m³). For every current density in this regime a linear response of the superfluid is observed. However, for the two largest current densities already a stronger increase in $\nabla\phi$ is visible in Fig. 5.2(a). This observed regime corresponds to the traditional spin superfluid solution, investigated by many studies [38, 40, 81]. The state provides the possibility for long-range spin transport. The gradient of the in-plane angle $\nabla\phi$ is linearly reduced only by a factor of two, when comparing values close to the injector and to the sink. Since the spin current is directly proportional to this quantity, the same reduction applies for it. In comparison to this, SWs would show an exponential damping. In the vicinity of the spin sink, the spin current quickly goes to zero due to the largely increased damping at the edges of the simulated system. The application of the spin superfluidic transport would be beneficial for various applications, since the spin current can be transported over very large length-scales. This regime is also obtained in the analytically model for the spin superfluid state using linear response theory. However, increasing the bias current density further, results in a breakdown of the initial fluid velocity $u_x = -\nabla\phi(x)$.

In Fig. 5.2(b) the fluid velocity is clearly reduced compared to the largest current density shown in Fig. 5.2(a). After this first critical current density $j_{\text{crit}}^{(1)}$ (blue line in Fig. 5.2(b)), the system undergoes a transition. As shown in Fig. 5.2(b) the linear superfluid is superimposed with additional spatial oscillations along the channel width. These oscillations are visible in all components of the magnetization vector. The injection mechanism can be considered as incoherent parametric magnon excitation within the region of the injector using spin-transfer torque. The injector region itself will autooscillate as a result of the parametric excitation. These autooscillations can be observed in Fig. 5.2(b) as an antisymmetric

distribution of $\nabla\varphi$ in the active region. However, the excited magnons are unstable, and therefore will rapidly disperse into incoherent magnons, propagating in the spin texture of the superfluid [164]. This superposition of spin waves (or magnons) with a collective state of magnons (the superfluid) shares large similarities with the two-fluid theory of superfluid Helium. The magnons in the system can be considered as the normal fluid in the system. Despite the fact that magnons are quasi-particles, still a BEC can be formed. Therefore, the magnon number in the system has to be conserved within a time scale accessible for experimental techniques. The time scale directly depends on the spin-lattice relaxation time. For YIG the spin-lattice relaxation time was reported to be about $1 \mu\text{s}$.

If we now consider the superfluid as a collective magnon state closely related to a magnon BEC, the two-fluid model for magnons can be explained as follows: While exciting a large number of incoherent magnons, the number of magnons in the collective state is reduced. Therefore, the fluid velocity u has to decrease.

If the bias current density is even further increased, the system will undergo the next transition. If the current density is larger than the second critical current density $j_{\text{crit}}^{(2)}$ the magnetization in the injection region is almost parallel to the injected spin polarization. The injected amount of angular momentum is too large for the active region to autooscillate. This is visible in Fig. 5.2(c). The gradient of the in-plane angle again depends linearly on the distance from the active region. In contrast to this, a stable spin texture is introduced in the active region.

The main results of all three regimes are summarized in Fig. 5.3. The gradient of the in-plane angle was extracted close to the active region, which is considered the initial fluid velocity $u_0 = -\nabla\varphi(0)$. As already discussed within the linear regime *I*, this quantity depends linearly on the injected current density. After reaching the first critical current density $j_{\text{crit}}^{(1)} = 2.5 \times 10^{11} \text{ A/m}^3$, the initial fluid velocity u_0 is reduced. The initial fluid velocity u_0 still depends linearly on the current density. However, the evaluation of the initial fluid velocity u_0 is complicated for this current range. The values in Fig. 5.3 correspond to the mean values of the oscillatory gradient at a given current density.

Therefore, minimizing the influence of the excited incoherent magnons on the data evaluation, and therefore, the oscillations visible in Fig. 5.2(b), a cell-dependent fast-Fourier transformation of the system was performed for all simulated current densities.

The resulting frequencies Ω are shown as the open red symbols in Fig. 5.3. Both quantities show very similar behavior. Only for the regime *II*, small deviations are visible between both. As already discussed above, u_0 is influenced by the additional magnons present in the system. The calculated frequency Ω of the spin superfluid depends linearly on the injector current density for both regimes *I* and *II*. The slope of the frequency is quite different for both regimes. The reduction of the frequency might be directly related to the reduction of

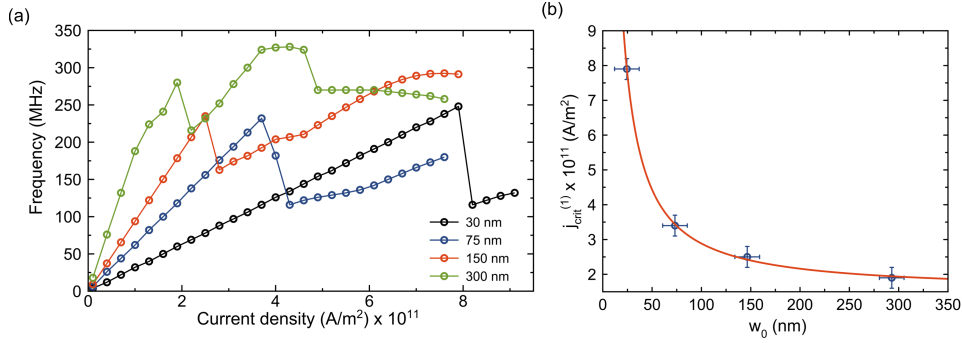


Figure 5.4.: Dependence of the spin superfluid on the injector width. (a) shows the calculated frequency Ω for four different injector widths. In (b) the extracted critical current density is plotted as a function of the injector width. The red line is a guide to the eye.

magnons in the collective state. Additionally, the difference in the slope might be a result of a large time-averaged m_z within the active region.

A similar effect is more pronounced for regime *III.*. At first the slope of the initial velocity and that frequency are similar to the one in regime *II.*, but with increasing bias current density both u_0 and Ω saturate. Since the static alignment of the magnetization in the active region is almost parallel to the spin polarization of the spin current for sufficiently large bias current densities, the superfluid is *screened*.

Since the observed behavior should strongly depend on the amount of injected spin current, different injector widths w were simulated. In Fig. 5.4(a) the frequency Ω is shown as a function of the bias current density for four different injector widths. For all four widths, the oscillatory breakdown is observed. The first critical current density j_{crit}^1 clearly depends on the injector width. For the nominally 300 nm wide active region the breakdown already occurs around $j_{\text{crit}}^{(1)} = 2 \times 10^{11}$ A/m². In comparison to this, reducing the injector width to nominally 30 nm, which corresponds to 1 cell in the simulations, increases the first critical current density to $j_{\text{crit}}^{(1)} = 8 \times 10^{11}$ A/m². Due to limitations in compute time and storage space the third regime could not be simulated for the small width of 30 nm. However, the results still clearly indicate that the amount of spin current injected modifies the breakdown current density. In Fig. 5.4(b) the first critical current density $j_{\text{crit}}^{(1)}$ is depicted as a function of the injector width. For this, the nominal width w of the injector was renormalized to the exact width given by the cell size of the simulation

$$w_0 = c_x \cdot \text{int} \left(\frac{w}{c_x} \right). \quad (5.1)$$

Here, w is the nominal width of the injector and c_x the cell size along the x-direction. Only the integer part of the fraction is considered for the calculation of the renormalized width w_0 . The red solid line in Fig. 5.4 is a fit using the function $\frac{A}{w_0} + B$, with the injector

width w_0 . A , B , p were treated as fitting parameters. The obtained fit parameters are listed in Tab. 5.1. Since the amount of spin current provided to the system linearly increases with the width w , a linear scaling was expected. However, scaling is proportional to x^{-1} within the uncertainties of the fit. Therefore, the critical current should be constant for sufficiently large injectors and converge to the value B extracted from the fit. To deepen the understanding of this scaling behavior additional studies of the detailed mechanisms of the breakdown have to be performed.

Together with the group of Prof. Tserkovnyak, and mainly driven by D. Hill¹, an analytic theoretical description of the observed effects was developed. As a starting point the equations of motion for non-linear spin superfluid transport were used [42]. The same coordinate system as depicted in Fig. 5.1 was employed.

$$\dot{\theta} - \alpha \dot{\varphi} \sin \theta = - \frac{\partial_x (\partial_x \varphi \sin^2 \theta)}{\sin \theta} \quad (5.2)$$

and

$$\dot{\varphi} \sin \theta + \alpha \dot{\theta} = \partial_x^2 \theta + \frac{1 - (\partial_x \varphi)^2}{2} \sin 2\theta. \quad (5.3)$$

Additionally, the following boundary conditions were applied

$$(\mp \partial_x \varphi + g \dot{\varphi} - j) \sin \theta = 0, \quad (5.4)$$

$$\partial_x \theta \mp g \dot{\theta} = 0. \quad (5.5)$$

Here, θ and φ describe the out-of-plane and the in-plane angle of the magnetization, respectively. The boundary conditions are determined by the dimensionless spin-mixing conductance $g = \frac{1}{s} \sqrt{\frac{K_u}{M_s}} \left(\frac{\hbar}{4\pi} \right)$ and the applied dimensionless spin current density j . To simplify matters, the Gilbert damping constant α is assumed to be zero. Moreover, we assume $\dot{\varphi} = \Omega$ and $\dot{\theta} = 0$. The fluid velocity is defined as always: $u(x) = -\partial_x \varphi$. Then, the equations of motion become

$$\partial_x (u \sin^2 \theta) = 0, \quad (5.6)$$

$$\Omega \sin \theta = \partial_x^2 \theta + (1 - u^2) \sin \theta \cos \theta. \quad (5.7)$$

¹Department of Physics and Astronomy, University of California, Los Angeles, California 90095, USA

Table 5.1.: Extracted parameters for the first critical current $j_{\text{crit}}^{(1)}$ as a function of the injector width w .

A	B	p
210.40 ± 59.04	1.52 ± 0.18	1.09 ± 0.09

Eq. (5.6) easily can be solved by integrating:

$$u = c_1 \csc^2 \theta. \quad (5.8)$$

It is important to note that c_1 is an integral. Substituting Eq. (5.8) in Eq. (5.7) and multiplying the equation with $\partial_x \theta$ yields

$$\Omega \cos \theta + \frac{1}{2} (\partial_x \theta)^2 + \frac{1}{2} \sin^2 \theta + \frac{c_1^2}{2} \csc^2 \theta = c_2. \quad (5.9)$$

The solution now should satisfy the new boundary conditions at $x = 0$

$$v(0) = j - g\Omega, \quad (5.10)$$

$$\partial_x \theta(0) = 0 \quad (5.11)$$

and for $x \rightarrow \infty$

$$u(\infty) = -j_\infty - g\Omega, \quad (5.12)$$

$$\partial_x \theta(\infty) = 0. \quad (5.13)$$

In general, the solution for non-constant θ can be obtained from Eq. (5.9), solving for x

$$x - x_0 = \frac{1}{\sqrt{2}} \int_{\theta_0}^{\theta(x)} \frac{d\theta}{\sqrt{c_2 - \Omega \cos \theta - \frac{1}{2} \sin^2 \theta + \frac{c_1^2}{2} \csc^2 \theta}}. \quad (5.14)$$

Considering the steady-state spin superfluid, the transition from an arbitrary θ_1 to θ_2 over a finite region, resembles a domain wall, as the superfluid state consists of 2π windings. The points θ_1 and θ_2 can be obtained from Eq. (5.9) with the condition $\partial_x \theta = 0$. The characteristic equation reads

$$\Omega \cos \theta_i + \frac{1}{2} \sin^2 \theta_i + \frac{c_1^2}{2} \csc^2 \theta_i = c_2, \quad (5.15)$$

with $i = 1, 2$.

To obtain the general solution, the boundary conditions have to be applied properly. At first we start with Eq. (5.7), which results in

$$u(x) = \frac{(j - g\Omega) \sin^2 \theta_1}{\sin^2 \theta(x)} \quad (5.16)$$

and

$$\frac{\sin^2 \theta_1}{\sin^2 \theta_2} = -\frac{j_\infty - g\Omega}{j - g\Omega} \geq 0. \quad (5.17)$$

Beyond the transition region, the solution represents a dissipationless spin superfluid, and from Eq. (5.7) this state must satisfy $\Omega = (1 - u^2) \cos \theta$. By applying the boundary condition at $x = \infty$ to the equation, one finds

$$\Omega = \left[1 - (j_\infty - g\Omega)^2 \right] \cos \theta_2. \quad (5.18)$$

Finally, one can apply the boundary conditions to Eq. (5.9)

$$\Omega \cos \theta_1 + \frac{1}{2} \left[1 + (j - g\Omega)^2 \right] \sin^2 \theta_1 = \Omega \cos \theta_2 + \frac{1}{2} \left[1 + (j_\infty - g\Omega)^2 \right] \sin^2 \theta_2. \quad (5.19)$$

The Eqs. (5.17), (5.18) and (5.19) give us three coupled equations for the three unknowns θ_1 , θ_2 , and Ω as a function of the external parameters j , j_∞ , and g .

The general solution of the set of coupled equations has to be obtained numerically. However, the limit of large bias, $j \rightarrow \infty$, for the case of $j_\infty = 0$ results in an asymptotic behavior

$$\Omega \propto 1/j \sin \theta_1 \propto 1/j \sin \theta_2 \propto 1 + O(1/j). \quad (5.20)$$

Therefore, the spin current carried by the spin superfluid is

$$j_s = u \sin^2 \theta_2 \propto \frac{1}{j}. \quad (5.21)$$

The resulting spin current $u \sin^2 \theta_2$ is shown in Fig. 5.3 as the solid black line. The qualitative agreement of both analytic theory and micromagnetic simulations is remarkable. Both critical current densities are almost perfectly predicted by the analytic calculations. In fact, the quantitative agreement is also good. For the low bias regime the deviation between both approaches is only given by the slope of the linear dependence. Since the analytic model was developed for the zero damping case, this is not surprising.

Moreover, the calculated fluid velocity u had to be renormalized by a factor of two to match the micromagnetic simulations. According to Ref. [40], the damping will affect the precessional frequency of the spin superfluid as

$$\Omega_d = \Omega \frac{1}{1 + \beta} \quad (5.22)$$

with the positive parameter β

$$\beta = \frac{2\pi\alpha sL}{\hbar}. \quad (5.23)$$

Here α is the Gilbert damping parameter, s the spin density and L the length of the transport channel. Since the fluid velocity is given by Eq. (5.11) the velocity in the presence of damping reads

$$\frac{u_d}{u} = 1 + \left(\frac{\beta}{1+\beta} \right). \quad (5.24)$$

Since $\beta \gg 1$ the velocity in the case of non-zero damping is given by $u_d \approx 2u$. Nevertheless, also the slope might slightly be affected.

The large bias regime seems to deviate more strongly from the analytically expected trend. For these large current densities, the stable spin texture in the active region is already formed. Two main contributions might affect the velocity of the spin superfluid. At first, the exact spin texture is not considered in the analytical model. Depending on the strength of the spin-transfer torque, the spin texture might change within the active region, and therefore influence the fluid velocity u . Additionally, the effect of the finite discretization size in the micromagnetic simulations has to be considered. Since the reorientation of the magnetization from in-plane to out-of-plane happens on a very small length scale, the cell size is crucial for the high bias regime. However, the overall trend does not change, only the fluid velocity is renormalized.

In order to understand the instability of the superfluid in more detail, the free energy

$$F = \frac{1}{2} \int dx \left[(\partial_x \theta)^2 + (\partial_x \varphi)^2 \sin^2 \theta + \cos^2 \theta \right] \quad (5.25)$$

has to be analyzed. To do so, the second variation of the free energy in θ has to be considered. Furthermore, we assume that $u = -\partial_x \varphi$ and θ_0 are constants that satisfy the equations of motion and boundary conditions discussed above. The superfluid will be unstable to fluctuations if the second variation corresponds to a saddle point in the free energy. The variation is given by

$$\delta^2 F = \frac{1}{2} \int dx \delta \theta(x) \left[-\partial_x^2 - 2(1-u^2) \cos(2\theta) \right] \delta \theta(x). \quad (5.26)$$

This variation can be negative, if the operator inside the brackets has negative eigenvalues. If we further assume $u < 1$, which is always the case for the investigated system, the spin superfluid will become unstable if $\cos(2\theta) > 0$, corresponding to $\theta < \pi/4$ and therefore to $m_z > 1/\sqrt{2}$.

Before discussing the impact of the dipole-dipole interactions on the superfluidic transport, it is valuable to discuss the spin superfluid in the presence of cubic anisotropy. Since the easy-plane anisotropy is stronger than the cubic anisotropy, only the in-plane contribution of the cubic anisotropy has to be considered. Thus, the energetic landscape is modified and easy directions are introduced within the plane of the film, resulting in a break of the

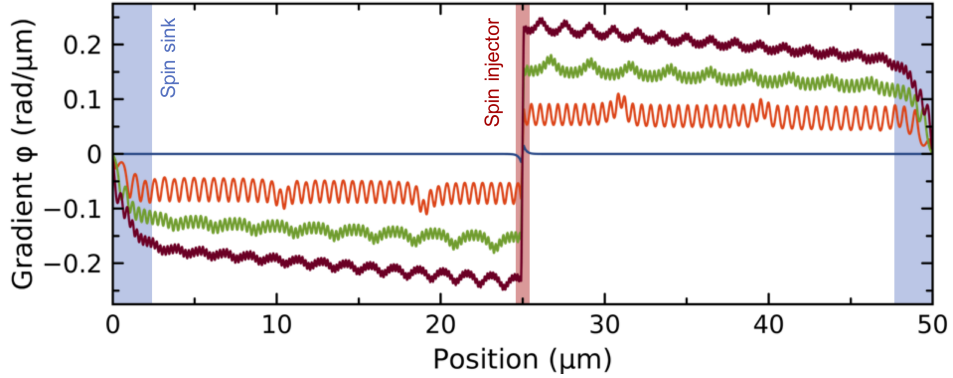


Figure 5.5.: Gradient of the in-plane angle φ as a function of the channel length with cubic in-plane anisotropy.

$U(1)$ symmetry. Since the system minimizes the total energy, spins close to the easy directions will rotate faster towards the easy anisotropy axes, when slightly increasing the exchange energy. As depicted in Fig. 5.5 the resulting gradient of the in-plane angle $\nabla\varphi$, and thus the fluid velocity u will be modulated along the transport channel. This distorted magnetization profile minimizes the total energy of the system. Since the magnetic ground state is aligned along one of the easy directions ($\vec{M} \parallel \hat{x}$) of the system, a threshold energy, respectively a threshold current density, is required to excite the superfluidic transport.

This symmetry-broken superfluid was already introduced by Sonin [37]. Since the homogenous rotation of the magnetization is perturbed, each full 2π rotation of the spin superfluid is considered an individual soliton² [37]. Therefore, the state can be interpreted as a chain of solitons traveling along the channel. Extending the theoretical description introduced by Sonin, one obtains a damped Sine-Gordon equation for the superfluidic transport [44, 82]. This type of equation is well-known in the fields of high-energy and particle physics [165–167]. Moreover, it is interesting to note that already Skyrme obtained the same equation [168]. One important class of solutions of this type of equation are solitons, shown in deep entanglement of the superfluidic transport with the motion of solitons.

Analyzing the modulation of the fluid velocity in detail yields two different periods directly linked to two frequencies present in the system.

As we now shall see, the dipole-dipole interaction will lead to very similar properties. Until now the superfluidic transport was only investigated without non-local dipole-dipole interactions. Realistic samples, e. g. , based on YIG will always have some non-zero thickness, and therefore dipole-dipole interactions will be present. To the knowledge of the author only two studies of spin superfluidity including full-scale micromagnetic simulations were published [43, 44]. However, both did not consider extended thin magnetic films.

²A soliton is a self-reinforcing wave packet.

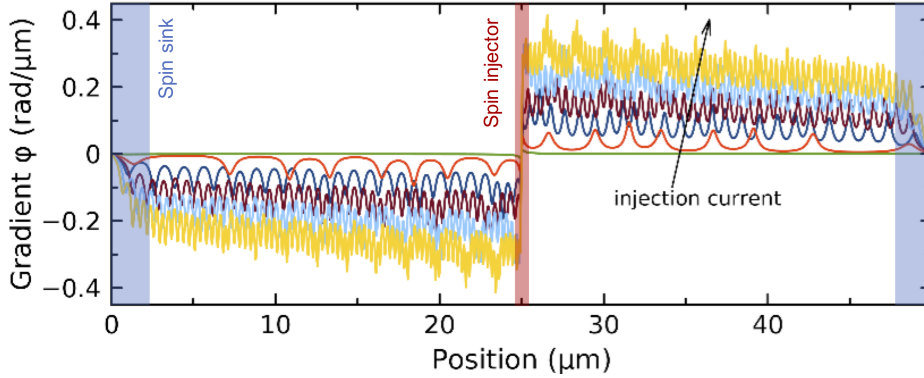


Figure 5.6.: Gradient of the in-plane angle ϕ as a function of channel length with enabled presence of non-local dipole interactions. The different colors represent different current densities ranging from 1.0×10^{10} A/m² to 1.6×10^{11} A/m². The current density step size is 3.0×10^{10} A/m².

The publication, even named "*Spin Superfluidity and Long-Range Transport in Thin-Film Ferromagnets*" [43], only considered magnetic microstructures. As it will be concluded in this section, the proper calculation of the magnetostatic field is crucial for the superfluidic transport in thin films. For this the calculation scheme applied to the magnetostatic field in MuMax³ will shortly be summarized.

In strong contrast to the long established micromagnetic simulation code OOMMF [94], MuMax³ relies on numerical integration to calculate the demagnetization tensor instead of Newell's expression [169]. As shown in the original publication of MuMax³, the accuracy of the numerical integration method is very good for finite sized systems and even for systems with PBC [127]. The calculation of the magnetostatic field in both simulation codes uses a supercell approach. However, in case of PBC not only the averaged demagnetization tensor is important, but also the symmetry of the tensor elements affects the magnetization dynamics. To study this influence in detail the demagnetization calculation of OOMMF for PBC was ported to MuMax³ [170] in the present work. Comparing both calculation methods shows that the newly implemented method slightly overestimates the magnetostatic field, but the symmetry is nicely calculated. Due to the decomposition of the magnetostatic field in three parts, purely analytic formulas can be employed. These formulas can be computed with a very high numerical accuracy, minimizing the total numerical error of the magnetostatic field. However, the original method implemented in MuMax³ usually slightly underestimates the magnetostatic field. The symmetry of the field can also be obtained using a large number of repetition to obtain a larger enough supercell for the PBC calculations, increasing the calculation time of the tensor significantly. For all simulations shown in this section, the newly implemented approach was used.

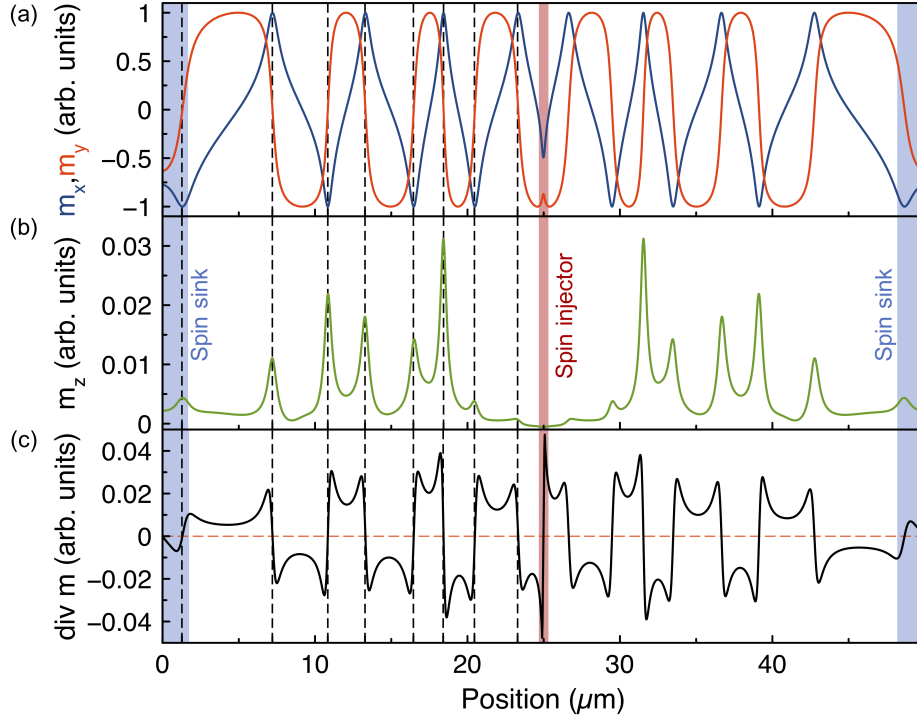


Figure 5.7.: Perturbed magnetization configuration of the superfluid state in the presence of dipole-dipole interaction. (a) In-plane components of the magnetization m_x (blue solid line) and m_y (red solid line). The deviation from a sine function is clearly visible. (b) depicts the out-of-plane component m_z . The peaks in this component always occur at the points with $m_x = -1$ and $m_x = 1$ marked by the vertical dashed lines. In (c) the divergence of the magnetization is shown. This quantity is directly linked to the magnetostatic field. The divergence is zero at the peaks in the m_z component.

Fig. 5.6 shows the gradient of the in-plane angle φ as a function of the distance from the injector. One of the main results of this study is directly visible in this figure. In very strong contrast to the publication mentioned above, superfluid transport is possible for very large length scales in ferromagnetic thin films. The linear dependence of the gradient on the distance is also achieved in the case of enabled dipole-dipole interactions. Nevertheless, peculiarities are visible. The blue solid line in Fig. 5.6 only shows non-zero values in the active regions. This leads to the conclusion, that the magnetostatic field induces a threshold current for the superfluid transport. Moreover, periodic spatial modulations are visible for all current density values shown in Fig. 5.6 are within the linear spin superfluidic regime. A detailed analysis shows that two different periods are present within this spin spiral. As already mentioned above, similar observations were made in easy-plane ferromagnets with additional in-plane anisotropy. In the case of the dipole-dipole interaction, the anisotropy introduced by the nonlocal interaction can be considered a two-fold anisotropy.

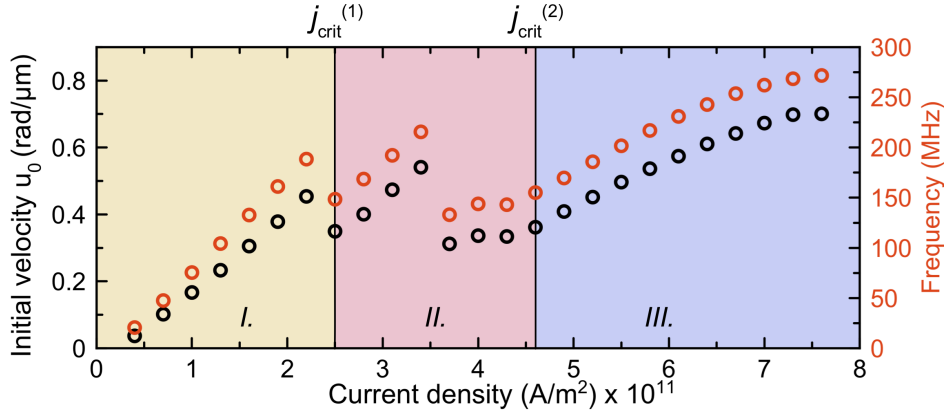


Figure 5.8.: Initial fluid velocity u_0 and frequency of the spin superfluid as a function of the injector current density in the presence of dipole-dipole interactions. Both quantities again shows three distinct regimes marked with yellow, red and blue, respectively.

To illustrate these non-homogenous rotations, Fig. 5.7 shows the magnetization configuration as a function of the distance away from the injector. Additionally, the divergence $\vec{\nabla} \cdot \vec{m} = \partial_x m_x$ was calculated and depicted in Fig. 5.7(c). The in-plane components m_x and m_y [Fig. 5.7(a)] show distinct deviations from a sine-like behavior. These deviations are a result of the dipole-dipole interactions. The magnetostatic field is mainly created by the volume charges in the system. Since the investigated structure is a one-dimensional transport channel, only the x -component contributes to the divergence. In Fig. 5.7(c) magnetic charges created by the spin spiral change sign every π rotation. The opposite charges attract each other, but can not annihilate. This attractive interaction reduces the distance between the magnetic charges at every π rotation, and thereby disturbs the spin superfluid.

The quantity m_z also shows peaks along the flow direction of the superfluid. For example shown in Fig. 5.7(b), every peak also corresponds to a π rotation. However, the analysis of different current densities reveals, that the wavelength of the modulation depends on the applied current density. Due to the non-homogenous rotations of the magnetization, the spin spiral can be considered as a chain of solitons.

To gain more insight into the effect of the dipole-dipole interactions on the superfluidic transport, again the initial fluid velocity u_0 and the frequency Ω for every simulated current density was extracted. The qualitative trend depicted in Fig. 5.8 resembles the trend without dipole-dipole interactions. The slope of the linear increase in the initial fluid velocity u_0 and the frequency Ω is very similar in the linear regime compared to the easy-plane case. Since the dipole-dipole interactions introduced a threshold current density as mentioned above, the observed deviations might just be a result of the sampling in the current density. Also the two other regimes agree very well with the easy-plane case. Both critical current

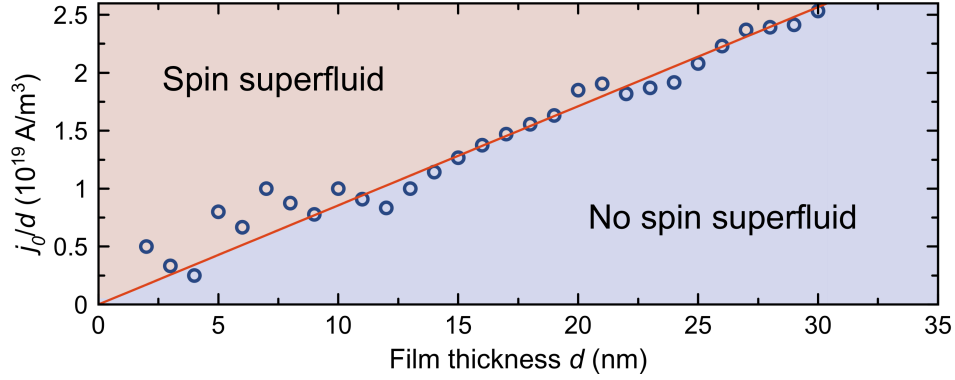


Figure 5.9.: Normalized threshold current j_0/d as a function of the film thickness d . The blue open symbols represent the simulation results. The red solid line is a guide to the eye using a linear function.

values seem to be affected by the dipole-dipole interactions. Nevertheless, the overall trend is perfectly reproduced.

At this point it is important to stress the significance of the results presented here. For both simulated systems the frequency-current response is very similar. That leads to the conclusion that spin superfluidity in thin ferromagnetic films might be observable in realistic systems.

In addition, the second periodicity observed in all simulations can be attributed to a second frequency. The m_z -component oscillates with the double frequency 2Ω compared to the in-plane components. Moreover, this excitation is located throughout the whole superfluidic channel. The out-of-plane component of each soliton is excited, and therefore this might be considered as an excitation of the soliton lattice. Nevertheless, the dispersion of the superfluid in the case of non-zero Gilbert damping, limits the length scale of those excitations. The author expects a perfect lattice forming the case of zero Gilbert damping. This case cannot easily be calculated using micromagnetic simulations, since zero damping might lead to unstable results while integrating, and therefore destroys the superfluidic state.

To further predict the possibility of the spin superfluidic state in ferromagnetic thin films, a phase diagram was calculated. For that reason, thin films with a different thickness ranging from 2 nm to 30 nm were simulated. For each thickness d the complete current dependence was recorded. The threshold current density was extracted for every simulation. However, in some cases the definition of the superfluidic state is complicated. Therefore, the definition by Sonin was chosen. The spin superfluidic state consists of multiple 2π windings [171]. Therefore, only states with multiple 2π windings after the total integration time were defined as superfluidic states. The extracted threshold current densities were renormalized by the thickness d to account for the scaling of the spin-transfer torque. The result is presented in Fig. 5.9. This reveals a linear scaling of the threshold current density with the film thick-

ness d . This scaling can be explained in the sense of the magnetostatic energy. Since the demagnetization tensor stays constant, only the volume of the system is changing, resulting in a linear increase of the magnetostatic energy. The injected spin current at first has to overcome this energy barrier, and therefore the scaling is linear.

Conclusion

To summarize, using large-scale micromagnetic simulations it was shown, that the spin superfluidity differs from other critical phenomena. Instead of a simple breakdown of the collective state at higher bias, the superfluid in ferromagnets undergoes two transitions. At first, the collective state is superimposed with incoherent magnons excited inside the injection region. Afterwards, the superfluidic transport is screened at higher current densities due to a local reorientation of the magnetization in the active region. Moreover, it was shown that the dipole-dipole interactions do not change the observed behavior qualitatively. Only a threshold current density, which linearly depends on the film thickness, is introduced. The spin spiral in the case of the dipole-dipole interactions is non-homogenous, since the system tries to minimize the magnetostatic energy. Moreover, the dipole-dipole interactions lead to a frequency doubling of the excitation of the m_z -component. The very remarkable fact of this investigation regarding the spin superfluidic transport is the universality of the models to describe this transport mode. The general behavior of the superfluid itself does not change, even if additional features like damping, dipole-dipole interactions or the effect of the finite discretization size are considered. All these additional contributions mainly renormalize key quantities but the observed physics stays the same.

The presented results might enable experimentalists to narrow the region of interest in the search for this special state in ferromagnetic materials. One important question regarding the spin superfluidity remains open. How does one achieve the injection of a spin current with a polarization perpendicular to the easy-plane in realistic systems? In the next section, a system is proposed to overcome this challenge.

5.2. Nanowires with Out-of-Plane Anisotropy

As already mentioned above, a thin magnetic film provides the challenge to achieve sufficient spin current injection with perpendicular polarization. In this section, a new system will be proposed to overcome this challenge.

The only condition the system has to fulfill is the presence of one easy-plane. In case of a thin ferromagnetic film, the magnetostatic field matches this condition. However, one can decompose this easy-plane anisotropy in two uniaxial anisotropies with perpendicular alignment. If the strengths of these two anisotropies are similar, a macrospin can rotate freely within the plane provided by the two uniaxial directions.

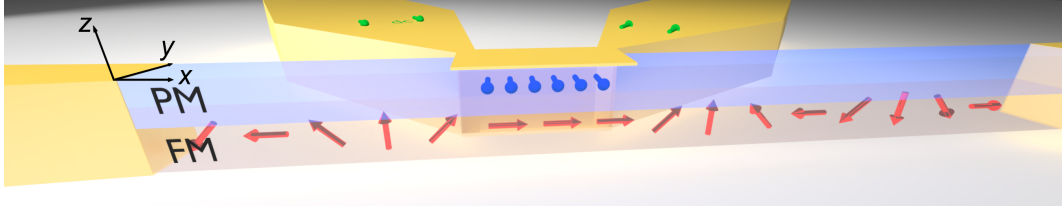


Figure 5.10.: Sketch of the NiCo nanowire with the superfluidic state excited. The red arrows indicate the spiraling magnetization excited by the spin-Hall effect (blue arrows) in the active region (gold).

The theoretically investigated system is a nanowire of length L with additional uniaxial out-of-plane anisotropy (PMA). The first anisotropy axis is provided by the shape anisotropy of the nanowire. Since the width w is chosen as $w/L \ll 1$, the magnetization would align with the long axis of the wire in the case of zero PMA. However, including a nonzero PMA, such as

$$\mu_0 N_{zz} H_{\text{Demag}} \approx \mu_0 H_{\text{anis}} \quad (5.27)$$

with the demagnetization tensor entry N_{zz} , leads to the formation of an easy-plane system. A sketch of the nanowire is shown in Fig. 5.10. In this system, the x - z plane provides an easy-plane.

All calculations were carried out in close collaboration with the group of Prof. Krivorotov at the University of California, Irvine. This group works on the experimental realization of the spin superfluidity in the presented system. Therefore, all magnetic and geometrical parameters were chosen according to the experimentally determined values. The experimentally investigated nanowire with the width $w = 40$ nm, length $L = 40$ μm and thickness $t = 5.6$ nm is grown as a multilayer of Ni and Co. Such superlattice structures consisting of these two materials are well known for their PMA [172–176]. However, a reduced width $w = 20$ nm was additionally investigated. To investigate the possibility of spin superfluidic transport, the phase diagram of the NiCo system was simulated. The uniaxial out-of-plane anisotropy (PMA) was implemented as a function of the device temperature, since all experiments were carried out using a cryostat. The device temperature was treated as an input parameter in the simulation script and results in a change of the anisotropy constant. Therefore, the difference between the PMA and the shape anisotropy can easily be controlled. The compensation temperature for which PMA and the shape anisotropy are balanced is ~ 55 K for the 40 nm wide wire and ~ 215 K for the 20 nm width.

In Fig. 5.11 the shape anisotropy for the different wire widths is compared to the PMA present in these systems. Both anisotropy contributions are calculated with the simulation code MuMax³. The dashed horizontal line indicates the compensation of both contributions and therefore, the point of spin reorientation for the system. Values smaller than zero or

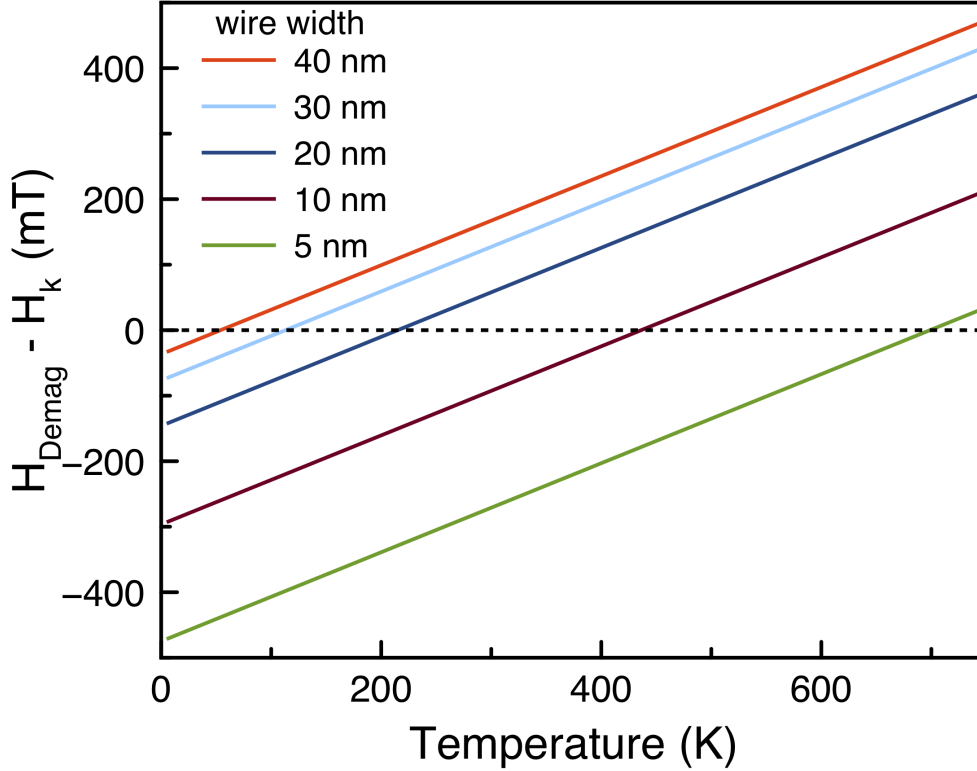


Figure 5.11.: Comparison of the shape anisotropy and the PMA for different wire widths. The dashed line indicates the spin reorientation transition.

larger than zero correspond to an equilibrium configuration out-of-plane or in-plane, respectively.

Using this as a starting point, multiple temperature values, and therefore PMA constants were considered. To minimize the storage capacity and computing time $20 \mu\text{m}$ long NiCo wires were chosen. During optimization of the simulations for the superfluidic transport, it became clear that PBCs are essential due to the weak dissipation present in the simulated system (the injected spin cannot be extracted fast enough and therefore the fluid velocity is reduced). However, combining PBCs with an exponential increase of the Gilbert damping constant towards the short edges of the wire provides satisfying results. Simulating longer wires for selected current densities might be beneficial to resolve the linear slope of the fluid velocity more nicely. Due to the small fluid velocity ($\sim 30\%$ than in YIG) in the NiCo system, the integration time for a $40 \mu\text{m}$ long NiCo wire was doubled to 500 ns.

The saturation magnetization of the NiCo multilayer was calculated as the average value of the saturation determined for Co ($M_s = 1422 \text{ kA/m}$) and Ni ($M_s = 485.4 \text{ kA/m}$). This results in a saturation magnetization of $M_s = 954 \text{ kA/m}$. Additional FMR investigations confirmed this value. Moreover, the exchange constant was assumed as the averaged con-

stant of Co and Ni, resulting in $A_{\text{ex}} = 14$ pJ/m. The PMA was extracted from temperature-dependent FMR measurements done at the UC Irvine. The PMA field at room temperature is given by

$$\mu_0 H_k^{\text{RT}} = \frac{4587.5}{t} \text{ [T} \cdot \text{nm]}. \quad (5.28)$$

Moreover, the temperature dependence of the anisotropy was determined as:

$$\mu_0 H_k(T) = \left[1 + \frac{0.24(300 - T)}{300} \right] \mu_0 H_k^{\text{RT}}. \quad (5.29)$$

The Gilbert damping constant was set to $\alpha = 0.02$. The applied current density was varied between 8×10^{11} A/m² and 2×10^{12} A/m² with a step size of 2.5×10^{10} A/m². For each current density the magnetization configuration is recorded every 100 ps while integration over 500 ns. To distinguish between normal fluidic states, superfluidic states, and autooscillations, the gradient of the easy-plane angle $\nabla\varphi$ was calculated for every magnetization configuration.

Influence of the Dipole-Dipole Interactions

As already shown in Chapter 5.1, dipole-dipole interactions strongly influence the symmetry of the superfluidic state. Since NiCo has a considerably larger saturation magnetization M_s than YIG, the effect will be more prominent in this system. In addition, the dipole-dipole interaction plays a crucial role for the stability of the superfluid in the nanowire. The magnetostatic field provides one of the uniaxial anisotropies needed for the compensated state. To understand the influence of the saturation magnetization in detail, a toy model is considered. Therefore, two different systems were simulated. For the first system, material parameters similar to YIG were chosen. Additionally, an out-of-plane anisotropy was introduced artificially to compensate the shape anisotropy. Recent advancement in the field of crystal growth, such as YIG on Bismuth substituted Gadolinium Gallium Garnet, $\text{Gd}_3\text{Ga}_5\text{O}_{12}$ [177, 178], (sGGG) or $\text{Tm}_3\text{Fe}_5\text{O}_{12}$ (TIG) [179] might be candidates for the experimental realization of the spin superfluidity.

The second system is the aforementioned NiCo superlattice. Fig. 5.12 shows the difference in the gradient of the easy-plane angle for two different widths (20 nm and 40 nm) of the nanowire. The larger saturation magnetization M_s and, thus, the larger dipole-dipole fields lead to strongly non-uniform rotations of the magnetization in the x - z plane. This directly points to the fact that the system is only compensated within a macro spin approach. Micromagnetically, the same effect as mentioned before has to be considered. The volume charges produced by the divergence of the magnetization, and therefore the magnetostatic field, will be minimized. However, superfluidic transport still seems to be possible.

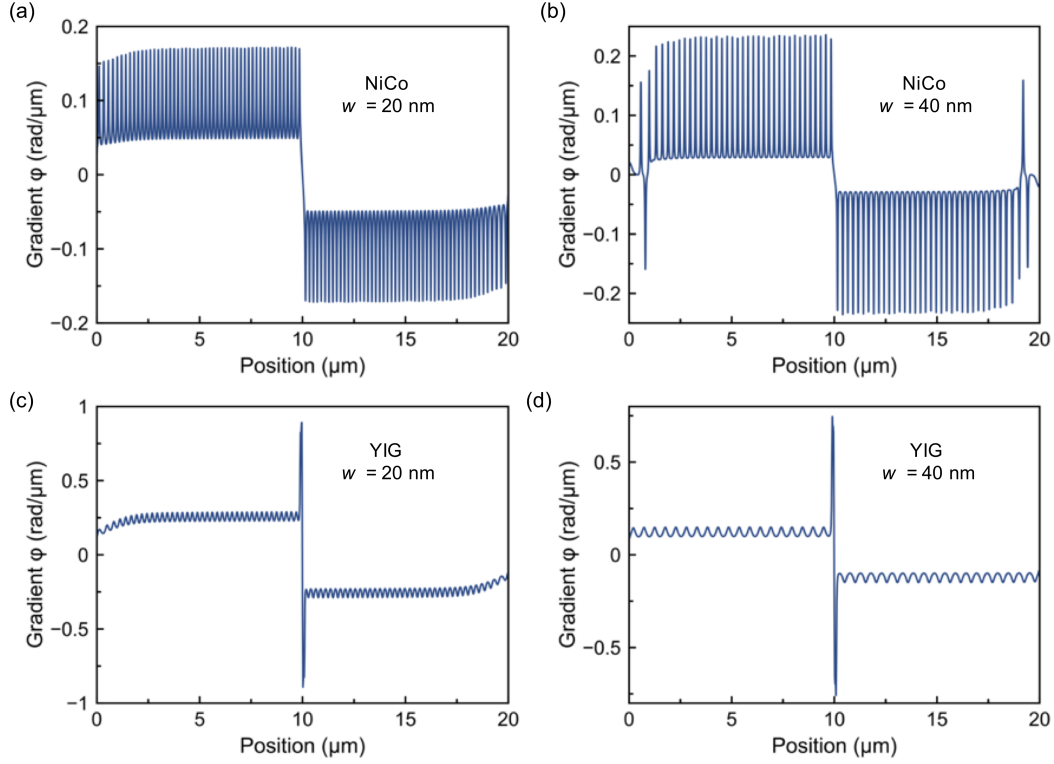


Figure 5.12.: Gradient of the easy-plane angle φ for (a) a 20 nm wide NiCo wire, (b) a 40 nm wide NiCo wire, (c) a 20 nm wide YIG wire and (d) a 40 nm wide YIG wire. The out-of-plane anisotropy was balanced according to the calculated magnetostatic field.

The 40 nm NiCo Wire

The frequency response of the system as a function of the injector current is shown in Fig. 5.13. The dynamic response of the system roughly can be divided into three regimes. At first the superfluidic transport, in the area between $0.8 \times 10^{12} \text{ A/m}^2$ and $1.1 \times 10^{12} \text{ A/m}^2$. The gradient $\nabla\varphi$ indicates the presence of the superfluidic transport, but no signature of such state is present in the frequency response. One explanation for the observed behavior might be that the frequencies of the state are below 10 MHz. Only an increase of the dynamic response towards zero frequency is present, as visible in Fig 5.13. For higher bias current densities two autooscillation modes are observed with a narrow linewidth. Both modes are stable within the broad current range from approximately $1.3 \times 10^{12} \text{ A/m}^2$ to $1.8 \times 10^{12} \text{ A/m}^2$. As clearly visible in Fig. 5.13, both modes exhibit a slightly different non-linear frequency shift as function of the bias current, indicating the different nature of both modes. Since, the width of 40 nm seems to be large enough to form a spin texture across the width of the wire, two different modes might be excited in the system. This behavior was especially observed when the PMA and the shape anisotropy were exactly balanced. Therefore, the

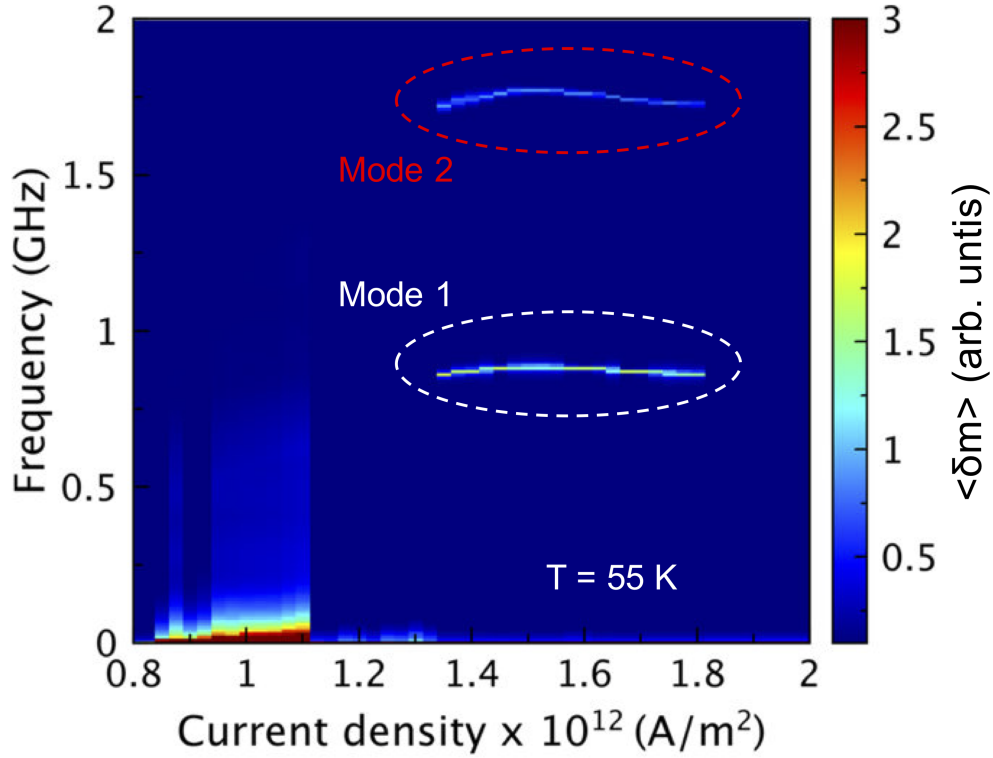


Figure 5.13.: Color-coded dynamic response of the magnetization as a function of frequency Ω and injector current density j for the compensated 40 nm wide NiCo wire. Superfluidic transport at very low frequencies, as well as autooscillations can be observed for the compensated system. Two different spin wave modes are excited around 1 GHz and 1.75 GHz.

formation of the spin texture is mainly driven by the dynamic dipole-dipole interactions in the spin spiral. It seems that the spin texture reduces the superfluid flow and even stops it in certain cases. Nevertheless, this problem might not occur in experiments, since the simulations are done at $T = 0$ K.

To further investigate the influence of the ratio of shape and out-of-plane anisotropy, multiple cases have been computed. The results are summarized in Fig. 5.14, focusing on important temperatures, and therefore anisotropies. If the residual PMA is too large, e.g. for 30 K, neither a superfluidic state nor autooscillations are excited. The temperature of 30 K corresponds to a residual anisotropy of $H_{\text{Demag}} - H_k = -16.3$ mT. However, slightly increasing the temperature to 35 K, evidences for a possible superfluidic transport with smaller frequencies are present again. Increasing the temperature further towards the compensation point results in an increase of the current range supporting the very small frequency response, as visible for 45 K [Fig. 5.14(b)]. No autooscillations were observed within the investigated current range. As already discussed above, the compensated case

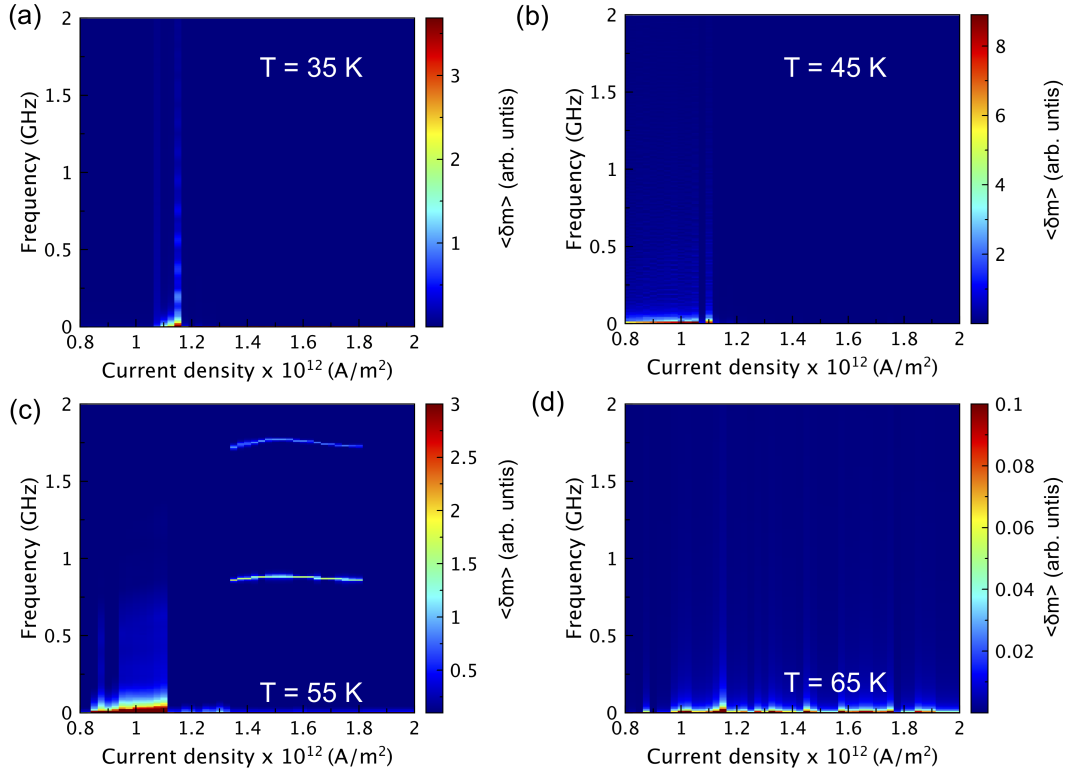


Figure 5.14.: Color-coded dynamic response of the magnetization as a function of frequency Ω and injector current density j for the 40 nm wide NiCo wire with different strengths of the uniaxial anisotropy. (a) and (b) represent the dynamic response below the compensation temperature, which is shown in (c). (d) was obtained for a temperature value above the compensation temperature. Neither show a clear evidence for superfluidic transport nor autooscillations.

might support both, superfluidity and autooscillations. Nevertheless, the transition is rather sharp. The PMA only changes by 1.3% for 35 K compared to the compensation. However, no additional investigations regarding the 40 nm width have been performed, due to the very small frequencies observed in the simulations. To overcome this challenge, a 20 nm wide NiCo wire has been considered.

The 20 nm NiCo Wire

To understand the influence of the spin texture across the width of the wire and the dynamic dipole-dipole interactions, the wire width was reduced to 20 nm. According to analytic calculations the compensation temperature is approximately 215 K. Since the width in the case of the nanowires plays the role of the thickness in films, a reduction of the critical current and less influence of the dynamic dipole-dipole interactions are expected. The results for selected temperatures are shown in Fig. 5.15. In strong contrast to the 40 nm wide wire clear

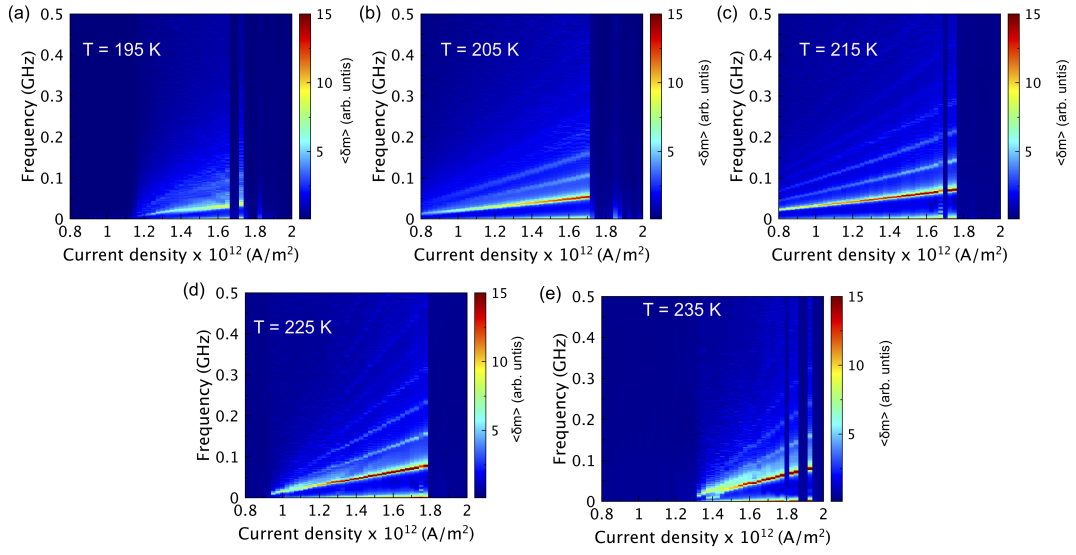


Figure 5.15.: Color-coded dynamic response of the magnetization as a function of frequency Ω and injector current density j for the 20 nm wide NiCo wire with different strengths of the uniaxial anisotropy. All simulated anisotropy strengths supported the superfluidic transport. The stability of the superfluidic state depends strongly on the anisotropy strength.

indications for spin superfluidity are present in both, the gradient of the easy-plane angle and the frequency. For the compensated case ($T = 215$ K) a frequency response around 50 MHz to 100 MHz is observed. The selected minimal current density is even slightly too high, confirming the reduction of the threshold current, and thus the influence of the dipole-dipole interactions.

For both lower and higher temperatures, corresponding to the same identical effective magnetizations as for the 40 nm wide wire, superfluidic transport is observed for all cases. The threshold current density depends on the effective magnetization. For $T = 195$ K, a threshold of $j \approx 1.2 \times 10^{12}$ A/m² is observed [Fig. 5.15(a)]. Comparing the threshold values for Figs. 5.15(a)-(b) and Figs. 5.15(d)-(e), shows an interesting property. For temperature values below 215 K the PMA is strong, changing in favor of the shape anisotropy for larger temperatures. The threshold current values are not symmetrically distributed around the compensation points. This shows a clear indication, that both anisotropies cannot be treated equally. Depending on the dominating contribution, the properties of the spin superfluid are changing.

Besides the superfluidic transport, no autooscillations are observed at the investigated current density range. Nevertheless, it might be possible, that autooscillations will be excited for different current values.

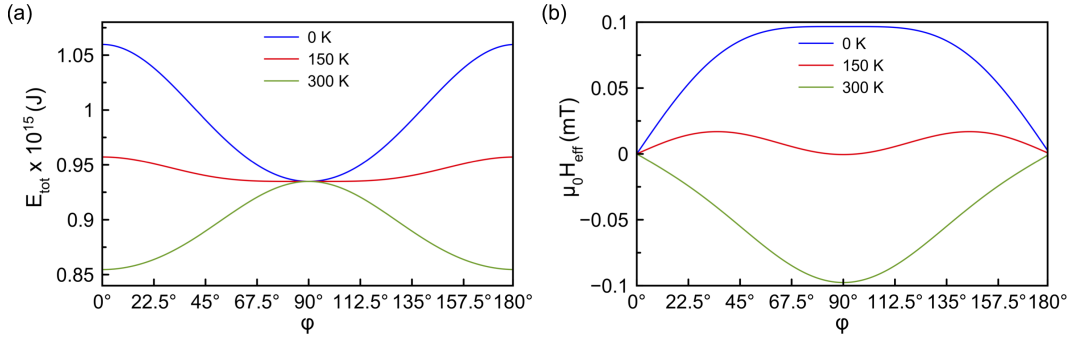


Figure 5.16.: Anisotropy energy (a) and anisotropy field including the second-order anisotropy in a 20 nm NiCo wire. No perfect compensation can be achieved in the presence of the second-order anisotropy, leading to a suppression of the superfluidic transport.

So far, only the first order PMA was considered in the simulations. However, the NiCo system is known to show a rather larger second order anisotropy [180]. To the knowledge of the author, no study measuring the second order contribution as a function of temperature is available. Theoretical calculations predicted a power-law dependence of the anisotropy constant on the temperature [181]. The exponent of the power-law is thereby determined by the order of the anisotropy. This behavior is supported by experiments for cubic Fe on GaAs [182]. Since the main goal of this study was to supply frequency and current density ranges for the experiments done at the UC Irvine, the same scaling as for the first order constant was assumed, since no direct measurement exists for the NiCo multilayers.

For all investigated current densities and widths it was not possible to excite the spin superfluid with the second order anisotropy present. To further understand this strong suppression of the spin superfluid, the total energy E_{tot} as well as the effective field $\mu_0 H_{\text{eff}}$ was calculated as a function of the easy-plane angle for various temperatures. All magnetic moments were rotated simultaneously, and therefore the calculation resembles the macro-spin approach. The resulting effective field and total energy for $T = 0$ K, $T = 150$ K and $T = 300$ K are shown in Fig. 5.16. Since the angular dependences of the energy for second $\propto \sin^4$ and first order $\propto \sin^2$ uniaxial anisotropies differ, no easy-plane system can be achieved. For the two limits $T = 0$ K and $T = 300$ K, the difference between the first order PMA and the shape anisotropy dominates both the total energy E_{tot} , as well as the effective field $\mu_0 H_{\text{eff}}$. The energy is almost perfectly 180° symmetric [Fig. 5.16(a)]. However, in the effective field the contribution of the second order anisotropy is directly visible, resulting in a distorted 180° -symmetry [Fig. 5.16(b)]. The new compensation point with the included second order contribution is $T = 150$ K. As visible in Fig. 5.16(b), a residual anisotropy field of approximately 15 mT results, leading to the suppression of the spin superfluid.

Conclusion

In conclusion, the collective spin transport, referred to as spin superfluidity, was numerically investigated for two different systems. For the thin-film system, two very important conclusions were obtained:

1. Two previously unknown transport regimes were found in using micromagnetic simulations as well as analytic theory. The *oscillatory* regime is subject to a self-stabilization mechanism. The superfluid phase is stabilized emitting incoherent spin waves in the transport channel.
2. Dipole-dipole interactions do not suppress the long-distance transport.

To overcome challenges regarding the experimental investigations, a nanowire system was investigated. The prototype nanowire made of NiCo exhibits a large PMA to compensate the shape anisotropy, and therefore fulfills the condition for the superfluid transport. Nevertheless, only for widths of 20 nm or smaller, spin superfluidity is possible. Moreover, it was shown, that the second-order uniaxial anisotropy suppresses the superfluid.

6. Conclusion and Outlook

This thesis entitled "Spin dynamics and transport in magnetic heterostructures" presented two important topics devoted to the field of magnonics.

The first part of the thesis focused on the excitation and guiding of nonreciprocal spin waves in magnetic bilayers. An analytic theory of the spin-wave dispersion in magnetic bilayers supported by micromagnetic simulations as well as experiments was presented. The nonreciprocity induced by the dynamic intralayer dipole-dipole interactions theoretically reaches 8.5 GHz for 20 nm thick magnetic layers. The derived analytic spin-wave dispersion has many similarities with the frequency shift induced by the Dzyaloshinskii-Moriya interaction for small wave numbers. The micromagnetic simulations show an almost perfect agreement with the analytic theory. For larger wave numbers both approaches slightly deviate, due to the confinement of the spin-wave amplitude close to the surfaces of the magnetic bilayer. Two prototype systems were experimentally investigated utilizing ferromagnetic resonance spectroscopy, magnetometry, transmission electron microscopy, and Brillouin light scattering. The first system consisted of two $\text{Ni}_{81}\text{Fe}_{19}$ layers separated by a 5-nm Cu spacer. To achieve the antiparallel alignment of the magnetic bilayer the antiferromagnet IrMn was deposited in contact with one of the $\text{Ni}_{81}\text{Fe}_{19}$ layers. The second system was composed of a $\text{Ni}_{81}\text{Fe}_{19}$ layer and a $\text{Co}_{40}\text{Fe}_{40}\text{B}_{20}$ layer separated by a thin Ir spacer. The antiparallel alignment is achieved by the interlayer exchange coupling of both magnetic layers.

The ferromagnetic resonance measurements for the first system indicate the presence of an exchange bias field of approximately $\mu_0 H_{\text{eb}} = 10$ mT. However, the Brillouin light scattering results were not promising. Therefore, additional characterization were not performed.

For the second layer stack the full characterization was performed. By combining the ferromagnetic resonance results with the magnetometry and micromagnetic simulations the bilinear (biquadratic) interlayer exchange coupling constants J_1 (J_2) were successfully determined. The transmission electron microscopy measurements provided the structural information needed to calculate the spin-wave dispersion of the system. The Brillouin light scattering measurements show the predicted nonreciprocity in the antiparallel state with a maximum frequency shift of $\Delta f = 2.2$ GHz. Very good agreement with the analytic theory

is achieved by tilting the magnetization of each layer by 25° . The tilt is supported by the magnetometry indicating a non-perfect antiparallel state for small magnetic fields.

Besides the spin-wave dispersion also the topological spin-wave emission in microstructured magnetic bilayers consisting of thick magnetic layers investigated by scanning transmission x-ray microscopy was presented. Since the size of the elliptical structures are in the micrometer range, the analytic theory as well as micromagnetic simulations for extended bilayers almost perfectly resemble the dispersion in such devices. The microstructuring leads to the formation of a spin texture composed of an elongated vortex state separated by a domain wall. Both building blocks of this spin texture can emit spin waves if excited homogeneously. The vortex core emits spin waves locally confined to the domain wall at low frequencies. For higher frequencies the emission of a plane wave originating at the domain wall was observed. This topological emission is explained by the gap in the spin-wave dispersion. The mechanism of the plane wave emission is explained by the antiphase breathing of the domain walls in both magnetic layers. With this new concept it is possible to excite spin waves with ultra-short wavelength. The lower bound is provided by the domain wall width of the system. Combined with the nonreciprocal transport, this study is an important step towards the application of magnonic devices in the information and telecommunication technology.

The second part of this thesis presented the concept of spin superfluidity in ferromagnetic thin films. For the numerical study of the spin superfluid excited locally by means of spin-transfer torque, the prototype system YIG was chosen. Two cases: (i) omitting and (ii) including dipole-dipole interactions were considered.

It was found that in strong contrast to previous studies, the spin superfluidic transport is **not** suppressed by the presence of dipole-dipole interactions. Two distinct alterations compared to previous works led to this finding: (i) extended thin magnetic film were considered and (ii) the magnetostatic field was calculated very carefully regarding its symmetry and strength. This very important result might encourage new experimental endeavors to realize the spin superfluidity in ferromagnetic thin films. In addition to this, the numerical results show the existence of three distinct regimes depending on the injection current strength.

For small injection currents the traditional superfluid regime in good accordance to literature is obtained. In this regime the fluid velocity as well as the base frequency of the spin superfluid linearly increases with the injection current.

Further increase of the bias current leads to a reduction of the fluid velocity and the base frequency. Moreover, incoherent oscillations were observed in the transport channel. The reduction of both frequency and velocity can be explained in sense of a superposition of the spin superfluid with the "normal" fluid, given by spin waves. The incoherent magnons are excited in the active region by the parametric excitation of the injector region. The

critical current density needed for the breakdown strongly depends on the injector width, supporting the hypothesis of parametrically pumped autooscillations. Therefore, the second regime is termed *oscillatory* regime.

The third regime is defined by the stable spin texture introduced inside the active region by the very strong spin-transfer torque. The increase of the injector current is followed by the overdamping of the active region, and therefore, to a localized switching of the magnetization. At first, the fluid velocity still increases in this regime, but quickly saturates. Further increase leads to a reduction following the trend $1/j$. The existence of the three regimes is supported by an analytic theory, predicting the critical current.

Besides persistent superfluidic transport in the presence of dipole-dipole interactions, additional impacts were observed. At first, a threshold current is introduced, given by the magnetostatic energy of the system. Furthermore, the coherent rotation of the magnetization in the presence of dipolar interactions is modified. The magnetic charges produced by the spin spiral attract each other, but do not annihilate, leading to the distorted profile of the spin superfluid. The profile can be considered as a chain of dispersive solitons, showing the deep entanglement of the spin superfluidic transport and the sine-Gordon equation. Additionally, the excitation of this soliton lattice can be observed at twice the frequency of the spin superfluid. To deepen the understanding of the influence of the dipole-dipole interactions, the threshold current as a function of the film thickness was simulated. The resulting phase diagram shows a linear increase of the threshold current, as aspected by the linear increase in the magnetostatic energy.

To further provide a new experimental approach to the spin superfluid, a nanowire system consisting of Ni and Co multilayers with out-of-plane anisotropy was investigated. For this system the injector of the spin polarized current could be achieved by means of the spin-Hall effect. The "film thickness" is now given by the width of the nanowire, providing an upper bound for the latter. Two widths, 40 nm and 20 nm, were considered. For the larger width, only parametrically excited autooscillations were observed, the narrow wire showed clear indications for spin superfluidity in the micromagnetic simulations. However, the mentioned material system is known to exhibit an additional second-order anisotropy, directly leading to the suppression of the spin superfluid.

The direct combination of spin waves and spin superfluid would enable a very broad playground for applications based on magnonic devices. By directly exciting spin waves to control the spin superfluid frequency and also to transport additional information new concepts for neuromorphic computing or telecommunication based on magnons could be developed.

A. Appendix

A.1. Coefficient for FMR in Coupled Bilayers

$$b = \frac{f_{\theta_1\theta_1}f_{\varphi_1\varphi_1} - f_{\theta_1\varphi_1}^2}{d_1^2 M_1^2 \gamma_2^2 \sin^2 \theta_1^{\text{eq}}} + \frac{f_{\theta_2\theta_2}f_{\varphi_2\varphi_2} - f_{\theta_2\varphi_2}^2}{d_2^2 M_2^2 \gamma_1^2 \sin^2 \theta_2^{\text{eq}}} + 2 \frac{f_{\theta_1\theta_2}f_{\varphi_1\varphi_2} - f_{\theta_1\varphi_2}f_{\theta_2\varphi_1}}{d_1 d_2 M_1 M_2 \gamma_1 \gamma_2 \sin \theta_1^{\text{eq}} \sin \theta_2^{\text{eq}}} \quad (1.1)$$

$$c = \frac{1}{d_1^2 d_2^2 M_1^2 M_2^2 \sin^2 \theta_1^{\text{eq}} \sin^2 \theta_2^{\text{eq}}} \left[f_{\theta_1\theta_2}^2 f_{\varphi_1\varphi_2}^2 + f_{\theta_1\varphi_1}^2 f_{\theta_2\varphi_2}^2 + f_{\theta_1\varphi_2}^2 f_{\theta_2\varphi_1}^2 \right. \\ - f_{\theta_1\theta_2}^2 f_{\varphi_1\varphi_1} f_{\varphi_2\varphi_2} - f_{\varphi_1\varphi_2}^2 f_{\theta_1\theta_1} f_{\theta_2\theta_2} - f_{\theta_2\varphi_2}^2 f_{\theta_1\theta_1} f_{\varphi_1\varphi_1} - f_{\theta_1\varphi_2}^2 f_{\theta_2\theta_2} f_{\varphi_1\varphi_1} \\ - f_{\theta_1\varphi_1}^2 f_{\theta_2\theta_2} f_{\varphi_2\varphi_2} - f_{\theta_2\varphi_1}^2 f_{\theta_1\theta_1} f_{\varphi_2\varphi_2} + f_{\theta_1\theta_1} f_{\varphi_1\varphi_1} f_{\theta_2\theta_2} f_{\varphi_2\varphi_2} \\ + 2f_{\theta_1\theta_1} f_{\varphi_1\varphi_2} f_{\theta_2\varphi_1} f_{\theta_2\varphi_2} + 2f_{\theta_1\varphi_1} f_{\theta_1\varphi_2} f_{\varphi_1\varphi_2} f_{\theta_2\theta_2} + 2f_{\theta_1\theta_2} f_{\theta_1\varphi_2} f_{\varphi_1\varphi_1} f_{\theta_2\varphi_2} \\ + 2f_{\theta_1\theta_2} f_{\theta_1\varphi_1} f_{\theta_2\varphi_1} f_{\varphi_2\varphi_2} - 2f_{\theta_1\varphi_1} f_{\theta_2\varphi_2} f_{\theta_1\theta_2} f_{\varphi_1\varphi_2} - 2f_{\theta_1\varphi_1} f_{\theta_2\varphi_2} f_{\theta_1\varphi_2} f_{\theta_2\varphi_1} \\ \left. - 2f_{\theta_1\theta_2} f_{\varphi_1\varphi_2} f_{\theta_1\varphi_2} f_{\theta_2\varphi_1} \right]. \quad (1.2)$$

A.2. Matrix Elements

The matrix \tilde{A} has following entries:

$$\tilde{A} = \begin{pmatrix} A_{X_1}^{X_1} & A_{Y_1}^{X_1} & A_{X_2}^{X_1} & A_{Y_2}^{X_1} \\ A_{X_1}^{Y_1} & A_{Y_1}^{Y_1} & A_{X_2}^{Y_1} & A_{Y_2}^{Y_1} \\ A_{X_1}^{X_2} & A_{Y_1}^{X_2} & A_{X_2}^{X_2} & A_{Y_2}^{X_2} \\ A_{X_1}^{Y_2} & A_{Y_1}^{Y_2} & A_{X_2}^{Y_2} & A_{Y_2}^{Y_2} \end{pmatrix}. \quad (1.3)$$

$$A_{X_1}^{X_1} = 0, \quad (1.4a)$$

$$A_{Y_1}^{X_1} = -M_s^{(1)} \zeta(k, d_1) - M_s^{(1)} [\lambda_{\text{ex}}^{(1)}]^2 k^2 - H_{Z_1}^{e0} - H_s^{(1)}, \quad (1.4b)$$

$$A_{X_2}^{X_1} = iM_s^{(1)} \sin \varphi_2 \frac{kd_2}{2} \zeta(k, d_1) \zeta(k, d_2) e^{-|k|s}, \quad (1.4c)$$

$$A_{Y_2}^{X_1} = M_s^{(1)} \frac{|k|d_2}{2} \zeta(k, d_1) \zeta(k, d_2) e^{-|k|s} + \frac{J_1 + 2J_2 \cos(\varphi_1 - \varphi_2)}{d_1 M_s^{(2)}}. \quad (1.4d)$$

$$\begin{aligned} A_{X_1}^{Y_1} &= M_s^{(1)} \sin^2 \varphi_1 [1 - \zeta(k, d_1)] + M_s^{(1)} [\lambda_{\text{ex}}^{(1)}]^2 k^2 \\ &\quad - H_u^{(1)} \cos^2 \varphi_1 + H_{Z_1}^{e0} - \frac{2J_2}{d_1 M_s^{(1)}} \sin^2(\varphi_1 - \varphi_2), \end{aligned} \quad (1.5a)$$

$$A_{Y_1}^{Y_1} = 0, \quad (1.5b)$$

$$\begin{aligned} A_{X_2}^{Y_1} &= M_s^{(1)} \sin \varphi_1 \sin \varphi_2 \frac{|k|d_2}{2} \zeta(k, d_1) \zeta(k, d_2) e^{-|k|s} \\ &\quad - \frac{J_1 \cos(\varphi_2 - \varphi_1) + 2J_2 \cos[2(\varphi_1 - \varphi_2)]}{d_1 M_s^{(2)}}, \end{aligned} \quad (1.5c)$$

$$A_{Y_2}^{Y_1} = -iM_s^{(1)} \sin \varphi_1 \frac{kd_2}{2} \zeta(k, d_1) \zeta(k, d_2) e^{-|k|s}. \quad (1.5d)$$

$$A_{X_1}^{X_2} = -iM_s^{(2)} \sin \varphi_1 \frac{kd_1}{2} \zeta(k, d_1) \zeta(k, d_2) e^{-|k|s}, \quad (1.6a)$$

$$A_{Y_1}^{X_2} = M_s^{(2)} \frac{|k|d_1}{2} \zeta(k, d_1) \zeta(k, d_2) e^{-|k|s} + \frac{J_1 + 2J_2 \cos(\varphi_1 - \varphi_2)}{d_2 M_s^{(1)}}, \quad (1.6b)$$

$$A_{X_2}^{X_2} = 0, \quad (1.6c)$$

$$A_{Y_2}^{X_2} = -M_s^{(2)} \zeta(k, d_2) - M_s^{(2)} [\lambda_{\text{ex}}^{(2)}]^2 k^2 - H_{Z_2}^{e0} + H_s^{(2)}. \quad (1.6d)$$

$$A_{X_1}^{Y_2} = M_s^{(2)} \sin \varphi_1 \sin \varphi_2 \frac{|k| d_1}{2} \zeta(k, d_1) \zeta(k, d_2) e^{-|k|s} - \frac{J_1 \cos(\varphi_1 - \varphi_2) + 2J_2 \cos[2(\varphi_1 - \varphi_2)]}{d_2 M_s^{(1)}}, \quad (1.7a)$$

$$A_{Y_1}^{Y_2} = i M_s^{(2)} \sin \varphi_2 \frac{k d_1}{2} \zeta(k, d_1) \zeta(k, d_2) e^{-|k|s}, \quad (1.7b)$$

$$A_{X_2}^{Y_2} = M_s^{(2)} \sin^2 \varphi_2 [1 - \zeta(k, d_2)] + M_s^{(2)} [\lambda_{\text{ex}}^{(2)}]^2 k^2 - H_u^{(2)} \cos^2 \varphi_2 + H_{Z_2}^{e0} - \frac{2J_2}{d_2 M_s^{(2)}} \sin^2(\varphi_1 - \varphi_2), \quad (1.7c)$$

$$A_{Y_2}^{Y_2} = 0. \quad (1.7d)$$

with

$$\zeta(k, d_v) = \frac{\sinh(kd_v/2) e^{-|k|d_v/2}}{kd_v/2}, \quad (1.8)$$

and

$$H_{Z_v}^{e0} = H \cos(\varphi_h - \varphi_v) + H_u^{(v)} \sin^2 \varphi_v + \frac{J_1 \cos(\varphi_1 - \varphi_2) + 2J_2 \cos^2(\varphi_1 - \varphi_2)}{d_v M_s^{(v)}}. \quad (1.9)$$

A.3. The Effect of Windowing

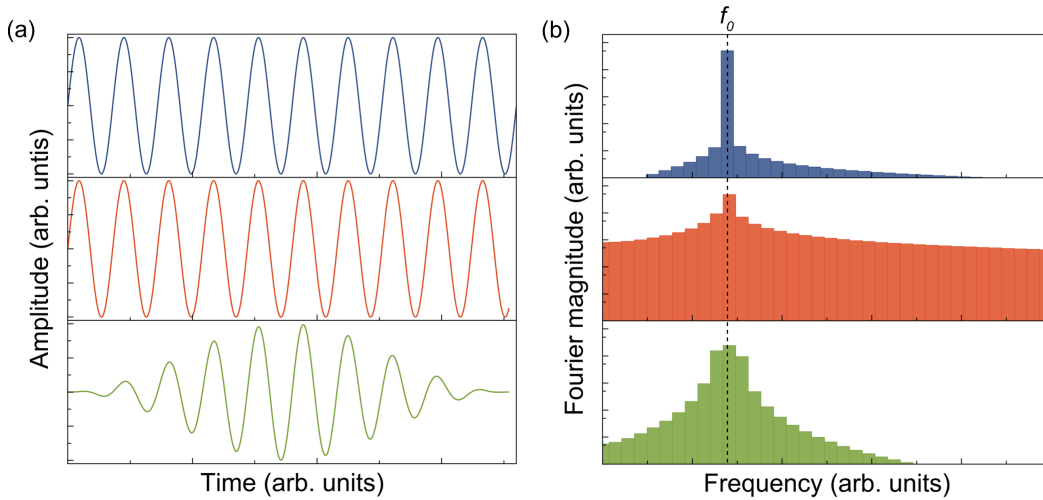


Figure A.1.: Effect of a Hann window function on the result of a FFT. (a) shows a sine wave with frequency f_0 for an integer number of periods (upper panel), for a non-integer number of periods (middle panel) and a windowed sine wave with frequency f_0 for a non-integer number of periods. The corresponding FFT spectra are shown in (b).

The effect of the window function in Fourier transformations is depicted in Fig. A.1. To illustrate the influence of the window function a sine function with a single frequency is considered. The left panels [Fig. A.1(a)] shows an ideal sine wave with an integer number of periods (upper panel), a sine wave with a non-integer number of periods (middle panel) and the windowed sine wave with a non-integer number of periods (bottom panel). The FFT assumes that the provided data set contains at least one complete period of the signal. If the two endpoints are not identical, higher frequencies show up in the FFT. Since this high-frequency components may be higher than the Nyquist frequency, they are aliased between 0 and half of the sampling rate. The obtained FFT spectrum is broadened and the energy is distributed into other frequency. This is illustrated in Fig. A.1(b). The upper panel represents the FFT of the perfect sine wave, resulting in a delta peak at the single frequency. The float-point accuracy leads to a small redistribution of the energy even for this case. The middle panel shows the FFT of the sine wave with the non-integer number of periods. The energy is strongly redistributed over the whole frequency range. This spectral leakage of the FFT is suppressed for the windowed sine wave, as shown in the bottom panel. The window function varies of the amplitude of the original signal. This results in a periodic signal.

Bibliography

- [1] I. S. Jacobs, „*Role of Magnetism in Technology*“, J. Appl. Phys. **40**, 917 (1969).
- [2] R. McCallum, L. Lewis, R. Skomski, M. Kramer and I. Anderson, „*Practical Aspects of Modern and Future Permanent Magnets*“, Annu. Rev. Mater. Res. **44**, 451 (2014).
- [3] J. Lenz and S. Edelstein, „*Magnetic sensors and their applications*“, IEEE Sensors Journal **6**, 631 (2006).
- [4] S. A. Wolf, „*Spintronics: A Spin-Based Electronics Vision for the Future*“, Science **294**, 1488 (2001).
- [5] A. Fert, „*Nobel Lecture: Origin, development, and future of spintronics*“, Rev. Mod. Phys. **80**, 1517 (2008).
- [6] M. N. Baibich, J. M. Broto, A. Fert, F. N. V. Dau, F. Petroff, P. Etienne, G. Creuzet, A. Friederich and J. Chazelas, „*Giant Magnetoresistance of (001)Fe/(001)Cr Magnetic Superlattices*“, Phys. Rev. Lett. **61**, 2472 (1988).
- [7] G. Binasch, P. Grünberg, F. Saurenbach and W. Zinn, „*Enhanced magnetoresistance in layered magnetic structures with antiferromagnetic interlayer exchange*“, Phys. Rev. B **39**, 4828 (1989).
- [8] M. Julliere, „*Tunneling between ferromagnetic films*“, Phys. Lett. A **54**, 225 (1975).
- [9] J. Slonczewski, „*Current-driven excitation of magnetic multilayers*“, J. Magn. Magn. Mater. **159**, L1 (1996).
- [10] J. J. Nowak, R. P. Robertazzi, J. Z. Sun, G. Hu, J.-H. Park, J. Lee, A. J. Annunziata, G. P. Lauer, R. Kothandaraman, E. J. O'Sullivan, P. L. Trouilloud, Y. Kim and D. C. Worledge, „*Dependence of Voltage and Size on Write Error Rates in Spin-Transfer Torque Magnetic Random-Access Memory*“, IEEE Magnetics Letters **7**, 1 (2016).
- [11] S. Bhatti, R. Sbiaa, A. Hirohata, H. Ohno, S. Fukami and S. Piramanayagam, „*Spintronics based random access memory: a review*“, Mater. Today **20**, 530 (2017).
- [12] A. A. Serga, A. V. Chumak and B. Hillebrands, „*YIG magnonics*“, J. Phys. D: Appl. Phys. **43**, 264002 (2010).
- [13] A. V. Chumak, V. I. Vasyuchka, A. A. Serga and B. Hillebrands, „*Magnon spintronics*“, Nat. Phys. **11**, 453 (2015).
- [14] D. Sander, S. O. Valenzuela, D. Makarov, C. H. Marrows, E. E. Fullerton, P. Fischer, J. McCord, P. Vavassori, S. Mangin, P. Pirro, B. Hillebrands, A. D. Kent, T. Jung-

- wirth, O. Gutfleisch, C. G. Kim and A. Berger, „*The 2017 Magnetism Roadmap*“, J. Phys. D: Appl. Phys. **50**, 363001 (2017).
- [15] M. Jamali, J. H. Kwon, S.-M. Seo, K.-J. Lee and H. Yang, „*Spin wave nonreciprocity for logic device applications*“, Sci. Rep. **3**, 3160 (2013).
- [16] S. Wintz, V. Tiberkevich, M. Weigand, J. Raabe, J. Lindner, A. Erbe, A. Slavin and J. Fassbender, „*Magnetic vortex cores as tunable spin-wave emitters*“, Nat. Nanotechnol. **11**, 948 (2016).
- [17] K.-S. Lee, S. Choi and S.-K. Kim, „*Radiation of spin waves from magnetic vortex cores by their dynamic motion and annihilation processes*“, Appl. Phys. Lett. **87**, 192502 (2005).
- [18] R. B. Holländer, C. Müller, J. Schmalz, M. Gerken and J. McCord, „*Magnetic domain walls as broadband spin wave and elastic magnetisation wave emitters*“, Sci. Rep. **8**, 13871 (2018).
- [19] K. Vogt, H. Schultheiss, S. Jain, J. E. Pearson, A. Hoffmann, S. D. Bader and B. Hillebrands, „*Spin waves turning a corner*“, Appl. Phys. Lett. **101**, 042410 (2012).
- [20] Q. Wang, Z. Zhong, L. Jin, X. Tang, F. Bai, H. Zhang and G. S. Beach, „*Design of nanostrip magnonic crystal waveguides with a single magnonic band gap*“, J. Magn. Mater. **340**, 23 (2013).
- [21] K. Vogt, F. Fradin, J. Pearson, T. Sebastian, S. Bader, B. Hillebrands, A. Hoffmann and H. Schultheiss, „*Realization of a spin-wave multiplexer*“, Nat. Commun. **5**, 3727 (2014).
- [22] A. V. Sadovnikov, C. S. Davies, V. V. Kruglyak, D. V. Romanenko, S. V. Grishin, E. N. Beginin, Y. P. Sharaevskii and S. A. Nikitov, „*Spin wave propagation in a uniformly biased curved magnonic waveguide*“, Phys. Rev. B **96**, 060401 (2017).
- [23] F. Garcia-Sanchez, P. Borys, R. Soucaille, J.-P. Adam, R. L. Stamps and J.-V. Kim, „*Narrow Magnonic Waveguides Based on Domain Walls*“, Phys. Rev. Lett. **114**, 247206 (2015).
- [24] K. Wagner, A. Kákay, K. Schultheiss, A. Henschke, T. Sebastian and H. Schultheiss, „*Magnetic domain walls as reconfigurable spin-wave nanochannels*“, Nat. Nanotechnol. **11**, 432 (2016).
- [25] E. Albisetti, D. Petti, G. Sala, R. Silvani, S. Tacchi, S. Finizio, S. Wintz, A. Calò, X. Zheng, J. Raabe, E. Riedo and R. Bertacco, „*Nanoscale spin-wave circuits based on engineered reconfigurable spin-textures*“, Communications Physics **1**, 56 (2018).
- [26] Y. Tserkovnyak, A. Brataas and G. E. W. Bauer, „*Enhanced Gilbert Damping in Thin Ferromagnetic Films*“, Phys. Rev. Lett. **88**, 117601 (2002).

- [27] K. Ando, S. Takahashi, J. Ieda, Y. Kajiwara, H. Nakayama, T. Yoshino, K. Harii, Y. Fujikawa, M. Matsuo, S. Maekawa and E. Saitoh, „*Inverse spin-Hall effect induced by spin pumping in metallic system*“, J. Appl. Phys. **109**, 103913 (2011).
- [28] Y. Kajiwara, K. Harii, S. Takahashi, J. Ohe, K. Uchida, M. Mizuguchi, H. Umezawa, H. Kawai, K. Ando, K. Takanashi, S. Maekawa and E. Saitoh, „*Transmission of electrical signals by spin-wave interconversion in a magnetic insulator*“, Nature **464**, 262 (2010).
- [29] R. Damon and J. Eshbach, „*Magnetostatic modes of a ferromagnet slab*“, J. Phys. Chem. Solids **19**, 308 (1961).
- [30] J. R. Eshbach and R. W. Damon, „*Surface Magnetostatic Modes and Surface Spin Waves*“, Phys. Rev. **118**, 1208 (1960).
- [31] O. Gladii, M. Haidar, Y. Henry, M. Kostylev and M. Bailleul, „*Frequency nonreciprocity of surface spin wave in permalloy thin films*“, Phys. Rev. B **93**, 054430 (2016).
- [32] K. Di, V. L. Zhang, H. S. Lim, S. C. Ng, M. H. Kuok, X. Qiu and H. Yang, „*Asymmetric spin-wave dispersion due to Dzyaloshinskii-Moriya interaction in an ultrathin Pt/CoFeB film*“, Appl. Phys. Lett. **106**, 052403 (2015).
- [33] K. Di, V. L. Zhang, H. S. Lim, S. C. Ng, M. H. Kuok, J. Yu, J. Yoon, X. Qiu and H. Yang, „*Direct Observation of the Dzyaloshinskii-Moriya Interaction in a Pt/Co/Ni Film*“, Phys. Rev. Lett. **114**, 047201 (2015).
- [34] K. Mika and P. Grünberg, „*Dipolar spin-wave modes of a ferromagnetic multilayer with alternating directions of magnetization*“, Phys. Rev. B **31**, 4465 (1985).
- [35] P. Grünberg, R. Schreiber, Y. Pang, M. B. Brodsky and H. Sowers, „*Layered Magnetic Structures: Evidence for Antiferromagnetic Coupling of Fe Layers across Cr Interlayers*“, Phys. Rev. Lett. **57**, 2442 (1986).
- [36] B. I. Halperin and P. C. Hohenberg, „*Hydrodynamic Theory of Spin Waves*“, Phys. Rev. **188**, 898 (1969).
- [37] E. Sonin, „*Spin currents and spin superfluidity*“, Adv. Phys. **59**, 181 (2010).
- [38] J. König, M. C. Bønsager and A. H. MacDonald, „*Dissipationless Spin Transport in Thin Film Ferromagnets*“, Phys. Rev. Lett. **87**, 187202 (2001).
- [39] J. Heurich, J. König and A. H. MacDonald, „*Persistent spin currents in helimagnets*“, Phys. Rev. B **68** (2003).
- [40] S. Takei and Y. Tserkovnyak, „*Superfluid Spin Transport Through Easy-Plane Ferromagnetic Insulators*“, Phys. Rev. Lett. **112**, 227201 (2014).
- [41] B. Flebus, S. Bender, Y. Tserkovnyak and R. Duine, „*Two-Fluid Theory for Spin Superfluidity in Magnetic Insulators*“, Phys. Rev. Lett. **116** (2016).

- [42] Y. Tserkovnyak and M. Kläui, „*Exploiting Coherence in Nonlinear Spin-Superfluid Transport*“, Phys. Rev. Lett. **119**, 187705 (2017).
- [43] H. Skarsvåg, C. Holmqvist and A. Brataas, „*Spin Superfluidity and Long-Range Transport in Thin-Film Ferromagnets*“, Phys. Rev. Lett. **115**, 237201 (2015).
- [44] E. Iacocca, T. J. Silva and M. A. Hofer, „*Symmetry-broken dissipative exchange flows in thin-film ferromagnets with in-plane anisotropy*“, Phys. Rev. B. **96**, 134434 (2017).
- [45] W. F. Brown, „*Micromagnetics, Domains, and Resonance*“, J. Appl. Phys. **30**, S62 (1959).
- [46] D. Griffiths, „*Introduction to Quantum Mechanics*“, Pearson international edition, Pearson Prentice Hall (2005).
- [47] D. Cortés-Ortuño and P. Landeros, „*Influence of the Dzyaloshinskii–Moriya interaction on the spin-wave spectra of thin films*“, J. Phys.: Condens. Matter **25**, 156001 (2013).
- [48] A. Fert, N. Reyren and V. Cros, „*Magnetic skyrmions: advances in physics and potential applications*“, Nature Reviews Materials **2**, 17031 (2017).
- [49] J. C. Maxwell, „*A Dynamical Theory of the Electromagnetic Field*“, Philos. Trans. R. Soc. London **155**, 459 (1865).
- [50] G. Green, „*An Essay on the Application of mathematical Analysis to the theories of Electricity and Magnetism*“, Nottingham (1828).
- [51] A. Aharoni, „*Magnetostatic energy calculations*“, IEEE Trans. Magn. **27**, 3539 (1991).
- [52] J. D. Jackson, „*Classical electrodynamics*“, Wiley, New York, NY, 3. Ed. (1999).
- [53] A. Aharoni, „*“Local” Demagnetization in a Rectangular Ferromagnetic Prism*“, Phys. Stat. Sol. (b) **229**, 1413 (2002).
- [54] J. H. van Vleck, „*On the Anisotropy of Cubic Ferromagnetic Crystals*“, Phys. Rev. **52**, 1178 (1937).
- [55] H. Brooks, „*Ferromagnetic Anisotropy and the Itinerant Electron Model*“, Phys. Rev. **58**, 909 (1940).
- [56] G. C. Fletcher, „*Calculations of the First Ferromagnetic Anisotropy Coefficient, Gyromagnetic Ratio and Spectroscopic Splitting Factor for Nickel*“, Proc. Phys. Soc. London, Sect. A **67**, 505 (1954).
- [57] M. A. Ruderman and C. Kittel, „*Indirect Exchange Coupling of Nuclear Magnetic Moments by Conduction Electrons*“, Phys. Rev. **96**, 99 (1954).
- [58] M. D. Stiles, „*Exchange coupling in magnetic heterostructures*“, Phys. Rev. B **48**, 7238 (1993).

- [59] P. Bruno, „*Interlayer exchange coupling: a unified physical picture*“, J. Magn. Mater. **121**, 248 (1993).
- [60] P. Bruno, „*Theory of interlayer magnetic coupling*“, Phys. Rev. B **52**, 411 (1995).
- [61] L. Landau and E. Lifshitz, „*On the theory of the dispersion of magnetic permeability in ferromagnetic bodies.*“, Phys. Zeits. Sowj. **8**, 153 (1935).
- [62] J. M. Luttinger and C. Kittel, „*Eine Bemerkung zur Quantentheorie der ferromagnetischen Resonanz*“, Helv. Phys. Acta **21**, 480 (1948).
- [63] J. H. Van Vleck, „*Concerning the Theory of Ferromagnetic Resonance Absorption*“, Phys. Rev. **78**, 266 (1950).
- [64] I. Newton, A. Motte and J. Machin, „*The Mathematical Principles of Natural Philosophy*“, No. Bd. 1 in The Mathematical Principles of Natural Philosophy, B. Motte (1729).
- [65] T. Gilbert, „*A phenomenological theory of damping in ferromagnetic materials*“, IEEE Trans. Magn. **40**, 3443 (2004).
- [66] S. V. Vonsovskii, „*Ferromagnetic resonance; the phenomenon of resonant absorption of a high-frequency magnetic field in ferromagnetic substances, edited by S.V. Vonsovski. Translated by H.S.H. Massey. Translation edited by D. ter Haar*“, Pergamon Press Oxford, New York, [1st english ed.]. Ed. (1966).
- [67] J. Smit and H. G. Beljers, „*Ferromagnetic Resonance Absorption in BaFe₁₂O₁₉ a highly anisotropic crystal.*“, Philips Res. Rep. **10**, 113 (1955).
- [68] H. Suhl, „*Ferromagnetic Resonance in Nickel Ferrite Between One and Two Kilocycles*“, Phys. Rev. **97**, 555 (1955).
- [69] L. Baselgia, M. Warden, F. Waldner, S. L. Hutton, J. E. Drumheller, Y. Q. He, P. E. Wigen and M. Maryško, „*Derivation of the resonance frequency from the free energy of ferromagnets*“, Phys. Rev. B **38**, 2237 (1988).
- [70] Z. Zhang, L. Zhou, P. E. Wigen and K. Ounadjela, „*Angular dependence of ferromagnetic resonance in exchange-coupled Co/Ru/Co trilayer structures*“, Phys. Rev. B **50**, 6094 (1994).
- [71] D. D. Stancil and A. Prabhakar, „*Spin waves: Theory and Applications*“, Springer (2010).
- [72] B. A. Kalinikos and A. N. Slavin, „*Theory of dipole-exchange spin wave spectrum for ferromagnetic films with mixed exchange boundary conditions*“, J. Phys. C: Solid State Phys. **19**, 7013 (1986).
- [73] S. Demokritov and A. Slavin, „*Magnonics: From Fundamentals to Applications*“, Topics in Applied Physics, Springer Berlin Heidelberg (2012).
- [74] A. Oosawa, M. Ishii and H. Tanaka, „*Field-induced three-dimensional magnetic ordering in the spin-gap system*“, J. Phys. Condens. Matter **11**, 265 (1999).

- [75] T. Nikuni, M. Oshikawa, A. Oosawa and H. Tanaka, „*Bose-Einstein Condensation of Dilute Magnons in $TlCuCl_3$* “, Phys. Rev. Lett. **84**, 5868 (2000).
- [76] T. Radu, H. Wilhelm, V. Yushankhai, D. Kovrizhin, R. Coldea, Z. Tylczynski, T. Lühmann and F. Steglich, „*Bose-Einstein Condensation of Magnons in Cs_2CuCl_4* “, Phys. Rev. Lett. **95**, 127202 (2005).
- [77] S. O. Demokritov, V. E. Demidov, O. Dzyapko, G. A. Melkov, A. A. Serga, B. Hillebrands and A. N. Slavin, „*Bose-Einstein condensation of quasi-equilibrium magnons at room temperature under pumping*“, Nature **443**, 430 (2006).
- [78] D. A. Bozhko, A. A. Serga, P. Clausen, V. I. Vasyuchka, F. Heussner, G. A. Melkov, A. Pomyalov, V. S. L'vov and B. Hillebrands, „*Supercurrent in a room-temperature Bose-Einstein magnon condensate*“, Nat. Phys. **12**, 1057 (2016).
- [79] P. Kapitza, „*Viscosity of Liquid Helium below the λ -Point*“, Nature **141**, 74 (1938).
- [80] E. Noether, „*Invariante Variationsprobleme*“, Nachrichten von der Gesellschaft der Wissenschaften zu Göttingen, Mathematisch-Physikalische Klasse **1918**, 235 (1918).
- [81] E. Iacocca, T. Silva and M. A. Hofer, „*Breaking of Galilean Invariance in the Hydrodynamic Formulation of Ferromagnetic Thin Films*“, Phys. Rev. Lett. **118**, 017203 (2017).
- [82] D. Hill, S. K. Kim and Y. Tserkovnyak, „*Spin-Torque-Biased Magnetic Strip: Nonequilibrium Phase Diagram and Relation to Long Josephson Junctions*“, Phys. Rev. Lett. **121**, 037202 (2018).
- [83] H. Chen and A. H. MacDonald, „*Spin-Superfluidity and Spin-Current Mediated Non-Local Transport*“, arXiv:, 1604.02429v1 (2016).
- [84] T. W. O'Keeffe and R. W. Patterson, „*Magnetostatic surface-wave propagation in finite samples*“, J. Appl. Phys. **49**, 4886 (1978).
- [85] W. Arkadiew, „*Über die Absorption elektromagnetischer Wellen an zwei parallelen Drähten*“, Ann. Phys. **363**, 105 (1919).
- [86] E. Zavoisky, „*Spin magnetic resonance in the decimetre-wave region*“, J. Phys. USSR **10**, 197 (1946).
- [87] J. H. E. Griffiths, „*Anomalous High-frequency Resistance of Ferromagnetic Metals*“, Nature **158**, 670 (1946).
- [88] H. T. Nembach, T. J. Silva, J. M. Shaw, M. L. Schneider, M. J. Carey, S. Maat and J. R. Childress, „*Perpendicular ferromagnetic resonance measurements of damping and Landé g-factor in sputtered $(Co_2Mn)_{1-x}Gex$ thin films*“, Phys. Rev. B **84**, 054424 (2011).
- [89] Y. S. Gui, S. Holland, N. Mecking and C. M. Hu, „*Resonances in Ferromagnetic Gratings Detected by Microwave Photoconductivity*“, Phys. Rev. Lett. **95**, 056807 (2005).

- [90] Y. S. Gui, N. Mecking and C. M. Hu, „*Quantized Spin Excitations in a Ferromagnetic Microstrip from Microwave Photovoltage Measurements*“, Phys. Rev. Lett. **98**, 217603 (2007).
- [91] Y. S. Gui, N. Mecking, A. Wirthmann, L. H. Bai and C.-M. Hu, „*Electrical detection of the ferromagnetic resonance: Spin-rectification versus bolometric effect*“, Appl. Phys. Lett. **91**, 082503 (2007).
- [92] Z. Duan, C. T. Boone, X. Cheng, I. N. Krivorotov, N. Reckers, S. Stienen, M. Farle and J. Lindner, „*Spin-wave modes in permalloy/platinum wires and tuning of the mode damping by spin Hall current*“, Phys. Rev. B **90**, 024427 (2014).
- [93] D. Markó, „*Magnetostatics and Dynamics of Ion Irradiated NiFe/Ta Multilayer Films Studied by Vector Network Analyzer Ferromagnetic Resonance*“, PhD thesis, TU Dresden (2010).
- [94] M. Donahue and D. Porter, „*OOMMF User’s Guide, Version 1.0*“, Technical report, National Institute of Standards and Technology (1999).
- [95] W. Scholz, J. Fidler, T. Schrefl, D. Suess, R. Dittrich, H. Forster and V. Tsiantos, „*Scalable parallel micromagnetic solvers for magnetic nanostructures*“, Comput. Mater. Sci. **28**, 366 (2003), Proceedings of the Symposium on Software Development for Process and Materials Design.
- [96] A. Kakay, E. Westphal and R. Hertel, „*Speedup of FEM Micromagnetic Simulations With Graphical Processing Units*“, IEEE Trans. Magn. **46**, 2303 (2010).
- [97] R. F. L. Evans, W. J. Fan, P. Chureemart, T. A. Ostler, M. O. A. Ellis and R. W. Chantrell, „*Atomistic spin model simulations of magnetic nanomaterials*“, J. Phys.: Condens. Matter **26**, 103202 (2014).
- [98] M. Lakshmanan, „*The fascinating world of the Landau-Lifshitz-Gilbert equation: an overview*“, Philosophical Transactions of the Royal Society A: Mathematical, Physical and Engineering Sciences **369**, 1280 (2011).
- [99] Y. Katznelson, „*An Introduction to Harmonic Analysis*“ (1976).
- [100] J. Leliaert, M. Dvornik, J. Mulkers, J. D. Clercq, M. V. Milošević and B. V. Waeyenberge, „*Fast micromagnetic simulations on GPU—recent advances made with mumax³*“, J. Phys. D: Appl. Phys. **51**, 123002 (2018).
- [101] N. Agrawal, V. Prabhakaran, T. Wobber, J. D. Davis, M. Manasse and R. Panigrahy, in *USENIX 2008 Annual Technical Conference, ATC’08*, P. 57–70, „*Design Trade-offs for SSD Performance*“, Berkeley, CA, USA (2008), USENIX Association.
- [102] T. Jones, A. Koniges and R. Yates, in *Proceedings 14th International Parallel and Distributed Processing Symposium. IPDPS 2000*, P. 673, „*Performance of the IBM general parallel file system*“. IEEE Comput. Soc (2000).

- [103] M. Frigo and S. G. Johnson, „*The Design and Implementation of FFTW3*“, Proc. IEEE **93**, 216 (2005), Special issue on “Program Generation, Optimization, and Platform Adaptation”.
- [104] T. Shanley, „*Infiniband*“, Addison-Wesley Longman Publishing Co., Inc., Boston, MA, USA (2002).
- [105] D. Kumar, O. Dmytriiev, S. Ponraj and A. Barman, „*Numerical calculation of spin wave dispersions in magnetic nanostructures*“, J. Phys. D: Appl. Phys. **45**, 015001 (2011).
- [106] F. Ruesink, M.-A. Miri, A. Alù and E. Verhagen, „*Nonreciprocity and magnetic-free isolation based on optomechanical interactions*“, Nat. Commun. **7**, 13662 (2016).
- [107] E. Verhagen and A. Alù, „*Optomechanical nonreciprocity*“, Nat. Phys. **13**, 922 (2017).
- [108] K. J. Moore, J. Bunyan, S. Tawfick, O. V. Gendelman, S. Li, M. Leamy and A. F. Vakakis, „*Nonreciprocity in the dynamics of coupled oscillators with nonlinearity, asymmetry, and scale hierarchy*“, Phy. Rev. E **97**, 012219 (2018).
- [109] N. Reiskarimian and H. Krishnaswamy, „*Magnetic-free non-reciprocity based on staggered commutation*“, Nat. Commun. **7**, 11217 (2016).
- [110] N. R. Bernier, L. D. Tóth, A. Koottandavida, M. A. Ioannou, D. Malz, A. Nunnenkamp, A. K. Feofanov and T. J. Kippenberg, „*Nonreciprocal reconfigurable microwave optomechanical circuit*“, Nat. Commun. **8**, 604 (2017).
- [111] D. L. Sounas and A. Alù, „*Non-reciprocal photonics based on time modulation*“, Nat. Photonics **11**, 774 (2017).
- [112] B. Hillebrands, „*Spin-wave calculations for multilayered structures*“, Phys. Rev. B **41**, 530 (1990).
- [113] B. Hillebrands, „*Brillouin light scattering from layered magnetic structures*“, P. 174–289, Springer, Berlin, Heidelberg (2000).
- [114] P. K. Amiri, B. Rejaei, M. Vroubel and Y. Zhuang, „*Nonreciprocal spin wave spectroscopy of thin Ni–Fe stripes*“, Appl. Phys. Lett. **91**, 062502 (2007).
- [115] M. Mruczkiewicz, M. Krawczyk, G. Gubbiotti, S. Tacchi, Y. A. Filimonov, D. V. Kalyabin, I. V. Lisenkov and S. A. Nikitov, „*Nonreciprocity of spin waves in metalized magnonic crystal*“, New J. Phys. **15**, 113023 (2013).
- [116] M. Mruczkiewicz, E. S. Pavlov, S. L. Vysotsky, M. Krawczyk, Y. A. Filimonov and S. A. Nikitov, „*Observation of magnonic band gaps in magnonic crystals with non-reciprocal dispersion relation*“, Phys. Rev. B **90**, 174416 (2014).
- [117] R. Verba, V. Tiberkevich, E. Bankowski, T. Meitzler, G. Melkov and A. Slavin, „*Conditions for the spin wave nonreciprocity in an array of dipolarly coupled magnetic nanopillars*“, Appl. Phys. Lett. **103**, 082407 (2013).

- [118] J. A. Otálora, M. Yan, H. Schultheiss, R. Hertel and A. Kákay, „*Curvature-Induced Asymmetric Spin-Wave Dispersion*“, Phys. Rev. Lett. **117**, 227203 (2016).
- [119] T. Moriya, „*New Mechanism of Anisotropic Superexchange Interaction*“, Phys. Rev. Lett. **4**, 228 (1960).
- [120] I. Dzyaloshinsky, „*A thermodynamic theory of “weak” ferromagnetism of antiferromagnetics*“, J. Phys. Chem. Solids **4**, 241 (1958).
- [121] H. T. Nembach, J. M. Shaw, M. Weiler, E. Jué and T. J. Silva, „*Linear relation between Heisenberg exchange and interfacial Dzyaloshinskii–Moriya interaction in metal films*“, Nat. Phys. **11**, 825 (2015).
- [122] S. Tacchi, R. Troncoso, M. Ahlberg, G. Gubbiotti, M. Madami, J. Åkerman and P. Landeros, „*Interfacial Dzyaloshinskii–Moriya Interaction in Pt/CoFeB Films: Effect of the Heavy-Metal Thickness*“, Phys. Rev. Lett. **118**, 147201 (2017).
- [123] L. Yang, P. Durrenfeld, X. Ruan, W. Liu, L. He, Y. Xu and Y. Zhou, „*Interfacial DMI Induced Directional Spin Wave in Spin-torque Oscillators*“, IEEE Magnetics Letters **8**, 1 (2017).
- [124] S.-J. Lee, J.-H. Moon, H.-W. Lee and K.-J. Lee, „*Spin-wave propagation in the presence of inhomogeneous Dzyaloshinskii–Moriya interactions*“, Phys. Rev. B **96**, 184433 (2017).
- [125] Z. Wang, B. Zhang, Y. Cao and P. Yan, „*Proposal to probe the Dzyaloshinskii–Moriya interaction by the propagation characteristics of spin waves in ferromagnetic thin films*“, arXiv:, <http://arxiv.org/abs/1807.04025v1> (2018).
- [126] J. Mulkers, B. V. Waeyenberge and M. V. Milošević, „*Tunable Snell's law for spin waves in heterochiral magnetic films*“, Phys. Rev. B **97**, 104422 (2018).
- [127] A. Vansteenkiste, J. Leliaert, M. Dvornik, M. Helsen, F. Garcia-Sanchez and B. V. Waeyenberge, „*The design and verification of MuMax3*“, AIP Advances **4**, 107133 (2014).
- [128] J.-H. Moon, S.-M. Seo, K.-J. Lee, K.-W. Kim, J. Ryu, H.-W. Lee, R. D. McMichael and M. D. Stiles, „*Spin-wave propagation in the presence of interfacial Dzyaloshinskii–Moriya interaction*“, Phys. Rev. B **88**, 184404 (2013).
- [129] J. Cho, N.-H. Kim, S. Lee, J.-S. Kim, R. Lavrijsen, A. Solignac, Y. Yin, D.-S. Han, N. J. J. van Hoof, H. J. M. Swagten, B. Koopmans and C.-Y. You, „*Thickness dependence of the interfacial Dzyaloshinskii–Moriya interaction in inversion symmetry broken systems*“, Nat. Commun. **6**, 7635 (2015).
- [130] A. Layadi, „*Resonance modes of cubic single crystal thin film with exchange anisotropy: A theoretical study*“, J. Appl. Phys. **87**, 1429 (2000).
- [131] A. Layadi, „*Effect of biquadratic coupling and in-plane anisotropy on the resonance modes of a trilayer system*“, Phys. Rev. B **65**, 104422 (2002).

- [132] M. Belmeguenai, T. Martin, G. Woltersdorf, M. Maier and G. Bayreuther, „*Frequency- and time-domain investigation of the dynamic properties of interlayer-exchange-coupled $Ni_{81}Fe_{19}/Ru/Ni_{81}Fe_{19}$ thin films*“, Phys. Rev. B **76**, 104414 (2007).
- [133] C. C. Kuo, M.-T. Lin and H. L. Huang, „*Effect of biquadratic exchange coupling on magnetoresistance and magnetization process in magnetic bilayer systems*“, J. Appl. Phys. **85**, 4430 (1999).
- [134] S. J. Yun, S. H. Lim and S.-R. Lee, „*Strong interlayer exchange coupling and high post-annealing stability in perpendicularly magnetized $[Pt/Co]/Ru/[Co/Pt]$ structures*“, AIP Advances **6**, 025112 (2016).
- [135] S. O. Demokritov, „*Biquadratic interlayer coupling in layered magnetic systems*“, J. Phys. D: Appl. Phys. **31**, 925 (1998).
- [136] J. Lindner, „*Ferromagnetische Resonanz an ultradiinnen magnetischen Einfach- und Mehrfachlagen der 3d-Übergangsmetalle – Statik und Dynamik*“, PhD thesis, Freie Universität Berlin (2002).
- [137] K. Lenz, „*Magnetische Anisotropie und Dämpfungsmechanismen in ultradiinnen 3d-Ferromagneten. Eine FMR-Studie.*“, PhD thesis, Freie Universität Berlin (2005).
- [138] A. K. Chaurasiya, C. Banerjee, S. Pan, S. Sahoo, S. Choudhury, J. Sinha and A. Barman, „*Direct Observation of Interfacial Dzyaloshinskii-Moriya Interaction from Asymmetric Spin-wave Propagation in $W/CoFeB/SiO_2$ Heterostructures Down to Sub-nanometer $CoFeB$ Thickness*“, Sci. Rep. **6**, 32592 (2016).
- [139] A. K. Chaurasiya, S. Choudhury, J. Sinha and A. Barman, „*Dependence of Interfacial Dzyaloshinskii-Moriya Interaction on Layer Thicknesses in $Ta/Co-Fe-B/TaO_x$ Heterostructures from Brillouin Light Scattering*“, Phys. Rev. Appl. **9**, 014008 (2018).
- [140] R. Mock, B. Hillebrands and R. Sandercock, „*Construction and performance of a Brillouin scattering set-up using a triple-pass tandem Fabry-Perot interferometer*“, J. Phys. E: Sci. Instrum. **20**, 656 (1987).
- [141] B. Heinrich and J. Bland, „*Ultrathin Magnetic Structures II: Measurement Techniques and Novel Magnetic Properties*“, Ultrathin Magnetic Structures, Springer Berlin Heidelberg (2006).
- [142] V. Sluka, T. Schneider, R. Gallardo, A. Kakay, M. Weigand, T. Warnatz, R. Mattheis, A. Roldan-Molina, P. Landeros, V. Tiberkevich et al., „*Emission and Propagation of Multi-Dimensional Spin Waves in Anisotropic Spin Textures*“, arXiv preprint arXiv:1807.00897 (2018).
- [143] J. Raabe, G. Tzvetkov, U. Flechsig, M. Böge, A. Jaggi, B. Sarafimov, M. G. C. Ver-nooij, T. Huthwelker, H. Ade, D. Kilcoyne, T. Tyliczszak, R. H. Fink and C. Quitmann, „*PoLLux: A new facility for soft x-ray spectromicroscopy at the Swiss Light Source*“, Rev. Sci. Instrum. **79**, 113704 (2008).

- [144] M. Labruno and J. Miltat, „*Wall structures in ferro/antiferromagnetic exchange-coupled bilayers: A numerical micromagnetic approach*“, J. Magn. Magn. Mater. **151**, 231 (1995).
- [145] G. Dieterle, J. Förster, H. Stoll, A. S. Semisalova, S. Finizio, A. Gangwar, M. Weigand, M. Noske, M. Fähnle, I. Bykova, D. A. Bozhko, H. Y. Musienko-Shmarova, V. Tiberkevich, A. N. Slavin, C. H. Back, J. Raabe, G. Schütz and S. Wintz, „*Coherent excitation of heterosymmetric spin waves with ultrashort wavelengths*“, arXiv: <http://arxiv.org/abs/1712.00681v1> (2017).
- [146] N. J. Whitehead, S. A. R. Horsley, T. G. Philbin, A. N. Kuchko and V. V. Kruglyak, „*Theory of linear spin wave emission from a Bloch domain wall*“, Phys. Rev. B **96**, 064415 (2017).
- [147] V. P. Kravchuk, Y. Gaididei and D. D. Sheka, „*Nucleation of a vortex-antivortex pair in the presence of an immobile magnetic vortex*“, Phys. Rev. B **80**, 100405 (2009).
- [148] A. Conca, E. T. Papaioannou, S. Klingler, J. Greser, T. Sebastian, B. Leven, J. Lösch and B. Hillebrands, „*Annealing influence on the Gilbert damping parameter and the exchange constant of CoFeB thin films*“, Appl. Phys. Lett. **104**, 182407 (2014).
- [149] S. Wintz, T. Strache, M. Körner, C. Bunce, A. Banholzer, I. Mönch, R. Mattheis, J. Raabe, C. Quitmann, J. McCord, A. Erbe, K. Lenz and J. Fassbender, „*Control of vortex pair states by post-deposition interlayer exchange coupling modification*“, Phys. Rev. B **85**, 134417 (2012).
- [150] D. Wang, C. Nordman, Z. Qian, J. M. Daughton and J. Myers, „*Magnetostriction effect of amorphous CoFeB thin films and application in spin-dependent tunnel junctions*“, J. Appl. Phys. **97**, 10C906 (2005).
- [151] B. V. de Wiele, S. J. Hämäläinen, P. Baláž, F. Montoncello and S. van Dijken, „*Tunable short-wavelength spin wave excitation from pinned magnetic domain walls*“, Sci. Rep. **6**, 21330 (2016).
- [152] P. E. Roy, T. Trypiniotis and C. H. W. Barnes, „*Micromagnetic simulations of spin-wave normal modes and the resonant field-driven magnetization dynamics of a 360° domain wall in a soft magnetic stripe*“, Phys. Rev. B **82**, 134411 (2010).
- [153] J. Wei, Z. Zhu, C. Song, H. Feng, P. Jing, X. Wang, Q. Liu and J. Wang, „*Annealing influence on the exchange stiffness constant of Permalloy films with stripe domains*“, J. Phys. D: Appl. Phys. **49**, 265002 (2016).
- [154] J. Goldstone, A. Salam and S. Weinberg, „*Broken Symmetries*“, Phys. Rev. **127**, 965 (1962).
- [155] S. K. Kim and Y. Tserkovnyak, „*Magnetic Domain Walls as Hosts of Spin Superfluids and Generators of Skyrmions*“, Phys. Rev. Lett. **119**, 047202 (2017).
- [156] P. Upadhyaya, S. K. Kim and Y. Tserkovnyak, „*Magnetic Domain Wall Floating on a Spin Superfluid*“, Phys. Rev. Lett. **118**, 097201 (2017).

- [157] W. Yuan, Q. Zhu, T. Su, Y. Yao, W. Xing, Y. Chen, Y. Ma, X. Lin, J. Shi, R. Shindou, X. C. Xie and W. Han, „*Experimental signatures of spin superfluid ground state in canted antiferromagnet Cr₂O₃ via nonlocal spin transport*“, *Sci. Adv.* **4**, eaat1098 (2018).
- [158] P. Stepanov, S. Che, D. Shcherbakov, J. Yang, R. Chen, K. Thilagar, G. Voigt, M. W. Bockrath, D. Smirnov, K. Watanabe, T. Taniguchi, R. K. Lake, Y. Barlas, A. H. MacDonald and C. N. Lau, „*Long-distance spin transport through a graphene quantum Hall antiferromagnet*“, *Nat. Phys.* **14**, 907 (2018).
- [159] I. H. Solt, „*Temperature Dependence of YIG Magnetization*“, *J. Appl. Phys.* **33**, 1189 (1962).
- [160] S. Klingler, A. V. Chumak, T. Mewes, B. Khodadadi, C. Mewes, C. Dubs, O. Surzhenko, B. Hillebrands and A. Conca, „*Measurements of the exchange stiffness of YIG films using broadband ferromagnetic resonance techniques*“, *J. Phys. D: Appl. Phys.* **48**, 015001 (2014).
- [161] C. Dubs, O. Surzhenko, R. Linke, A. Danilewsky, U. Brückner and J. Dellith, „*Sub-micrometer yttrium iron garnet LPE films with low ferromagnetic resonance losses*“, *J. Phys. D: Appl. Phys.* **50**, 204005 (2017).
- [162] T. Schneider, D. Hill, A. Kakay, K. Lenz, J. Lindner, J. Fassbender, P. Upadhyaya, Y. Liu, K. Wang, Y. Tserkovnyak, I. N. Krivorotov and I. Barsukov, „*Self-stabilizing spin superfluid*“, arXiv: <http://arxiv.org/abs/1811.09369v1> (2018).
- [163] V. P. Kravchuk, D. D. Sheka, A. Kákay, O. M. Volkov, U. K. Röbber, J. van den Brink, D. Makarov and Y. Gaididei, „*Multiplet of Skyrmion States on a Curvilinear Defect: Reconfigurable Skyrmion Lattices*“, *Phys. Rev. Lett.* **120**, 067201 (2018).
- [164] V. E. Zakharov, V. S. L'vov and S. S. Starobinets, „*Spin-wave turbulence beyond the parametric excitation threshold*“, *Sov. Phys. Usp.* **17**, 896 (1975).
- [165] J. Cuevas-Maraver, P. Kevrekidis and F. Williams, „*The sine-Gordon Model and its Applications: From Pendula and Josephson Junctions to Gravity and High-Energy Physics*“, *Nonlinear Systems and Complexity*, Springer International Publishing (2014).
- [166] P. J. Caudrey, J. C. Eilbeck and J. D. Gibbon, „*The sine-Gordon equation as a model classical field theory*“, *Il Nuovo Cimento B Series 11* **25**, 497 (1975).
- [167] J. Rubinstein, „*Sine-Gordon Equation*“, *J. Math. Phys.* **11**, 258 (1970).
- [168] T. H. R. Skyrme, „*A Non-Linear Theory of Strong Interactions*“, *Proceedings of the Royal Society A: Mathematical, Physical and Engineering Sciences* **247**, 260 (1958).
- [169] A. J. Newell, W. Williams and D. J. Dunlop, „*A generalization of the demagnetizing tensor for nonuniform magnetization*“, *J. Geophys. Res.* **98**, 9551 (1993).

- [170] W. Wang, C. Mu, B. Zhang, Q. Liu, J. Wang and D. Xue, „*Two-dimensional periodic boundary conditions for demagnetization interactions in micromagnetics*“, *Comput. Mater. Sci.* **49**, 84 (2010).
- [171] E. Sonin, in *APS March Meeting*, „*Spin superfluidity: superfluid ^3He , solids, spinor BEC*“ (2018).
- [172] G. H. O. Daalderop, P. J. Kelly and F. J. A. den Broeder, „*Prediction and confirmation of perpendicular magnetic anisotropy in Co/Ni multilayers*“, *Phys. Rev. Lett.* **68**, 682 (1992).
- [173] J.-M. Beaujour, D. Ravelosona, I. Tudosa, E. E. Fullerton and A. D. Kent, „*Ferromagnetic resonance linewidth in ultrathin films with perpendicular magnetic anisotropy*“, *Phys. Rev. B* **80**, 180415 (2009).
- [174] M. Haertinger, C. H. Back, S.-H. Yang, S. S. P. Parkin and G. Woltersdorf, „*Properties of Ni/Co multilayers as a function of the number of multilayer repetitions*“, *J. Phys. D: Appl. Phys.* **46**, 175001 (2013).
- [175] C. Coutts, M. Arora, R. Hübner, B. Heinrich and E. Girt, „*Magnetic properties of Co/Ni grain boundaries after annealing*“, *AIP Advances* **8**, 056318 (2018).
- [176] S. Andrieu, T. Hauet, M. Gottwald, A. Rajanikanth, L. Calmels, A. M. Bataille, F. Montaigne, S. Mangin, E. Otero, P. Ohresser, P. L. Fèvre, F. Bertran, A. Resta, A. Vlad, A. Coati and Y. Garreau, „*Co/Ni multilayers for spintronics: High spin polarization and tunable magnetic anisotropy*“, *Phys. Rev. Mater.* **2**, 064410 (2018).
- [177] L. Qassym, C. Carretero, E. Jacquet, J. Ben-Youssef, R. Lebourgeois, V. Cros, P. Bortolotti, A. Anane, L. Soumah and N. Beaulieu, in *Spintronics X*, Ed. H. Jaffrès, H.-J. Drouhin, J.-E. Wegrowe and M. Razeghi, „*Perpendicular magnetic anisotropy in Bismuth substituted nanometers thick YIG films (Conference Presentation)*“. SPIE (2017).
- [178] L. Soumah, N. Beaulieu, L. Qassym, C. Carrétéro, E. Jacquet, R. Lebourgeois, J. B. Youssef, P. Bortolotti, V. Cros and A. Anane, „*Ultra-low damping insulating magnetic thin films get perpendicular*“, arXiv:, <http://arxiv.org/abs/1806.00658v1> (2018).
- [179] C. Tang, P. Sellappan, Y. Liu, Y. Xu, J. E. Garay and J. Shi, „*Anomalous Hall hysteresis in $\text{Tm}_3\text{Fe}_5\text{O}_{12}/\text{Pt}$ with strain-induced perpendicular magnetic anisotropy*“, arXiv:, <http://arxiv.org/abs/1609.06367v1> (2016).
- [180] M. Arora, R. Hübner, D. Suess, B. Heinrich and E. Girt, „*Origin of perpendicular magnetic anisotropy in Co/Ni multilayers*“, *Phys. Rev. B* **96**, 024401 (2017).
- [181] H. Callen and E. Callen, „*The present status of the temperature dependence of magnetocrystalline anisotropy, and the power law*“, *J. Phys. Chem. Solids* **27**, 1271 (1966).
- [182] K. Zakeri, T. Kebe, J. Lindner and M. Farle, „*Power-law behavior of the temperature dependence of magnetic anisotropy of uncapped ultrathin Fe Films on GaAs(001)*“, *Phys. Rev. B* **73**, 052405 (2006).

List of Figures

2.1. Spherical coordinate system for the magnetization M and the external field $\mu_0 H$	5
2.2. Trajectory of the magnetization around the effective field direction.	14
2.3. Renormalized energy contribution for spin waves as a function of wave length.	19
2.4. Sketch of (a) Damon-Eshbach, (b) backward-volume and (c) forward-volume spin waves.	20
2.5. Schematic representation of the transported spin current in non-superfluidic and superfluidic media.	23
3.1. Maximum throughput in millions of cells as a function of the total cell number in MuMax ³	29
3.2. Flow chart of MuMax ³ -pwsp	31
3.3. Runtime of MuMax ³ -pwsp in the HPC release as a function of cells.	32
3.4. Power spectrum of the magnetic vortex.	34
3.5. Example of two simulated dispersion relations for a thin magnetic film.	35
3.6. Runtime of MuMax ³ -dispersion for both releases as a function of cells.	36
4.1. Sketch of the bilayer system in the antiparallel state.	41
4.2. Nonreciprocal spin wave dispersion relation in magnetic bilayers.	43
4.3. Schematic representation of the magnetic volume and surface charges produced by the dynamic magnetization in a magnetic bilayer.	45
4.4. Magnetometry measurements for the sample Ch2724 for (a) in-plane orientation and (b) out-of-plane orientation of the magnetic field.	47
4.5. In-plane angular dependence of the sample Ch2754.	49
4.6. Polar angular dependence of sample Ch2724.	50
4.7. Frequency-field dependence $f(H)$ of sample Ch2724.	51
4.8. BLS spectra for selected wave numbers for (a) the antiparallel and (b) the parallel state of sample Ch2724.	53
4.9. Spin-wave dispersion and frequency shift for Stokes and Antistokes for the antiparallel (left panel) and the parallel state (right) panel.	54

4.10. Sketch of the dynamic magnetization profile along the thickness of a thick magnetic bilayer.	55
4.11. STXM images of the magnetic configuration of the coupled bilayer.	56
4.12. TR-STXM image of the magnetic configuration of the coupled bilayer.	57
4.13. Micromagnetic simulations of the excitation mode in coupled domain walls.	58
4.14. Dispersion relation for the coupled Vortex pair.	60
4.15. Calculated dispersion relation of the coupled vortex pair.	61
5.1. Sketch of the theoretically investigated system.	64
5.2. Gradient of the in-plane angle φ as a function of the distance from the injector.	65
5.3. Initial fluid velocity u_0 and frequency Ω of the superfluid state as a function of the injector current density omitting dipole-dipole interactions.	66
5.4. Dependence of the spin superfluid on the injector width.	68
5.5. Gradient of the in-plane angle φ as a function of the channel length with cubic in-plane anisotropy.	73
5.6. Gradient of the in-plane angle φ as a function of channel length with enabled presence of non-local dipole interactions.	74
5.7. Perturbed magnetization configuration of the superfluid state in the presence of dipole-dipole interaction.	75
5.8. Initial fluid velocity u_0 and frequency of the spin superfluid as a function of the injector current density in the presence of dipole-dipole interactions.	76
5.9. Normalized threshold current j_0/d as a function of the film thickness d	77
5.10. Sketch of the NiCo nanowire with the superfluidic state excited.	79
5.11. Comparison of the shape anisotropy and the PMA for different wire widths.	80
5.12. Gradient of the easy-plane angle φ for different nanowires with PMA.	82
5.13. Color-coded dynamic response of the magnetization as a function of frequency Ω and injector current density j for the compensated 40 nm wide NiCo wire.	83
5.14. Color-coded dynamic response of the magnetization as a function of frequency Ω and injector current density j for the 40 nm wide NiCo wire with different strengths of the uniaxial anisotropy.	84
5.15. Color-coded dynamic response of the magnetization as a function of frequency Ω and injector current density j for the 20 nm wide NiCo wire with different strengths of the uniaxial anisotropy.	85
5.16. Anisotropy energy (a) and anisotropy field including the second-order anisotropy in a 20 nm NiCo wire.	86

A.1. Effect of a window function on the result of a FFT. 95

List of Tables

4.1. Overview of the thickness of the individual layers of all samples.	46
4.2. Overview of magnetic parameters for selected samples.	49
4.3. Experimentally determined material parameters for sample Ch2724. The magnetic properties were determined by FMR, SQUID and VSM. The layer thicknesses and the spacer thickness were determined by cross-section TEM.	52
5.1. Extracted parameters for the first critical current $j_{\text{crit}}^{(1)}$ as a function of the injector width w	69

Acknowledgment

An dieser Stelle möchte ich allen Personen herzlich danken, welche an dieser Promotion beteiligt waren:

Prof. S. Gemming für die Übernahme des Erstgutachtens.

Prof. J. Fassbender als Zweitgutachter dieser Arbeit.

Ein Dank gilt auch Dr. J. Lindner und Dr. K. Lenz für die Betreuung der Arbeit und die zahlreichen Diskussionen.

Außerdem möchte ich mich bei dem gesamten hier nicht erwähnten FWIN-Team für das angenehme Arbeitsklima, die zahlreichen Diskussionen und die Hilfsbereitschaft bedanken.

Auch allen Personen, welche diese Arbeit Korrektur gelesen haben, gilt ein Dank.

Im Einzelnen danken ich Dr. R. Gallardo und Prof. P. Landeros für die Möglichkeit drei Monate in ihrer Arbeitsgruppe in Valparaíso verbringen zu können und für ihre tatkräftige Unterstützung in theoretischen Fragen. Des Weiteren möchte ich mich bei Prof. O. Hellwig und seinem Team für die Herstellung der Proben bedanken. Einen großen Dank gebührt außerdem Prof. K. Barman und A. K. Chaurasiya für die BLS Messungen. Auch Dr. R. Hübner möchte ich für die TEM Messungen danken.

Einen besonderen Dank gilt Prof. I. Barsukov für die sehr hilfreiche Kritik des Superfluid-Manuskripts und die Möglichkeit der Mitarbeit in seiner Arbeitsgruppe. Auch bei Prof. Y. Tserkovnyak und D. Hill für die sehr schnelle Ausarbeitung der Theorie für das Manuskript möchte ich danken.

Ein ganz besonderer Dank gilt meinen Eltern für die finanzielle und moralische Unterstützung während, aber auch schon vor meinem Studium.

Letztlich gilt auch meiner Freundin Ulrike ein besonderer Dank für die moralische Unterstützung in der Endphase meiner Promotion.

Declaration of Authorship

I, Tobias Schneider, declare that this thesis titled, 'Spin dynamics and transport in magnetic heterostructures' and the work presented in it are my own. I confirm that:

- This work was done wholly while in candidature for a doctoral degree at the Technische Universität Chemnitz.
- Where any part of this thesis has previously been submitted for a degree or any other qualification at this University or any other institution, this has been clearly stated.
- Where I have consulted the published work of others, this is always clearly attributed.
- Where I have quoted from the work of others, the source is always given. With the exception of such quotations, this thesis is entirely my own work.
- I have acknowledged all main sources of help.
- In the acknowledgements, I have made clear which of the results presented in this thesis are based on work done in cooperation with others. I have made clear exactly what was done by others.

Tobias Schneider

Dresden, November 2018